Computational aspects of generalized continua based on moving least square approximations

Sebastian Skatulla

Thesis submitted to the University of Adelaide
for the degree of Doctor of Philosophy

September, 2006

School of Mechanical Engineering
The University of Adelaide

Chapter 4

Classical Green strain tensor-based formulation

A classical *Green strain tensor*-based model is taken to be the reference model for the formulations developed in the latter. In order to improve the performance of this formulation with respect to the essential boundary condition enforcement of an elliptic PDE within MLS-based meshfree methods, a modified variational principle is proposed in the following.

4.1 A modified variational principle

Let us consider a non-linear boundary value problem on domain $\mathcal{B}$ with boundary $\partial\mathcal{B}$. Dirichlet boundary conditions are prescribed on $\partial\mathcal{B}_D \subset \partial\mathcal{B}$ and Neumann boundary conditions are prescribed on $\partial\mathcal{B}_N = \partial\mathcal{B} \setminus \partial\mathcal{B}_D$.

We assume a hyperelastic material behaviour and let $\rho_0\psi(\mathbf{E})$ define the stored energy function per unit volume, where $\mathbf{E}$ the *Green strain tensor* (Eq. 2.23). Further, let $\mathcal{W}_{ext}$ define the external potential as follows

$$\mathcal{W}_{ext}(\mathbf{u}) = -\int_{\mathcal{B}} \rho_0 \mathbf{b} \cdot \mathbf{u}\, dV - \int_{\partial\mathcal{B}_N} \hat{\mathbf{t}}^{(\mathbf{n})} \cdot \mathbf{u}\, dA\,, \tag{4.1}$$

where $\mathbf{b}$ is the body force, $\hat{\mathbf{t}}^{(\mathbf{n})}$ is the external traction vector prescribed on $\mathcal{B}_N$ and $\mathbf{n}$ defines the normal vector at the boundary $\partial\mathcal{B}$. We start from the following variational statement

$$\delta\Psi(\mathbf{u}) = \int_{\mathcal{B}} \mathbf{S} : \delta\mathbf{E}\, dV - \int_{\mathcal{B}} \mathbf{b} \cdot \delta\mathbf{u}\, dV - \int_{\partial\mathcal{B}_N} \hat{\mathbf{t}}^{(\mathbf{n})} \cdot \delta\mathbf{u}\, dA = 0\,, \tag{4.2}$$

where $\mathbf{S}$ is the second Piola-Kirchhoff stress tensor given by

$$\mathbf{S}(\mathbf{u}) = \rho_0 \frac{\partial\psi(\mathbf{E})}{\partial\mathbf{E}}\,. \tag{4.3}$$

The above functional corresponds to the following Euler-Lagrange field equations

$$\frac{1}{\sqrt{G}}\left(\sqrt{G}\,\mathbf{F}\mathbf{S}\mathbf{G}^i\right)_{,i}+\rho_0\,\mathbf{b}\;=\;\mathbf{0}\;,\quad\text{in }\mathcal{B}\;,\qquad\mathbf{F}\mathbf{S}\mathbf{n}-\hat{\mathbf{t}}^{(\mathbf{n})}=\mathbf{0}\quad\text{on }\partial\mathcal{B}_N\;, \tag{4.4}$$

where G is the determinate of the *Riemannian* metric coefficients (Eq. 2.13) and $\mathbf{F}$ is the deformation gradient tensor (Eq. 2.5). Note that here and throughout this section the basis vectors $\mathbf{G}_i$ are assumed to be independent of θ^k.

These field equations are supplemented by essential boundary conditions, the so-called Dirichlet boundary conditions

$$\mathbf{u}=\mathbf{h}\quad\text{on }\partial\mathcal{B}_D\;. \tag{4.5}$$

To incorporate the essential boundary conditions in the functional itself, that is to enforce these conditions as Euler-Lagrange equation, the functional (Eq. 4.2) is modified in the following way

$$\begin{aligned}\delta\Psi\left(\mathbf{u}\right)=&\int_{\mathcal{B}}\mathbf{S}:\delta\mathbf{E}\;dV+\int_{\partial\mathcal{B}_D}\delta\left(\boldsymbol{\lambda}\cdot\left(\mathbf{u}-\mathbf{h}\right)\right)\;dA-\int_{\mathcal{B}}\rho_0\,\mathbf{b}\cdot\delta\mathbf{u}\;dV-\\&-\int_{\partial\mathcal{B}_N}\hat{\mathbf{t}}^{(\mathbf{n})}\cdot\delta\mathbf{u}\;dA=0\;.\end{aligned} \tag{4.6}$$

Making use of *Gauss's divergence theorem* this formulation is transferred back to its strong form which is the integral form of the Euler-Lagrange equations

$$\begin{aligned}\delta\Psi\left(\mathbf{u}\right)=&-\int_{\mathcal{B}}\frac{1}{\sqrt{G}}\left(\sqrt{G}\,\mathbf{F}\mathbf{S}\mathbf{G}^i\right)_{,i}\cdot\delta\mathbf{u}\;dV+\int_{\partial\mathcal{B}}\mathbf{F}\mathbf{S}\mathbf{n}\cdot\delta\mathbf{u}\;dA+\int_{\partial\mathcal{B}_D}\boldsymbol{\lambda}\cdot\delta\mathbf{u}\;dA+\\&+\int_{\partial\mathcal{B}_D}\delta\boldsymbol{\lambda}\cdot\left(\mathbf{u}-\mathbf{h}\right)\;dA\;-\int_{\mathcal{B}}\rho_0\,\mathbf{b}\cdot\delta\mathbf{u}\;dV-\int_{\partial\mathcal{B}_N}\hat{\mathbf{t}}^{(\mathbf{n})}\cdot\delta\mathbf{u}\;dA=0\,.\end{aligned} \tag{4.7}$$

Since this integral equation must be valid for any arbitrary $\delta\mathbf{u}$, we can extract the Euler-Lagrange equations (Eq. 4.4) and identify the Lagrange multipliers as $\boldsymbol{\lambda}=-\mathbf{F}\mathbf{S}\mathbf{n}$ on $\partial\mathcal{B}_D$. Note that the second term in Eq. (4.7) is an integral expression over the entire boundary $\partial\mathcal{B}$. The final problem statement takes the following form

$$\begin{aligned}\delta\Psi\left(\mathbf{u}\right)=&\int_{\mathcal{B}}\mathbf{S}:\delta\mathbf{E}\;dV-\int_{\partial\mathcal{B}_D}\mathbf{F}\mathbf{S}\mathbf{n}\cdot\delta\mathbf{u}\;dA-\int_{\partial\mathcal{B}_D}\delta\left(\mathbf{F}\mathbf{S}\mathbf{n}\right)\cdot\left(\mathbf{u}-\mathbf{h}\right)\;dA-\\&-\int_{\mathcal{B}}\rho_0\,\mathbf{b}\cdot\delta\mathbf{u}\;dV-\int_{\partial\mathcal{B}_N}\hat{\mathbf{t}}^{(\mathbf{n})}\cdot\delta\mathbf{u}\;dA=0\;.\end{aligned} \tag{4.8}$$

4.2 A stabilized modified variational principle

The modified variational principle outlined in the previous section heavily relies on the accurate evaluation of the boundary integral expression. This is due to the fact that the definition of the Lagrange multipliers $\boldsymbol{\lambda} = -\mathbf{FSn}$ relates to *Gauss's divergence theorem* which states the equivalence of a volume and a surface integral expression. This equivalence however, is not given anymore, if the numerical accuracy is substantially lacking. Consequently, the essential boundary condition fulfillment can not be ensured anymore which also affects the solution for the entire problem domain. In this context we recall that Breitkopf *et al.* (2002) as well as De and Bathe (2000) noted that MLS-based formulations can not be as accurately integrated due to the non-polynomial character of the meshfree approximation function. Dolbow and Belytschko (1999) also made the misalignment between particle support zones and integration cells responsible for the reduced numerical integration accuracy. Especially the spherical particle influence zone was said to be disadvantageous. Therefore, they proposed a so-called bounding box technique to match particle support and background mesh and so to improve the performance of the integration. However, it can also be found that the meshfree approximation quality close to the boundary is significantly worse than within the domain. This is clear, as the particle support of the boundary area is less than that of the domain interior and consequently, the influence zones of those particles close the boundary must be chosen larger than within the domain in order to compensate this lack of support. Larger particle influence zone though, result in a solution approximation which is less local and therefore less accurate. For more details the reader is referred to Sec. 3.2. Consequently, the mathematical equivalence of volume and surface integral expressions is disturbed and so, the solution behaviour can become instable.

An approach to stabilize the modified variational principle introduced in Sec. 4.1, is to incorporate an additional stabilization or penalty term, the purpose of which is to balance out the lacking boundary approximation and boundary condition enforcement accuracy. The problem formulation introduced in the previous section is then extended as follows

$$\begin{aligned}\delta\Pi(\mathbf{u}) = &\int_{\mathcal{B}} \mathbf{S} : \delta\mathbf{E}\, dV - \int_{\partial\mathcal{B}_D} \mathbf{FSn}\cdot\delta\mathbf{u}\, dA - \int_{\partial\mathcal{B}_D} \delta(\mathbf{FSn})\cdot(\mathbf{u}-\mathbf{h})\; dA + \\ &+\beta\int_{\partial\mathcal{B}_D}(\mathbf{u}-\mathbf{h})\cdot\delta\mathbf{u}\, dA - \int_{\mathcal{B}}\mathbf{b}\cdot\delta\mathbf{u}\, dV - \int_{\partial\mathcal{B}_N}\hat{\mathbf{t}}^{(\mathbf{n})}\cdot\delta\mathbf{u}\, dA = 0\,, \end{aligned} \tag{4.9}$$

where the fourth term in Eq. (4.9) is a stabilization term together with the stabilization parameter β which is constant on $\partial\mathcal{B}_D$. The idea is, however, to keep the magnitude of the stabilization parameter β as low as possible to avoid an ill-conditioned discrete equation system.

For a similar but linear problem Nitsche showed the existence of a certain minimum positive constant which ensures that the coefficient matrix of the discrete equation system is positive definite and the solution is approximated within optimal error bounds (Nitsche 1970-1971). This constant could be related to β and was said to be dependent on the used basis polynomial and the chosen discretization of the solution space. The latter relates in

meshfree methods to the covering of the problem domain $\mathcal{B}$ by the particle support zones which basically puts on geometric constraints on their intersections (Griebel and Schweitzer 2002).

Applying this idea to solid mechanics we find, similar to the augmented Lagrangian method (Ventura 2002), that the material parameters strongly influence the determination of the stabilization parameter. Now, it is desirable if a suitable value for the stabilization parameter β is computed automatically. To achieve this, Griebel and Schweitzer (2002) proposed to solve a general eigenvalue problem of the following form

$$\mathbf{A}\mathbf{x} = \lambda \mathbf{B}\mathbf{x} \tag{4.10}$$

with the surface part of the stiffness matrix denoted by matrix $\mathbf{A}$ and the volume part by $\mathbf{B}$. The maximum eigenvalue was suggested to be taken as stabilization parameter β. Preliminary tests showed however, that this procedure leads to a magnitude of the stabilization parameter which is already at penalty levels. Thus, the stabilization term is dominating the problem formulation. Furthermore, in meshfree methods the boundary enforcement error is varying depending on the particle support. Therefore, it makes sense to consider the stabilization parameter as function of the coordinates charts ζ^1 and ζ^2 which describe the boundary $\partial\mathcal{B}_D$. We rewrite the modified variational principle Eq. (4.9) as follows

$$\begin{aligned}\delta\Pi(\mathbf{u}) = &\int_{\mathcal{B}} \mathbf{S} : \delta\mathbf{E}\, dV - \int_{\partial\mathcal{B}_D} \mathbf{FSn}\cdot\delta\mathbf{u}\, dA - \int_{\partial\mathcal{B}_D} \delta(\mathbf{FSn})\cdot(\mathbf{u}-\mathbf{h})\, dA + \\ &+ \int_{\partial\mathcal{B}_D} \beta\left(\zeta^1, \zeta^2, h_i\right)(\mathbf{u}-\mathbf{h})\cdot\delta\mathbf{u}\, dA - \int_{\mathcal{B}} \mathbf{b}\cdot\delta\mathbf{u}\, dV - \int_{\partial\mathcal{B}_N} \hat{\mathbf{t}}^{(\mathbf{n})}\cdot\delta\mathbf{u}\, dA = 0\,.\end{aligned} \tag{4.11}$$

In the discretized domain this means that the stabilization parameter is computed for each integration point individually and is not constant on $\partial\mathcal{B}$. Inspired by an iteration procedure applied to the augmented Lagrangian method (Ventura, 2002) we are utilizing an iteration procedure to determine the minimum necessary penalty value at each integration point in order to ensure solution stability and a high convergence rate. Hereby, the idea is to run the problem first as geometrically linear one and to compare at each integration point the error in the essential boundary condition enforcement ϵ with a given error tolerance δ

$$\epsilon\left(\zeta^1, \zeta^2, h_i\right) = \left| u_i\left(\zeta^1, \zeta^2\right) - h_i\left(\zeta^1, \zeta^2\right)\right| < \delta\,. \tag{4.12}$$

The value of this parameter δ is usually taken similarly to the limit of the convergence norm of the displacement field used for the Newton-Raphson method. The magnitude of the error in the boundary condition enforcement provides an indication of how much the constraint reaction resultant is too low. Depending on whether the error is higher or lower than the given error tolerance the stabilization parameter is increased or decreased correspondingly. Using these new adapted stabilization parameters and assigning to all particle parameter zero values, the problem is then solved again and the stabilization parameters are further modified if necessary. This process is repeated until the error tolerance is achieved at all

integration points. It usually takes about five to ten iteration steps to determine a suitable stabilization parameter distribution. At the start of this procedure $\beta(\zeta^1, \zeta^2, h_i)$ is estimated for all integration points individually by the following expression

$$\beta\left(\zeta^1, \zeta^2, h_i\right) = \frac{\epsilon\left(\zeta^1, \zeta^2, h_i\right)}{\delta}, \tag{4.13}$$

where $\epsilon(\zeta^1, \zeta^2, h_i)$ is the boundary condition enforcement error evaluated after the first iteration step. During the iteration procedure $\beta(\zeta^1, \zeta^2, h_i)$ is successively increased or decreased depending on the error of the boundary enforcement.

Note that in case of the augmented Lagrangian method the iteration procedure is undertaken with respect to the stabilization parameters as well as the Lagrange multipliers, but the modified variational principle Eq. (4.11) only requires the stabilization parameters to be obtained. That is the error in the essential boundary condition fulfillment is compensated by the stabilization term. For more details on the iteration algorithm the reader is referred to App. C.

4.3 Numerical examples

4.3.1 Study on essential boundary condition enforcement

In the following our aim is to study the applicability of the proposed stabilized modified variational principle on two different examples. Three different cases are distinguished: Firstly, using the modified variational principle together with the iterative stabilization parameter determination algorithm Eq. (4.11), secondly, using this modified variational principle with a constant and uniform stabilization parameter $\beta \in \partial\mathcal{B}_D$ which is Eq. (4.9), and finally, applying instead of the modified variational principle the conventional penalty method to enforce the essential boundary conditions. That is, only the penalty term with a constant penalty parameter β is incorporated in the original variational formulation Eq. (4.8), but not the other boundary terms which led to the modified variational principle Eq. (4.9).

Furthermore, two different material laws shall be utilized. These are the linear *Saint-Venant-Kirchhoff* model with the material parameters *Young's modulus* E and *Poisson's ratio* ν and a non-linear statistically based model of hyperelasticity (Arruda and Boyce 1993; Sansour *et al.* 2003a) which involves as constitutive parameters the shear modulus C_R, the bulk modulus κ and parameter N. The constant N addresses the limited extensibility of the macromolecular network structure of the rubber material.

Cantilever beam under pressure loading

The first study is a cantilever beam which is subjected to a constant pressure load on its top surface. It makes use of the *Saint-Venant-Kirchhoff* constitutive model and is illustrated in Fig. 4.1. The beam is modelled using 26 particles in longitudinal and only 2 in thickness

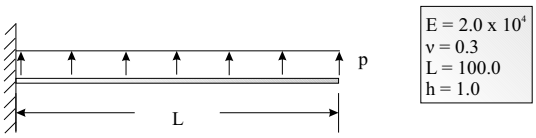

Figure 4.1: *problem definition*

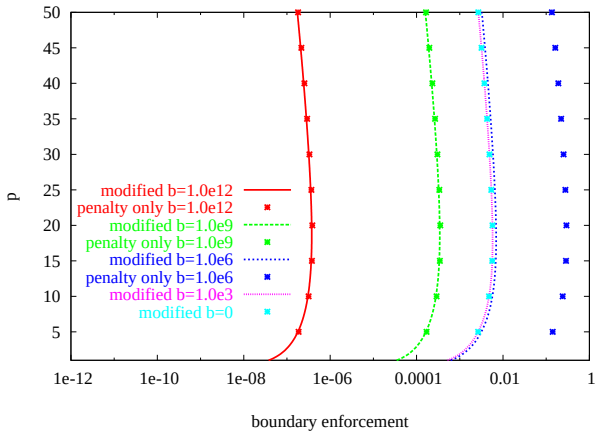

Figure 4.2: *boundary enforcement*

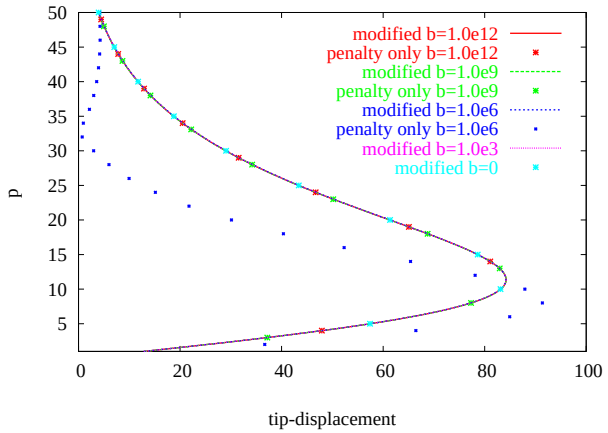

Figure 4.3: *displacement diagram*

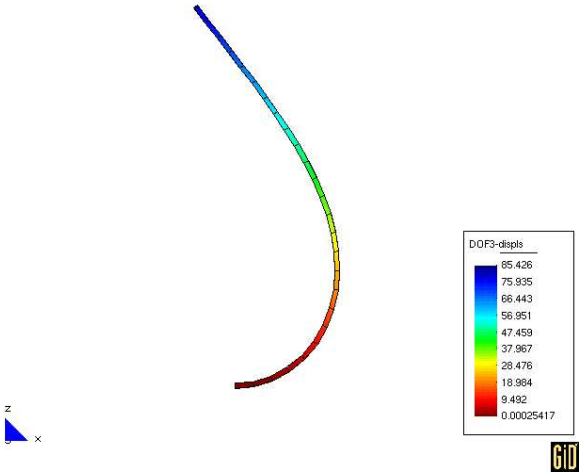

Figure 4.4: *deformed configuration at loading parameter* $p = 30$

direction. The stabilization parameters in the modified variational principle are kept uniform on $\partial\mathcal{B}_D$ and the results are compared with those achieved applying the penalty method instead. The boundary enforcement for different magnitudes of stabilization and penalizing is displayed in Fig. 4.2 and the corresponding tip deflection in Fig. 4.3. Note that the curves illustrating the tip deflection fall into one single line except for the one which represents the solution obtained using the penalty method with $\beta = 1.0 \times 10^6$ denoted by the dotted blue curve. We further find that the enforcement of the essential boundary conditions is best, if β is chosen to 1.0×10^{12}. The accuracy of our problem formulation is identical to the penalty method based formulation for parameters $\beta = 1.0 \times 10^{12}$ to $\beta = 1.0 \times 10^9$. The penalty method fails to provide meaningful results for penalty parameter values $\beta \leq 1.0 \times 10^6$. Using our proposed modified variational principle the stabilization parameter β can be chosen absolutely freely in order to achieve an accurate result for the tip deflection. Nevertheless, the accuracy of the boundary enforcement and the convergence rate become poorer for decreasing stabilization parameter values. In case of the modified variational formulation the lack

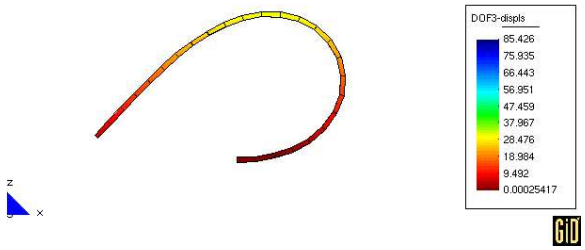

Figure 4.5: *deformed configuration at loading parameter* $p = 50$

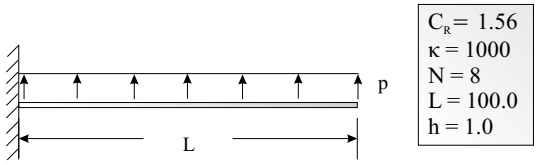

Figure 4.6: *problem definition*

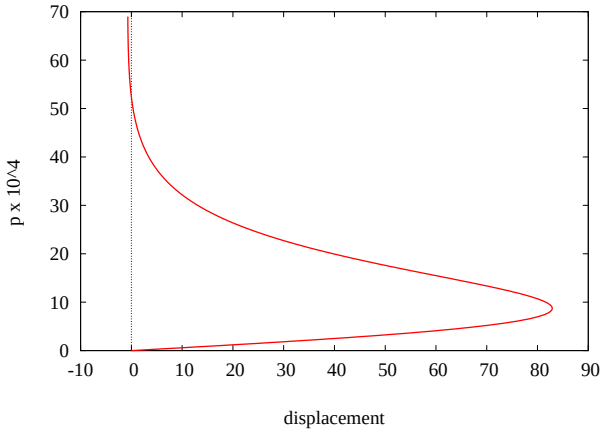

Figure 4.7: *displacement diagram*

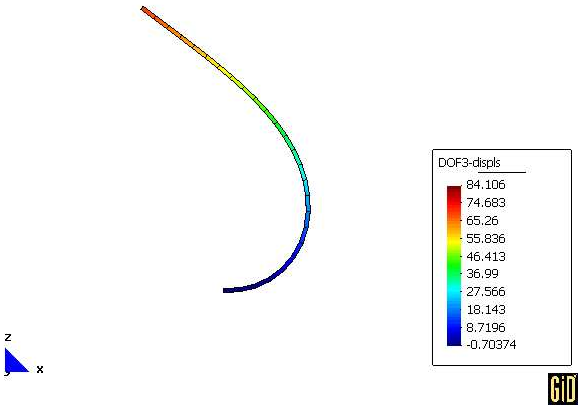

Figure 4.8: *deformed configuration at loading parameter* 13.5×10^4

of boundary approximation accuracy is for low values of the stabilization parameter quite significant, nonetheless we find good solutions for the tip deflection. The reason might be that the area having essential boundary conditions applied is minor compared to total surface of the problem domain. Moreover, there is no variation in the boundary approximation accuracy on all four affected particles and all integration points used for the surface integration of $\partial\mathcal{B}_D$. The deformed configuration depicted in Fig. 4.4 and Fig. 4.5 are modelled with the modified variational principle setting $\beta(\zeta^1, \zeta^2, h_i) = 0$ on $\partial\mathcal{B}_D$. Since the pressure acts during the entire simulation always perpendicular to the surface, the deformation process results in a kind of an ellipsoid.

Next, the above cantilever beam is again modelled with the same particle discretization, but using the non-linear hyperelastic material law instead of the linear Saint-Venant-Kirchhoff and is depicted in Fig. 4.6. Similar to the first study, the stabilization term in the modified variational principle is not needed. It is therefore simulated with $\beta(\zeta^1, \zeta^2, h_i) = 0$

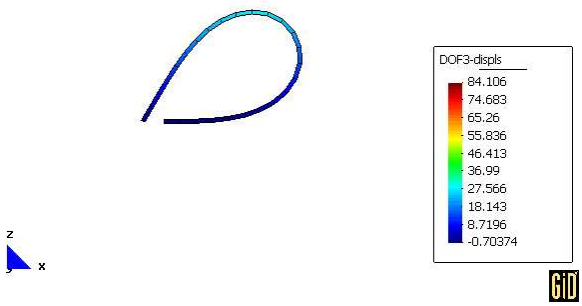

Figure 4.9: *deformed configuration at loading parameter* 69.0×10^4

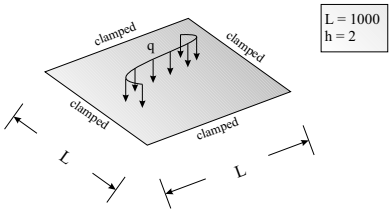

Figure 4.10: *problem definition*

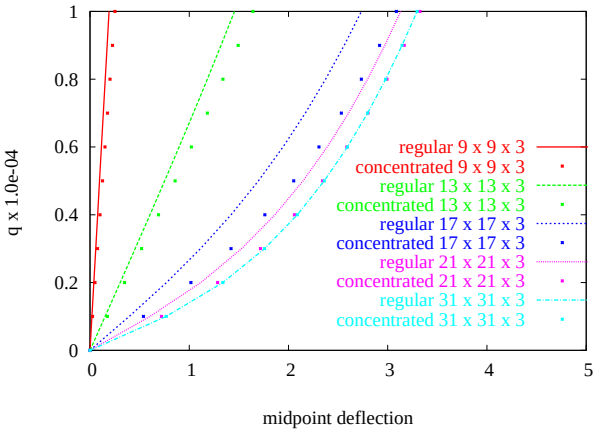

Figure 4.11: *displacement diagram of the midpoint deflection - linear material*

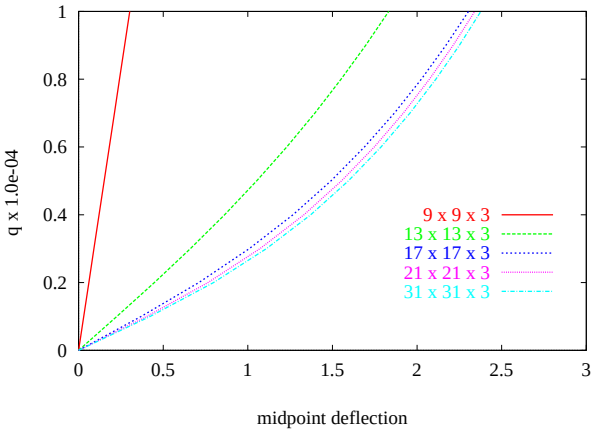

Figure 4.12: *displacement diagram of the midpoint deflection - non-linear material*

on $\partial\mathcal{B}_D$. The displacement diagram for the cantilever beam's tip is shown in Fig. 4.7 and the final deformed configuration in Fig. 4.9. The use of the penalty method is again critical, because only with the knowledge of the solution the correct penalty parameter can be determined.

Square sheet under dead loading

The next study's problem configuration is depicted in Fig. 4.10. It is a square sheet which is clamped at all four edges and subjected to a dead loading. It can be frequently found in literature. This problem is much more sensitive with respect to choice for the stabilization or penalty parameter than the cantilever beam presented in the previous paragraph. This is clear, as the analytical solution for cantilever beam's deflection only contains third order

exponents of the longitudinal coordinate, whereas for the clamped plate's deflection fourth order exponents of the in-plane coordinates. Considering that the approximation accuracy plays a crucial role especially on the boundary, different discretization levels are tested starting from the coarsest grid with 9×9, further 13×13, 17×17, 21×21 and the finest with 31×31 particles along the in-plane directions. Each configuration has three particle layers in thickness direction. A larger number of particles in thickness direction does not significantly improve the accuracy of the results. This fact is conceivable, as the solution of the displacement field primarily changes along the in-plane directions. As mentioned before, we find on the boundary a particle support deficit which must be compensated by enlarging the influence zones of particles located in the boundary area. An increased particle support however means a decrease of approximation locality and thus accuracy which is crucial for the modified variational principle. In order to circumvent this dilemma it is also meaningful not only to analyze equally spaced particle distributions, but additionally grids that are denser towards the boundary. This is achieved by shifting the particles from the center of the plate gradually to its edges. Therefore we distinguish for each discretization level another four different particle distribution densities ranging from equally spaced to strongly concentrated on the boundaries. By concentrating the particles towards the plate's edges the boundary and the inner domain approximation accuracy is expected to be more in balance, what should improve the overall applicability of the proposed modified variational principle. It is important to stress that the particle density is continuously increased towards the boundary. Otherwise, there would be jumps in the particle density and the particle distribution would be too irregular resulting in a negative effect on the approximation accuracy.

At first, the Saint-Venant-Kirchhoff constitutive law is applied with the material parameters *Young's modulus* $E = 2.0 \times 10^4$ and *Poisson's ratio* $\nu = 0.3$. The use of the penalty method exhibits the general difficulty that various solutions can be obtained for penalty parameters ranging from $\beta = 1.0$ - 1.0×10^{12}. This means, the problem behaves too soft or far too stiff. The correct result for the midpoint deflection however, can be found for $\beta \approx 1.0 \times 10^6$, whereas the boundary condition enforcement is always the best for $\beta = 1.0 \times 10^{12}$. It is therefore impossible to find out a suitable penalty parameter without the knowledge of the correct result. The modified variational principle provides with $\beta(\zeta^1, \zeta^2, h_i) = 0$ on $\partial\mathcal{B}_D$ for geometrically linear modelling a solution for the midpoint deflection which is the best achievable for each discretization level. The essential boundary condition enforcement however, is poor so that geometrically non-linear modelling fails for whatever particle distributions without utilizing the stabilization term. Therefore, the iteration procedure introduced in Sec. 4.2 is now used to determine a suitable stabilization parameter distribution $\beta(\zeta^1, \zeta^2, h_i)$. The load-deflection diagrams illustrated in Fig. 4.11 are modelled for different discretization levels. Each discretization level is simulated with a regularly spaced particle distribution denoted by the continuous line and an increased particle density on the boundary denoted by the dotted line. Note that the regular and the concentrated particle distribution have each the same total number of particles. The boundary enforcement error tolerance is set $\delta = 1.0 \times 10^{-8}$. We find for discretization levels $17 \times 17 \times 3$ and above that the minimum stabilization parameter is determined to $\beta_{min}(\zeta^1, \zeta^2) = 0$ and for the coarser grids it does not exceed $\beta(\zeta^1, \zeta^2, h_i)_{min} = 15$. The maximum value ranges from $\beta_{max}(\zeta^1, \zeta^2, h_i) = 5.0 \times 10^7 - 1.0 \times 10^{10}$ for different discretization levels and modes,

whereas lowest maximum stabilization parameter is achieved for $31 \times 31 \times 3$ particles regularly spaced. The particles distributions $9 \times 9 \times 3$ and $13 \times 13 \times 3$ fail to provide a good solution for the midpoint deflection. The discretization levels $17 \times 17 \times 3$ and $21 \times 21 \times 3$ however, show good solution accuracy, especially with the concentrated particle distribution near the boundary. The solution of the finest grid does not significantly change, if we apply higher particle density on the plate's edges. In all cases the highest values for $\beta(\zeta^1, \zeta^2, h_i)$ are always found at the clamped edges of the plate, whereas the lowest within the domain on the symmetry boundary. The minimum and maximum stabilization parameters can not be said to be significantly influenced by varying particle distribution. It seems that the constitutive law and the magnitude of its parameters have the main impact. This finding partly coincides with results of the next study, where the stiffness matrix norm is lower and correspondingly $\beta_{max}(\zeta^1, \zeta^2, h_i)$ has much lower values compared to this example.

In the next step the non-linear statistically based constitutive law is applied which involves as material parameters the shear modulus $C_R = 10 \times 10^3$, the bulk modulus $\kappa = 10.0 \times 10^7$ and parameter $N = 8$. These parameter are chosen in such way to provide a similar rigidity as we had for the Saint-Venant-Kirchhoff model. The boundary enforcement error tolerance is set $\delta = 1.0 \times 10^{-8}$. Compared to the previous study with the linear material law we find a substantially better boundary condition enforcement accuracy and consequently, much lower values for the stabilization parameters $\beta_{min}(\zeta^1, \zeta^2, h_i) = 0$ and $\beta_{max}(\zeta^1, \zeta^2, h_i) = 6.0 \times 10^4$ are computed in order to achieve a stable and fast converging non-linear simulation. Especially the two highest discretization levels do not need the stabilization term at all. For particle discretization levels $17 \times 17 \times 3$ and above a higher particle density on the plate's edges significantly improves the boundary enforcement accuracy, but not the midpoint deflection. Apparently, the boundary approximation accuracy provided by a regular particle distribution is in case of the non-linear constitutive model already sufficient enough to achieve the best possible solution for given number of particles. The convergence rate is almost as high as having the penalty method used with the optimal penalty parameter. Therefore, the load-deflection diagrams depicted in Fig. 4.12 are modelled for each discretization level with a regularly spaced particle distribution only.

4.3.2 Shell deformation examples

After demonstrating the excellent applicability of the modified variational formulation Eq. (4.11) in the previous sub-section, three further examples are presented that feature large deformations of shells. The problem configurations of all examples are discretized by regularly spaced particle grids and the modified variational principle is applied using the iterative stabilization parameter computation algorithm to determine the stabilization parameter distribution $\beta(\theta^1, \theta^2, \hat{u}_i)$ on $\mathcal{B}$. The boundary enforcement error tolerance is set $\delta = 1.0 \times 10^{-8}$.

Pinched cylinder with free edges

This example is a classical one, a cylindrical shell is subjected to two vertically opposite point loads at its central points (point A) as depicted in Fig. 4.13. Assuming appropriate symmetry boundary conditions, the cylinder is modelled using one octant with 6 particles in

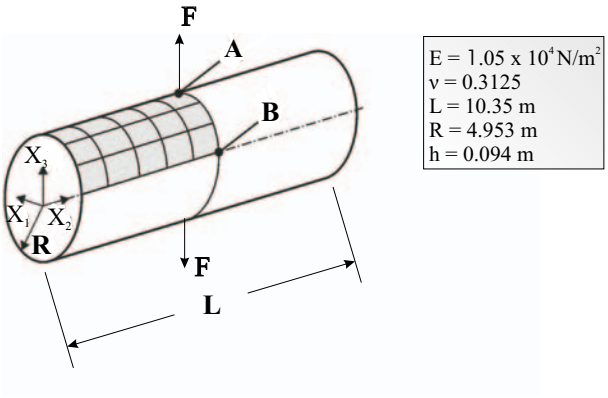

Figure 4.13: *problem definition*

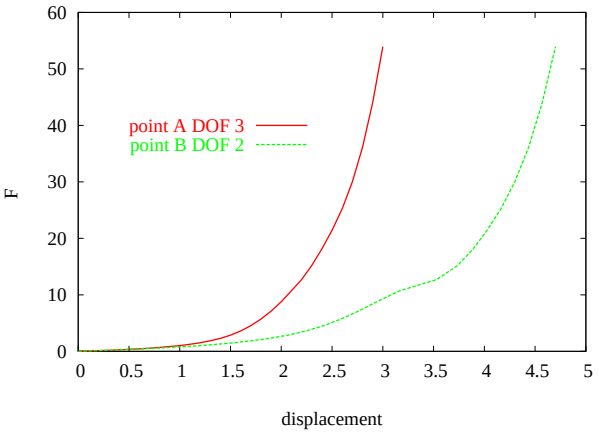

Figure 4.14: *displacement diagram*

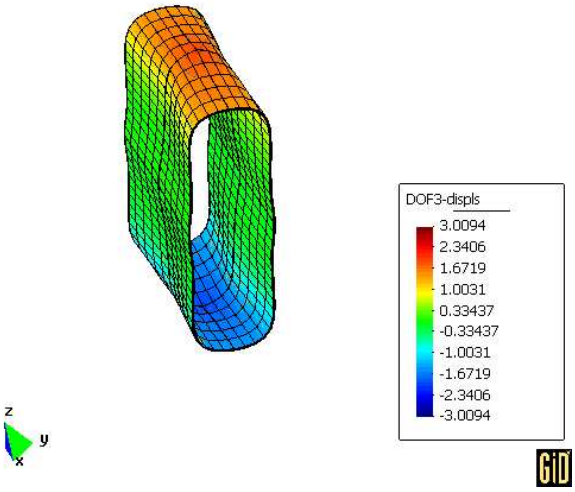

Figure 4.15: *deformed configuration at loading parameter* 8.78

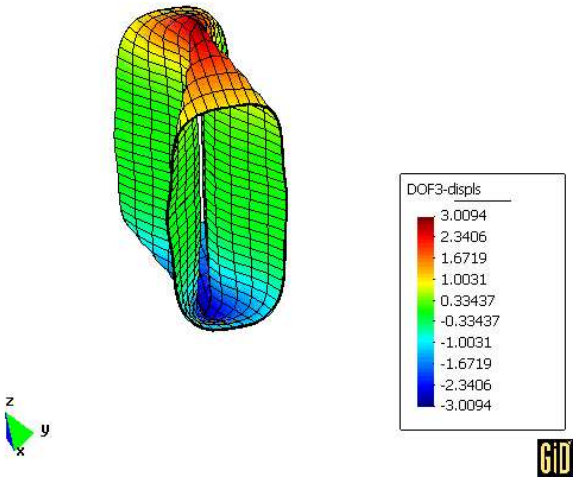

Figure 4.16: *deformed configuration at loading parameter* 53.95

longitudinal, 16 in radial, and 3 in thickness direction. The applied constitutive law is the Saint-Venant-Kirchhoff model.

The displacement diagram in Fig. 4.14 is illustrated for point A and point B. The diagram shows that the deformation process is split into two parts. The first part is bending dominated which results in large deformations for small loading parameters. The second part is characterized by a steep slope. In Fig. 4.16, the final deformed configuration is displayed. It should be mentioned that this example has been considered by many authors using different shell finite elements. In fact, our numerical results are in good agreement with those reported in the literature. The iterative stabilization parameter determination provides values

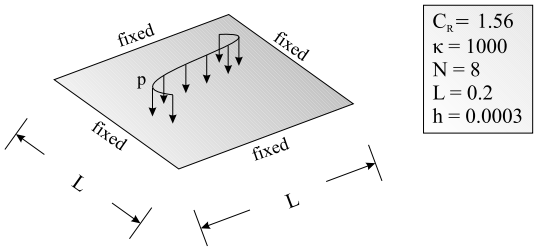

Figure 4.17: *problem definition*

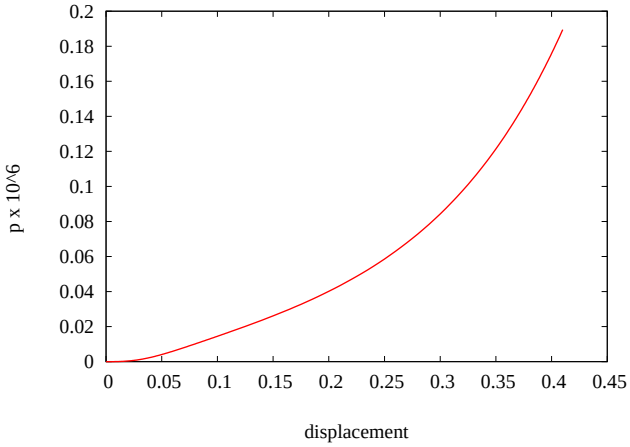

Figure 4.18: *displacement diagram*

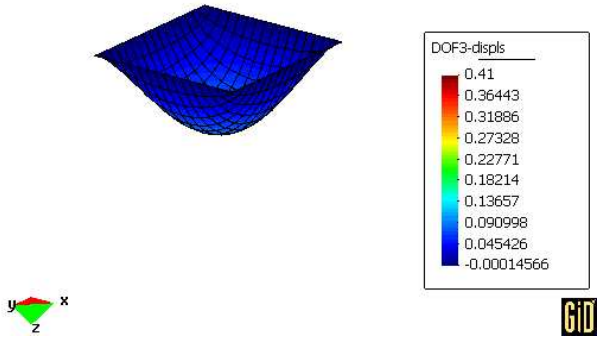

Figure 4.19: *deformed configuration at loading parameter* 0.015×10^6

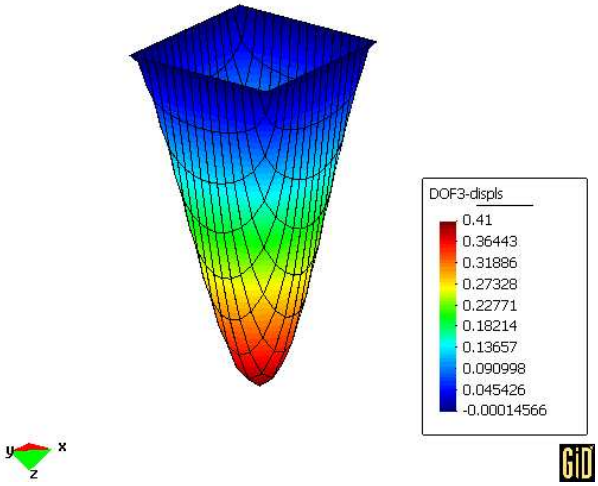

Figure 4.20: *deformed configuration at loading parameter* 0.189×10^6

$\beta_(\zeta^1, \zeta^2, h_i) = 118.8$ - 6.1×10^{10}. Even if the solution exhibits a final boundary enforcement error $\epsilon = 1.3 \times 10^{-4}$ the modelling is stable and converges at high rates.

The remaining two applications make use of the non-linear statistically based model involving as constitutive parameters the shear modulus C_R, the bulk modulus κ and the parameter N.

Square sheet under dead loading

The following example is a sheet which is fixed at all four edges and subjected to a dead loading on its top surface as illustrated in Fig. 4.17. Due to the symmetry conditions, only

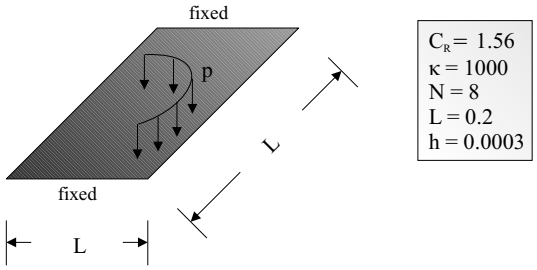

Figure 4.21: *problem definition*

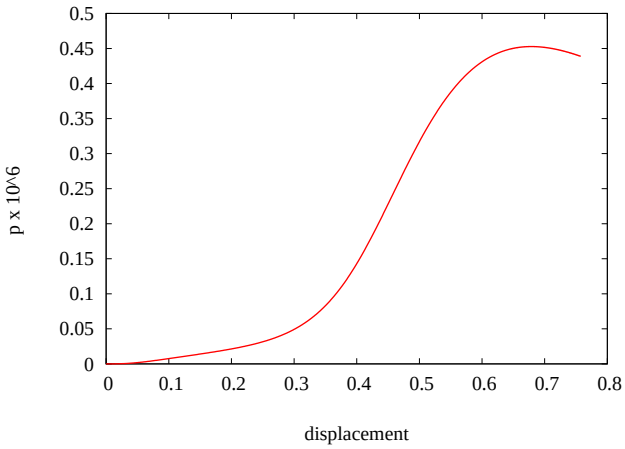

Figure 4.22: *displacement diagram*

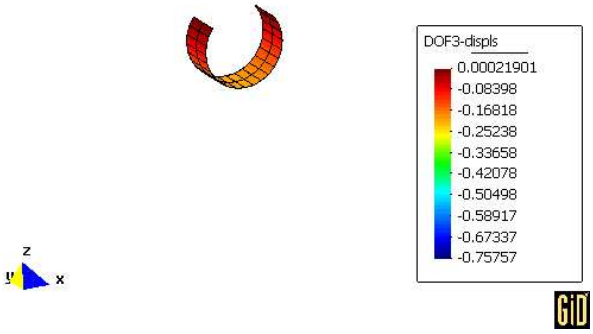

Figure 4.23: *deformed configuration at loading parameter* 0.008×10^6

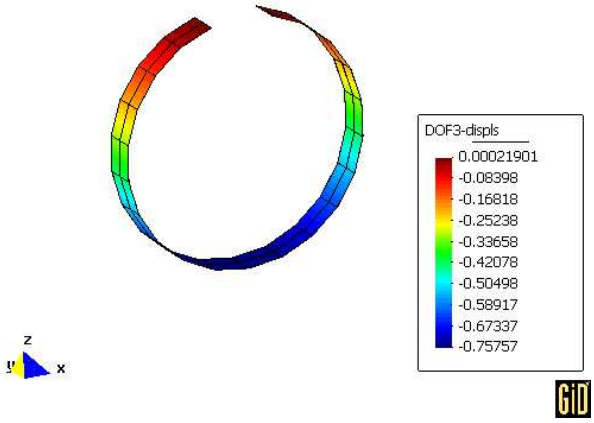

Figure 4.24: *deformed configuration at loading parameter* 0.439×10^6

one quarter of the sheet is modelled using 6 particles in length and 3 in thickness direction. The load-deflection diagram is presented in Fig. 4.18 for the vertical midpoint displacement and the deformed configurations are shown in Fig. 4.19 and Fig. 4.20 for different loading parameters. This problem is out of all our examples the most sensitive one with respect to the discretization. That is, the number of particle layers in length direction is limited to maximal 7, if 3 particles layers in thickness direction are chosen. The best results we can find however, if 5 particle layers are utilized in longitudinal direction. The stabilization parameters in this particular examples is determined to $\beta(\zeta^1, \zeta^2, h_i) = 1.4 \times 10^3$ - 3.5×10^7.

Square sheet under pressure loading

The last example is a square sheet which is simply supported at two opposite edges shown

in Fig. 4.21. On its top surface an uniform pressure load is applied. Due to symmetry conditions, only one half of the sheet is modelled using 11 particles in length, 3 in width and 3 in thickness direction. Despite a not very refined discretization this example performs a very large deformation which is depicted in Fig. 4.23 and Fig. 4.24. The entire deformation process is displayed in Fig. 4.22 for the vertical midpoint displacement. The examples is simulated with stabilization parameters $\beta(\zeta^1, \zeta^2, h_i) = 0.0$ - 7.0×10^{-5}.

Summarizing, the proposed augmented modified variational principle is demonstrated to be a real alternative to the penalty method. This is as the solution dependency on the stabilization parameter is minimized and so also the stabilization term's affect on the physical properties of the problem configuration. Furthermore, the magnitude of the stabilization parameters $\beta(\zeta^1, \zeta^2, h_i)$ are kept on relatively low levels, but sufficiently high to enforce the essential boundary at all integration points within a given error tolerance. This benefits a high adaptivity to various problems with different essential boundary conditions applied. The difficulty to find suitable values for $\beta(\zeta^1, \zeta^2, h_i)$ is solved by using an iterative algorithm which allows to determine them individually for each integration point.

Chapter 5

Cosserat continuum

5.1 Overview

The *Cosserat continuum* falls into the group of micropolar continua as defined by Eringen (1999) and those are a sub-group of the so-called generalized continua which will be addressed in more detail in Sec. 6. Micropolar continuum mechanical models originated in the so-called *Cosserat theory of elasticity* (Cosserat and Cosserat 1909) are characterized by the property that each material point inherits a rotation field which is independent of and additional to the conventional displacement field. This rotation field can be introduced by means of a rotation tensor which is element of the *Lie* group $SO(3)$ (Sansour and Bednarczyk 1995). The *Cosserat continuum* possesses two strain measures which are presented in Sec. 5.2. Since the rotation tensor exhibits a multiplicative and non-linear structure, it is natural to carry out its variation and updating multiplicatively. Sec. 5.3 addresses the variation of the rotation tensor and both strain measures. The weak problem statement based on the *Cosserat continuum* is outlined in Sec. 5.4 which also includes the corresponding equilibrium equations. Sec. 5.5 provides the details of a multiplicative rotation updating algorithm and investigates its applicability to the moving least square method. In Sec. 5.6 the enforcement of the displacement boundary conditions is proposed by modifying the original variational formulation. Finally, in Sec. 5.7 the presented modified variational statement is used to model size-scale effects of bone and polymeric specimens.

The elaborations in Sec. 5.2 - Sec. 5.5 heavily rely on work of Sansour and co-authors (Sansour and Bufler 1992; Sansour and Bednarczyk 1995; Sansour and Wagner 2003b).

5.2 Strain measures of the Cosserat continuum

In the *Cosserat continuum* every material point is assigned a rotation field which is considered to be independent of the displacement. Motivated by the polar decomposition, the rotational part of the deformation is extracted from the deformation gradient tensor by $\mathbf{F} = \mathbf{RU}$, where the rotation tensor $\mathbf{R} \in SO(3)$ and a stretch-type strain measure $\mathbf{U}$ can be distinguished.

In opposition to the definition of the rotation tensor in Sec. 2.1, we consider here $\mathbf{R}$ to be independent of the map $\boldsymbol{\varphi}(\mathbf{X}, t)$ (Eq. 2.1). This also implies that $\mathbf{U}$ is not *a priori* symmetric. Furthermore, whereas classical continua can be described by one strain measure, e.g. by the stretch tensor, the *Cosserat continuum* requires, due to the independent rotation field, a second strain measure.

Let us start with an explicit expression for $\mathbf{R}$ which can be found by using an exponential map (Choquet-Bruhat, DeWitt-Morette and Dillard-Bleick 1982; Dubrovin, Fomenko and Novikov 1984)

$$\mathbf{R}\left(\theta^k, t\right) = \exp\left(\boldsymbol{\Gamma}\right) = \mathbf{1} + \boldsymbol{\Gamma} + \frac{\boldsymbol{\Gamma}^2}{2!} + \frac{\boldsymbol{\Gamma}^3}{3!} + \ \ldots \qquad , \tag{5.1}$$

where $\boldsymbol{\Gamma}\left(\theta^k, t\right) \in so(3)$ which is the so-called *Lie algebra* corresponding to the *Lie group* $SO(3)$. That is $\boldsymbol{\Gamma}$ is a skew-symmetric tensor

$$\boldsymbol{\Gamma} = -\boldsymbol{\Gamma}^T\,, \tag{5.2}$$

with the rotation vector $\boldsymbol{\gamma}\left(\theta^k, t\right)$ as its axial vector

$$\boldsymbol{\Gamma}\left(\theta^k\right) = \boldsymbol{\gamma}\left(\theta^k, t\right) \times \mathbf{1}\,, \tag{5.3}$$

and we arrive at the following expression (*Rodrigues formula*)

$$\mathbf{R}\left(\theta^k, t\right) = \mathbf{1} + \frac{\sin|\boldsymbol{\gamma}|}{|\boldsymbol{\gamma}|}\boldsymbol{\Gamma} + \frac{\cos|\boldsymbol{\gamma}|}{|\boldsymbol{\gamma}|^2}\boldsymbol{\Gamma}^2\,. \tag{5.4}$$

An important property of the rotation tensor $\mathbf{R}$ is that $\boldsymbol{\gamma}$ is an eigen-vector of the rotation tensor

$$\mathbf{R}\boldsymbol{\gamma} = \boldsymbol{\gamma}\,. \tag{5.5}$$

With $\mathbf{R} \in SO(3)$, the following relations hold

$$\mathbf{R}^T\mathbf{R} = \mathbf{1} \qquad \text{and} \qquad \det\mathbf{R} = 1 \qquad \text{and} \qquad \mathbf{R}^T_{,i}\mathbf{R} + \mathbf{R}^T\mathbf{R}_{,i} = \mathbf{0}\,, \tag{5.6}$$

which implies that the tensor products $\mathbf{R}^T\mathbf{R}_{,i}$ are skew-symmetric and elements of $so(3)$.

The axial vector of $\mathbf{R}^T\mathbf{R}_{,i}$ is then expressed by

$$\mathbf{k}_i\left(\theta^k, t\right) = \text{axial}\left(\mathbf{R}^T\mathbf{R}_{,i}\right) = -\frac{1}{2}\boldsymbol{\epsilon} : \left(\mathbf{R}^T\mathbf{R}_{,i}\right)\,. \tag{5.7}$$

One may elaborate the relation

$$\mathbf{k}_i\left(\theta^k, t\right) = \frac{\sin|\boldsymbol{\gamma}|}{|\boldsymbol{\gamma}|}\boldsymbol{\gamma}_{,i} + \frac{1-\cos|\boldsymbol{\gamma}|}{|\boldsymbol{\gamma}|^2}\boldsymbol{\gamma}_{,i}\times\boldsymbol{\gamma} + \left(\frac{1}{|\boldsymbol{\gamma}|} - \frac{\sin|\boldsymbol{\gamma}|}{|\boldsymbol{\gamma}|^2}\right)\frac{\left(\boldsymbol{\gamma}\cdot\boldsymbol{\gamma}_{,i}\right)}{|\boldsymbol{\gamma}|}\boldsymbol{\gamma}\,. \tag{5.8}$$

As a result we have together with the stretch-type tensor $\mathbf{U}$ (Eringen and Kafadar 1976) or so-called *first Cosserat strain tensor* (Sansour and Bednarczyk 1995)

$$\mathbf{U}\left(\theta^k, t\right) = \mathbf{R}^T\mathbf{F} \tag{5.9}$$

another strain measure which is the so-called *second Cosserat strain tensor*

$$\mathbf{K}\left(\theta^k, t\right) = \mathbf{k}_i\otimes\mathbf{G}^i = -\frac{1}{2}\boldsymbol{\epsilon} : \left(\mathbf{R}^T\mathbf{R}_{,i}\right)\otimes\mathbf{G}^i\,. \tag{5.10}$$

It is worth mentioning that the classical stretch tensor and the *first Cosserat strain tensor* are obviously different from a physical point of view, but also their definitions indicate a clear distinction. That is, the classical stretch tensor is symmetric and solely defined by the deformation map $\boldsymbol{\varphi}(\mathbf{X}, t)$ (Eq. 2.1), whereas the *first Cosserat strain tensor* makes use of the orthogonal rotation tensor $\mathbf{R}$ which is assumed to be independent of this deformation map.

In the following we want to confine ourselves to the quasi-static case and consider no time dependency.

5.3 Variation of the rotation group

Since the rotation field $\mathbf{R}$ is an element of the *Lie group* $SO(3)$, we have to take into account a certain multiplicative structure. Generally, the deformation in the *Cosserat continuum* is assumed such that every point $P \in \mathcal{B}$ is associated with a pair $\mathcal{U} = (\mathbf{u},\, \mathbf{R})$ and we consider a set $\mathcal{C}$ which encompasses all admissible configurations of the body $\mathcal{B}$

$$\mathcal{C}\left(\mathcal{B}\right) = \left\{\mathcal{U}\,|\,\mathcal{U} : \mathcal{B} \to \mathbb{E}(3)\times SO(3)\right\}\,, \tag{5.11}$$

where the cross operator denotes here the Cartesian product. That is all elements of $\mathcal{C}$ are thought to be element of a *linear Lie group* and the group operation of two such elements is given by the direct product $(\mathbf{u},\, \mathbf{R})\circ\left(\hat{\mathbf{u}},\, \hat{\mathbf{R}}\right) = \left(\mathbf{u}+\hat{\mathbf{u}},\, \hat{\mathbf{R}}\mathbf{R}\right)$. The neighbourhood of a point of the configuration space defined by the pair $(\mathbf{u},\, \mathbf{R})$ can be described by means of the curve $\mathcal{V}\left(s\right) \subset \mathcal{C}$ parameterized by s with $\mathcal{V}\left(s = s_0\right) = (\mathbf{u},\, \mathbf{R})$:

$$\mathcal{V}\left(s\right) = \left[\mathbf{u} + \left(s - s_0\right)\delta\mathbf{u},\, \exp((s - s_0)\,\mathbf{W})\mathbf{R}\right]\,, \tag{5.12}$$

where we made use of Eq. (5.1) and $\mathbf{W}$ denotes an element of the *Lie algebra* $so(3)$ corresponding to the the rotation field $\mathbf{R}$ which is element of the *Lie group* $SO(3)$. Now the variation of $(\mathbf{u},\, \mathbf{R})$ can be obtained by the derivation of $\mathcal{V}$ with respect to parameter s

$$\begin{aligned}(\delta\mathbf{u},\, \delta\mathbf{R}) &= \frac{\partial}{\partial s}\mathcal{V}(s)\,|_{s=s_0} = \\ &= \frac{\partial}{\partial s}\left[\mathbf{u} + (s-s_0)\,\delta\mathbf{u},\, \exp((s-s_0)\,\mathbf{W})\mathbf{R}\right]|_{s=s_0} = (\delta\mathbf{u},\, \mathbf{WR})\ . \end{aligned} \tag{5.13}$$

$\mathbf{WR}$ defines the left tangent vector in the tangent space of $SO(3)$ as it was obtained by making use of the so-called left group action. Accordingly, one can consider the right group action

$$\begin{aligned}(\delta\mathbf{u},\, \delta\mathbf{R}) &= \frac{\partial}{\partial s}\mathcal{V}(s)\,|_{s=s_0} = \\ &= \frac{\partial}{\partial s}\left[\mathbf{u} + (s-s_0)\,\delta\mathbf{u},\, \mathbf{R}\exp((s-s_0)\,\mathbf{Y})\right]|_{s=s_0} = (\delta\mathbf{u},\, \mathbf{RY})\ , \end{aligned} \tag{5.14}$$

which results in the right tangent vector $\mathbf{RY}$. $\mathbf{W}$ is related to $\mathbf{Y}$ by

$$\mathbf{W} = \mathbf{RYR}^T\,. \tag{5.15}$$

For the quasi-static case it is sufficient to restrict ourselves to left variations which are simply denoted by $\delta\mathbf{R} = \mathbf{WR}$ in the following. Note that the pair $(\delta\mathbf{u},\, \mathbf{W})$ defines an infinitesimal deformation which is superimposed to valid deformation state $(\mathbf{u},\, \mathbf{R})$ by the group operation $(\mathbf{u},\, \mathbf{R}) \circ (\delta\mathbf{u},\, \mathbf{W}) = (\mathbf{u} + \delta\mathbf{u},\, \mathbf{WR})$.

Now, we can immediately write the variation of the *first Cosserat strain tensor* $\mathbf{U}$ (Eq. 5.9) as

$$\begin{aligned}\delta\mathbf{U} &= \delta\left(\mathbf{R}^T\mathbf{x}_{,i}\right) \otimes \mathbf{G}^i = \\ &= -\mathbf{R}^T\mathbf{W}\left(\mathbf{x}_{,i} \otimes \mathbf{G}^i\right) + \mathbf{R}^T\left(\delta\mathbf{x}_{,i} \otimes \mathbf{G}^i\right)\ . \end{aligned} \tag{5.16}$$

In order to proceed with the variation of $\mathbf{k}_i$ (Eq. 5.7) we additionally consider a vector $\mathbf{w}$ to be the axial vector of the skew-symmetric tensor $\mathbf{W}$ and we have as left variation

$$\delta\mathbf{k}_i = \text{axial}\left[\delta\left(\mathbf{R}^T\mathbf{R}_{,i}\right)\right] = \mathbf{R}^T\mathbf{w}_{,\,i}\,. \tag{5.17}$$

5.4 The weak form and its corresponding equilibrium equations

Let us consider a non-linear boundary value problem on domain $\mathcal{B}$ with boundary $\partial\mathcal{B}$. Dirichlet boundary conditions are prescribed on $\partial\mathcal{B}_D \subset \partial\mathcal{B}$ and Neumann boundary conditions

are prescribed on $\partial\mathcal{B}_N = \partial\mathcal{B} \setminus \partial\mathcal{B}_D$. Let us assume a hyperelastic material behaviour and

$$\rho_0\psi(\mathbf{U},\mathbf{K}) = \rho_0\,\psi^I(\mathbf{U}) + \frac{l^2}{12}\,\rho_0\,\psi^{II}(\mathbf{K}) \tag{5.18}$$

define the stored strain energy per unit undeformed volume which is considered to be a decoupled function of the two *Cosserat strain tensors* $\mathbf{U}$ and $\mathbf{K}$, respectively. l is the so-called *characteristic length* of the couple stress theory and has the dimension of length. Motivated by Sec. 6 the incorporation of l into the stored energy function is achieved by the integration over an assumed one-dimensional micro-continuum $\mathcal{S}$ with the coordinate chart ζ in the limits $\zeta = \left[-\frac{l}{2};\,\frac{l}{2}\right]$:

$$\rho_0\psi(\mathbf{U},\mathbf{K}) = \frac{1}{l}\int_{-\frac{l}{2}}^{\frac{l}{2}} \rho_0\,\psi^I(\mathbf{U})\;\,d\zeta + \frac{1}{l}\int_{-\frac{l}{2}}^{\frac{l}{2}} \zeta^2\,\rho_0\,\psi^{II}(\mathbf{K})\;\,d\zeta\,, \tag{5.19}$$

where $\rho_0\,\psi^I(\mathbf{U})$ and $\rho_0\,\psi^{II}(\mathbf{K})$ are considered to be independent of ζ. Then the internal potential, which is a functional of the *first Cosserat strain tensor* $\mathbf{U}$ and the *second Cosserat strain tensor* $\mathbf{K}$, is given in the Lagrangian form by

$$\Psi = \int_{\mathcal{B}} \left\{\; \rho_0\,\psi^I(\mathbf{U}) + \frac{l^2}{12}\,\rho_0\,\psi^{II}(\mathbf{K}) \;\right\} dV\,. \tag{5.20}$$

Furthermore, we have conjugate to $\mathbf{U}$ and $\mathbf{K}$ the force stress tensor $\boldsymbol{n}$ and the couple stress tensor $\boldsymbol{m}$, respectively, which are defined as follows

$$\boldsymbol{n} = \rho_0\,\frac{\partial\psi^I(\mathbf{U})}{\partial\mathbf{U}} \qquad \text{and} \qquad \boldsymbol{m} = \frac{l^2}{12}\,\rho_0\frac{\partial\psi^{II}(\mathbf{K})}{\partial\mathbf{K}}\,. \tag{5.21}$$

Note that both stress tensors are generally non-symmetric. Corresponding to the internal potential let $\mathcal{W}_{ext}$ define the external virtual work in the Lagrangian form as follows

$$\mathcal{W}_{ext} = \int_{\mathcal{B}} \rho_0\,\mathbf{b}\cdot\delta\mathbf{u}\;dV + \int_{\mathcal{B}} \rho_0\,\mathbf{l}\cdot\mathbf{w}\;dV + \int_{\partial\mathcal{B}_N} \mathbf{t}^{(\mathbf{n})}\cdot\delta\mathbf{u}\;dA + \tag{5.22}$$

$$+ \int_{\partial\mathcal{B}_N} \mathbf{q}^{(\mathbf{n})}\cdot\mathbf{w}\;dV \tag{5.23}$$

where the vectors $\mathbf{b}$, $\mathbf{l}$ are the external body force and torque, respectively, and the vectors $\mathbf{t}^{(\mathbf{n})}$, $\mathbf{q}^{(\mathbf{n})}$ are the corresponding quantities on the boundary. The virtual rotation vector $\mathbf{w}$ is conjugate to the external torque.

For the static case and considering only mechanical processes the *first law of thermodynamics* provides the following variational statement

$$\delta\Psi - \mathcal{W}_{ext} = 0\,, \tag{5.24}$$

which can be written with Eq. (5.20) and Eq. (5.23) as

$$\int_{\mathcal{B}} \left\{ \rho_0 \, \frac{\partial \psi^I_{int}\,(\mathbf{U})}{\partial \mathbf{U}} : \delta\mathbf{U} + \frac{l^2}{12}\,\rho_0 \frac{\partial \psi^{II}_{int}\,(\mathbf{K})}{\partial \mathbf{K}} : \delta\mathbf{K} \right\} dV - \mathcal{W}_{ext} = 0 \tag{5.25}$$

Making use of the expressions for the stress measures (Eq. 5.21) and the variational forms of both *Cosserat* strain tensors (Eq. 5.16) and (Eq. 5.17), respectively, the above functional takes its final form

$$\int_{\mathcal{B}} \left\{ \mathbf{R}\boldsymbol{n}\mathbf{G}^i \cdot \delta\mathbf{u}_{,i} - \mathbf{R}\boldsymbol{n}\mathbf{F}^T : \mathbf{W} + \mathbf{R}\boldsymbol{m}\mathbf{G}^i \cdot \mathbf{w}_{,i} \right\} dV - \mathcal{W}_{ext} = 0\,. \tag{5.26}$$

Applying *Gauss's divergence theorem* we can redraft the above functional as follows

$$\begin{aligned} &- \int_{\mathcal{B}} \frac{1}{\sqrt{G}} \left(\sqrt{G}\,\mathbf{R}\boldsymbol{n}\mathbf{G}^i \right)_{,i} \cdot \delta\mathbf{u}\; dV + \int_{\partial\mathcal{B}} \mathbf{R}\boldsymbol{n}\,\mathbf{n} \cdot \delta\mathbf{u}\; dA - \int_{\mathcal{B}} \mathbf{x}_{,i} \times \mathbf{R}\boldsymbol{n}\mathbf{G}^i \cdot \mathbf{w}\; dV - \\ &\quad - \int_{\mathcal{B}} \frac{1}{\sqrt{G}} \left(\sqrt{G}\,\mathbf{R}\boldsymbol{m}\mathbf{G}^i \right)_{,i} \cdot \mathbf{w}\; dV + \int_{\partial\mathcal{B}} \mathbf{R}\boldsymbol{m}\,\mathbf{n} \cdot \mathbf{w}\; dA - \mathcal{W}_{ext} = 0\,. \end{aligned} \tag{5.27}$$

where G is the determinate of the *Riemannian* metric coefficients (Eq. 2.13) and where we take into account the following expression

$$\begin{aligned} -\mathbf{R}\boldsymbol{n}\mathbf{F}^T : \mathbf{W} &= -\mathbf{R}\boldsymbol{n}\mathbf{G}^i \otimes \mathbf{x}_{,i} : \mathbf{W} = -\mathbf{R}\boldsymbol{n}\mathbf{G}^i \cdot \mathbf{W}\mathbf{x}_{,i} = -\mathbf{R}\boldsymbol{n}\mathbf{G}^i \cdot \mathbf{w} \times \mathbf{x}_{,i} = \\ &= -\mathbf{x}_{,i} \times \mathbf{R}\boldsymbol{n}\mathbf{G}^i \cdot \mathbf{w}\,. \end{aligned} \tag{5.28}$$

Note that here and throughout this section the basis vectors $\mathbf{G}_i$ are considered to be independent of θ^k. Since $\delta\mathbf{u}$ and $\mathbf{w}$ are arbitrary functions, the local statements of the governing equations of this functional, which are the equilibrium equations, are expressed by

$$-\frac{1}{\sqrt{G}} \left(\sqrt{G}\,\mathbf{R}\boldsymbol{n}\mathbf{G}^i \right)_{,i} - \rho_0\,\mathbf{b} = \mathbf{0}\,, \quad \text{in } \mathcal{B} \tag{5.29}$$

$$-\mathbf{x}_{,i} \times \mathbf{R}\boldsymbol{n}\mathbf{G}^i - \frac{1}{\sqrt{G}} \left(\sqrt{G}\,\mathbf{R}\boldsymbol{m}\mathbf{G}^i \right)_{,i} - \rho_0\,\mathbf{l} = \mathbf{0}\,, \quad \text{in } \mathcal{B}\,. \tag{5.30}$$

The corresponding natural boundary conditions are written as

$$\mathbf{R}\boldsymbol{n}\,\mathbf{n} = \mathbf{t}^{(\mathbf{n})} \qquad \text{and} \qquad \mathbf{R}\boldsymbol{m}\,\mathbf{n} = \mathbf{q}^{(\mathbf{n})}\,, \quad \text{on } \partial\mathcal{B}_N\,, \tag{5.31}$$

whereas the essential boundary conditions are given by

$$\mathbf{u} = \mathbf{h}_{\mathbf{u}} \qquad \text{and} \qquad \boldsymbol{\gamma} = \mathbf{h}_{\boldsymbol{\gamma}}\,, \quad \text{on } \partial\mathcal{B}_D\,. \tag{5.32}$$

5.5 Multiplicative updating of the rotation field

The simulation of a non-linear deformation process is performed as a sequence of loading or time steps. In case of a static simulation, for each step i an external loading increment is applied. The discretization of our problem as described in functional (Eq. 5.47) results in a set of non-linear algebraic equations $\mathbf{G}(\mathbf{u}, \mathbf{R}) = \mathbf{0}$ which are in our case the equilibrium equations at the particles. These equations can be approximated by a Taylor expansion in the vicinity of certain known displacement field $\mathbf{u}_0$ and rotation field $\mathbf{R}_0$ as follows

$$\mathbf{G}(\mathbf{u}, \mathbf{R}) = \mathbf{G}(\mathbf{u}_0, \mathbf{R}_0) + \left.\frac{\partial \mathbf{G}(\mathbf{u}, \mathbf{R})}{\partial \mathbf{u}}\right|_{\mathbf{u}_0} \Delta\mathbf{u} + \left.\frac{\partial \mathbf{G}(\mathbf{u}, \mathbf{R})}{\partial \mathbf{R}}\right|_{\mathbf{R}_0} \Delta\mathbf{R} = \mathbf{0}\,, \tag{5.33}$$

where higher order terms are neglected. $\Delta\mathbf{u}$ is the incremental displacement field and $\Delta\mathbf{R}$ the incremental rotation tensor which is computed with the help of Eq. (5.4) involving the incremental rotation vector $\Delta\boldsymbol{\gamma}$.

Due to the problem's non-linear nature it is solved by some form of iteration procedure such as the *Newton-Raphson method*. The iteration process involves several iteration steps j, where for a state of equilibrium $\mathbf{G}_{i+1}^{j+1} = \mathbf{0}$ the increments of the kinematical fields $\Delta\mathbf{u}^j$ and $\Delta\boldsymbol{\gamma}^j$ are determined. The total displacement field is updated after each iteration step by relying on its additive structure

$$\mathbf{u}_{i+1}^{j+1} = \mathbf{u}_{i+1}^{j} + \Delta\mathbf{u}^j\,. \tag{5.34}$$

The new rotation tensor however, is computed by a multiplicative updating scheme, considering that $\mathbf{R}$ is element of the *Lie* group $SO(3)$, where we have to take into account a certain multiplicative structure. Considering the increment of the rotation vector $\Delta\boldsymbol{\gamma}$ to be the axial vector of a skew-symmetric tensor $\Delta\boldsymbol{\Gamma} \in so(3)$, the linearization of the rotation tensor can be carried out according to its variation (Eq. 5.13) as $\Delta\mathbf{R} = \Delta\boldsymbol{\Gamma}\mathbf{R}$. Similarly, the updating of the total rotation tensor can be achieved by left multiplication after each iteration step j as follows

$$\mathbf{R}_{i+1}^{j+1} = \Delta\mathbf{R}^j\,\mathbf{R}_{i+1}^{j}\,. \tag{5.35}$$

Hence, the multiplicative structure of the rotational group is preserved.

A remaining issue is however, how to update the rotation vector. This is as the rotation tensor $\mathbf{R}$ can not be approximated, but only the corresponding rotation vector $\boldsymbol{\gamma}$. The same applies to the incremental rotation tensor $\Delta\mathbf{R}$. A first approach (Simo and Vu-Quoc 1992) is to approximate only the rotation vector increment $\Delta\boldsymbol{\gamma}^j$ at all integration points. Then the $\Delta\mathbf{R}^j$ can be evaluated using Eq. (5.4). The rotation tensor of the previous iteration step $\mathbf{R}_{i+1}^{j}$ is stored as a history variable for all integration points and the updated rotation tensor can therefore be computed with the help of Eq. (5.35). Note, in the reference configuration we have $\mathbf{R} = \mathbf{1}$. Drawbacks of this idea are that only the the increment of the rotation field $\Delta\boldsymbol{\gamma}^j$ can be approximated and the updated rotation field $\mathbf{R}_{i+1}^{j+1}$ is only available as history

variable at the integration points. In particular, it has been observed that this algorithm is not path-independent (Jelenic and Crisfield 1999).

In order to circumvent the path-dependency the total rotation field $\boldsymbol{\gamma}$ has to be approximated and it has been found that the use of spinors allows to update the total rotation field at the nodes (Sansour and Wagner 2003b). In the following the spinor theory as well as the rotation updating algorithm itself is briefly outlined. For more detailed information on the spinor theory the reader is referred to Hestens (1990).

Let us first consider the spinor notation of the rotation tensor $\mathbf{R}$ which is expressed in the *Eulerian* form as follows

$$\mathbf{R} \equiv \alpha + i\boldsymbol{\beta}\,, \qquad \mathbf{R}^T \equiv \alpha - i\boldsymbol{\beta} \tag{5.36}$$

with

$$\alpha = \cos\left(\frac{|\boldsymbol{\gamma}|}{2}\right)\,, \qquad \boldsymbol{\beta} = \sin\left(\frac{|\boldsymbol{\gamma}|}{2}\right)\frac{\boldsymbol{\gamma}}{|\boldsymbol{\gamma}|}\,, \tag{5.37}$$

where i is a complex number with $i^2 = -1$. Note that here the operation $(+)$ is not the usual addition of scalars or vectors. In order to update the rotation field $\mathbf{R}^j_{i+1}$ by an rotation field increment $\Delta\mathbf{R}^j$ using the spinor methodology we first consider the following expressions

$$\mathbf{R}^j_{i+1} \equiv \alpha_1 + i\boldsymbol{\beta}_1 \quad \text{and} \quad \Delta\mathbf{R}^j \equiv \alpha_2 + i\boldsymbol{\beta}_2 \quad \text{and} \quad \mathbf{R}^{j+1}_{i+1} \equiv \alpha_3 + i\boldsymbol{\beta}_3 \tag{5.38}$$

with

$$\alpha_1 = \cos\left(\frac{|\boldsymbol{\gamma}^j_{i+1}|}{2}\right)\,, \qquad \boldsymbol{\beta}_1 = \sin\left(\frac{|\boldsymbol{\gamma}^j_{i+1}|}{2}\right)\frac{\boldsymbol{\gamma}^j_{i+1}}{|\boldsymbol{\gamma}^j_{i+1}|}\,, \tag{5.39}$$

$$\alpha_2 = \cos\left(\frac{|\Delta\boldsymbol{\gamma}^j|}{2}\right)\,, \qquad \boldsymbol{\beta}_2 = \sin\left(\frac{|\Delta\boldsymbol{\gamma}^j|}{2}\right)\frac{\Delta\boldsymbol{\gamma}^j}{|\Delta\boldsymbol{\gamma}^j|} \tag{5.40}$$

$$\alpha_3 = \cos\left(\frac{|\boldsymbol{\gamma}^{j+1}_{i+1}|}{2}\right)\,, \qquad \boldsymbol{\beta}_3 = \sin\left(\frac{|\boldsymbol{\gamma}^{j+1}_{i+1}|}{2}\right)\frac{\boldsymbol{\gamma}^{j+1}_{i+1}}{|\boldsymbol{\gamma}^{j+1}_{i+1}|}\,. \tag{5.41}$$

The resulting rotation field $\mathbf{R}^{j+1}_{i+1}$ in spinor notation is now computed by a so-called *geometric product* of two spinors

$$\begin{aligned}
\alpha_3 + i\boldsymbol{\beta}_3 &= (\alpha_1 + i\boldsymbol{\beta}_1)(\alpha_2 + i\boldsymbol{\beta}_2) = \\
&= \alpha_1\alpha_2 + \alpha_1 i\boldsymbol{\beta}_2 + \alpha_2 i\boldsymbol{\beta}_1 + i^2(\boldsymbol{\beta}_1\cdot\boldsymbol{\beta}_2 + i(\boldsymbol{\beta}_1\times\boldsymbol{\beta}_2)) = \\
&= (\alpha_1\alpha_2 - \boldsymbol{\beta}_1\cdot\boldsymbol{\beta}_2) + i(\alpha_1\boldsymbol{\beta}_2 + \alpha_2\boldsymbol{\beta}_1 - \boldsymbol{\beta}_1\times\boldsymbol{\beta}_2)\,.
\end{aligned} \tag{5.42}$$

With the help of Eq. (5.41) we can extract the new rotation vector $\boldsymbol{\gamma}_{i+1}^{j+1}$

$$\boldsymbol{\gamma}_{i+1}^{j+1} = \frac{2\arccos(\alpha_3)}{\sin\left[\arccos(\alpha_3)\right]}\boldsymbol{\beta}_3 \tag{5.43}$$

This approach has clearly the advantage that the total rotation field can be approximated at all times during the modelling process in the entire domain, that is not only at the integration points, but also at particles.

In meshfree methods the rotation vector field $\boldsymbol{\gamma}(\mathbf{x}_I)$ at a particle $\mathbf{x}_I$ is not equal to the vector which contains the rotational particle parameters which is denoted by $\mathbf{r}_I$, because the meshfree interpolation functions do not possess the *Kronecker Delta property*. This fact leads to the question whether to update the $\boldsymbol{\gamma}(\mathbf{x}_I)$ or $\mathbf{r}_I$ at the particles. It is found that the spinor updating scheme can be applied to the vector containing the rotational particle parameters as well as to the rotation vector field. This property is advantageous, because the MLS shape functions are not interpolating at the particles. That is, in case of updating the rotation vector $\boldsymbol{\gamma}(\mathbf{x}_I)$, the particle parameters $\mathbf{r}_I$ have to be obtained by solving an equation system which assembles the rotation vector approximation equations

$$\boldsymbol{\gamma}(\mathbf{x}_I) = \sum_{J\in\Lambda} N_J(\mathbf{x}_I)\ \mathbf{r}_J \tag{5.44}$$

at all particles $\mathbf{x}_I$ in the problem domain. Λ is the set of particles which support $\mathbf{x}_I$, $N_J(\mathbf{x}_I)$ is the meshfree shape-function ordinate (Eq. 3.5) of a supporting particle $\mathbf{x}_J$ at particle $\mathbf{x}_I$ and $\mathbf{r}_J$ are the corresponding rotational parameters. Therefore, it is proposed to use this updating algorithm with respect to the particle parameter vector $\mathbf{r}_I$ instead of the rotation field. Note that this distinction does not exist in the finite element method, where the approximated rotation field at a certain particle coincides with its rotational degrees of freedom.

However, two problems still remain unsolved. Firstly, the minimum convergence criterium which is here the norm of the vector which contains the particle parameters of the entire system can occasionally not be considered as strictly as in the algorithm of Simo and Vu-Quoc, and secondly, the simulation becomes unstable, if at a particle $\mathbf{x}_I$ the absolute value of the current corresponding rotational particle parameter vector $|(\mathbf{r}_I)_{i+1}^{j}|$ approaches 2π. It is suspected that in both cases the involved trigonometric functions are the reason for this behaviour. This is because for $|(\mathbf{r}_I)_{i+1}^{j}| \to 2\pi$ as well as for $|(\Delta\mathbf{r}_I)^{j}| \to 0$ the vectors $\boldsymbol{\beta}_1$ (Eq. 5.39) and $\boldsymbol{\beta}_2$ (Eq. 5.40) which hold the direction of the corresponding spinors become null-vectors and the direction $\boldsymbol{\beta}_3$ of the updated vector $(\mathbf{r}_I)_{i+1}^{j+1}$ can not be determined properly anymore. In fact, the new direction $\boldsymbol{\beta}_3$ (Eq. 5.41) becomes ambiguous and is significantly changing during the iteration process, whereas its new absolute value is still correctly determined. This has the effect that also the rotational degrees of freedom vary increasingly from iteration step to iteration step, until finally the divergence criterium is exceeded and the simulation breaks down. In contrast to modelling in the three-dimensional space, this characteristic of the updating algorithm is obviously not critical for the two-dimensional space, because the rotation field is confined in the plain.

5.6 Enforcement of displacement boundary conditions

Corresponding to Sec. 4.2 an augmented modified variational principle can be found so that the displacement boundary conditions on $\partial\mathcal{B}_D$ (Eq. 5.32) are part of the original problem functional (Eq. 5.26). For this we modify the problem formulation as follows

$$\delta\Psi + \int_{\partial\mathcal{B}_D} \delta\left(\boldsymbol{\lambda}\cdot(\mathbf{u}-\mathbf{h}_\mathbf{u})\right)\, dV - \mathcal{W}_{ext} = 0\,. \tag{5.45}$$

where $\boldsymbol{\lambda}$ are some set of mathematical functions. If this functional is transferred back to the global equilibrium equation (Eq. 5.27), the unknown mathematical functions $\boldsymbol{\lambda}$ can be identified as the following physical quantity

$$\boldsymbol{\lambda} = -\mathbf{R}\boldsymbol{n}\,\mathbf{n}\,. \tag{5.46}$$

The modified variational principle takes its final form as follows

$$\begin{aligned}\int_\mathcal{B} \left\{ \mathbf{R}\boldsymbol{n}\mathbf{G}^i\cdot\delta\mathbf{u}_{,i} - \mathbf{R}\boldsymbol{m}\mathbf{F}^T : \mathbf{W} + \mathbf{R}\boldsymbol{m}\mathbf{G}^i\cdot\mathbf{w}_{,i}\right\}\, dV - \int_{\partial\mathcal{B}_D}\delta\left(\mathbf{R}\boldsymbol{n}\,\mathbf{n}\right)\cdot(\mathbf{u}-\mathbf{h}_\mathbf{u})\, dV - \\ - \int_{\partial\mathcal{B}_D}\mathbf{R}\boldsymbol{n}\,\mathbf{n}\cdot\delta\mathbf{u}\, dV + \int_{\partial\mathcal{B}_D}\beta\left(\zeta^1,\,\zeta^2,\,h_{u_i}\right)(\mathbf{u}-\mathbf{h}_\mathbf{u})\cdot\delta\mathbf{u}\, dA - \mathcal{W}_{ext} = 0\,,\end{aligned} \tag{5.47}$$

where the fourth integral expression in Eq. (5.47) is a stabilization term together with the stabilization parameter $\beta\left(\zeta^1,\,\zeta^2,\,h_{u_i}\right)$ which is a function of the coordinates charts ζ^1 and ζ^2 of $\partial\mathcal{B}_D$ and takes different values for each displacement degree of freedom. Note, it is usually presumed that the the test function $\delta\mathbf{u}$ is zero on $\partial\mathcal{B}_D$. Here however, the test function is assumed to be arbitrary on the entire boundary $\partial\mathcal{B}$.

The procedure outlined above could also be utilized to enforce the rotation boundary conditions. However, the physical quantity which is conjugate to the rotation field is very involved and does therefore not seem to be suitable for computational application.

5.7 Numerical examples

Before addressing the examples an initial remark is made with regard to the used numerical pre-conditioner and solver. Generally, the system of algebraic equations which is the result of the evaluation of the problem functional (Eq. 5.47) is usually not adequately conditioned and also asymmetric. Therefore, the right choice of a suitable pre-conditioning and solving method is indispensable. The *Generalized Minimal Residual* method together with the *Gram-Schmidt Orthogonalization* and left pre-conditioning is found to perform excellent. All numerical examples within this section make use of the hyperelastic *Saint-Venant-Kirchhoff* constitutive model which involves as material parameters *Young's modulus* E and *Poisson's ratio* ν.

Epoxy polymeric beams

Bending experiments on epoxy (bisphenol-A epichlorohydrin resin) polymeric micro-beams revealed a size-scale dependency of the resulting deformation (Lam et al. 2003). The authors demonstrated that in contrast to the classical elasticity theory the incorporation of strain gradients enabled to approximate size-dependent behaviour of these small-scale structures. Apparently, the nano-structure influences the macroscopic response of the polymeric specimens so that the heterogeneity of the material has to be addressed in order not to underestimate stress and rigidity. Epoxy polymers consist of molecule chains which are partly crosslinked to a network-type structures, if the side branches of such chains are joined up with other polymer chains. Their morphology is semi-crystalline, that is they form mixtures of small crystals and amorphous material. The amorphous or glass-like part though, exhibits no long range order, and the chains are tangled. The experiment consisted of four different

Figure 5.1: *problem configuration*

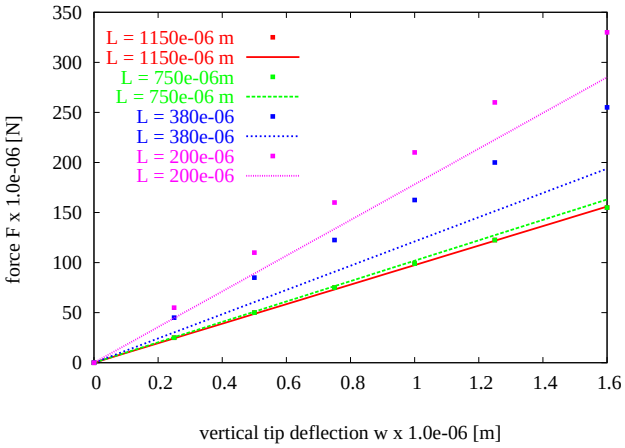

Figure 5.2: *load displacement with diagram* $l = 21\,\mu\,m$ *and* $\nu = 0.3$

micro-cantilever beams of length $L = 1150\,\mu m$, $750\,\mu m$, $380\,\mu m$ and $200\,\mu m$ depicted in Fig. 5.1. The width $b = 235\,\mu m$ and the ratio length to height $L/h = 10$ was kept constant for all four beams. This configuration allowed to compare directly the results of all beams despite their different scaling levels. *Young's modulus* was determined as $E = 1.55\,GPa$, whereas the transversal contraction was found negligible. The experiments did not show strictly linear deformation behaviour, but exhibited some kind of softening in the last third of the deformation process. The relation between different scaling levels to changing rigidity of the beams was clearly non-linear. The strain gradient formulation developed by Lam *et al.* was based on the bending theory of plain strain beams and involved one additional material parameter, a so-called *length scale parameter* l. Their approach provided a fairly accurate match with the experimental data, if this length scale parameter was chosen to $l = 24\,\mu m$.

This bending experiment is now modelled with $31 \times 3 \times 3$ particles in longitudinal and thickness direction, respectively, making use of the modified variational formulation (Eq. 5.47) which also involves a length scale parameter l. In Fig. 5.2 - 5.4 the load-deflection

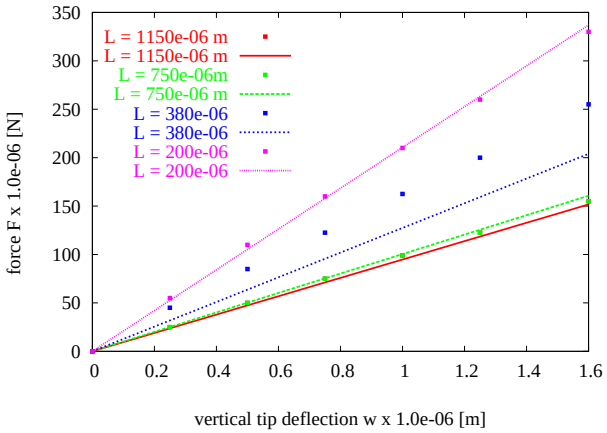

Figure 5.3: *load displacement diagram with* $l = 25\,\mu m$ *and* $\nu = 0$

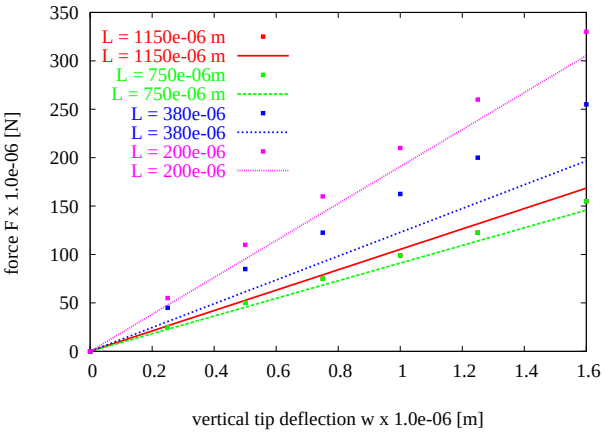

Figure 5.4: *load displacement diagram with* $l = 25\,\mu m$ *and* $\nu = 0.3$

graphs of all four scaling levels of the micro-cantilever beam are combined for micro-length scale parameters $l = 21\,\mu m$ and $l = 25\,\mu m$, respectively. The classical elastic plain strain relation between load and deflection is expressed by

$$w = \frac{1}{3}\frac{FL^3}{bh^3}\frac{12\nu}{E}\,, \tag{5.48}$$

which agrees with the red curves illustrated in Fig. 5.2 to 5.4. Each of the remaining colors represents a different scaling level. The dotted curves are the experimental results and the continuous curves illustrate the results which are simulated. Note that the experimental data indicate no difference for the beams with $L = 1150\,\mu m$ and $750\,\mu m$. In Fig. 5.2 and 5.4 modelling with transversal contraction is illustrated setting *Poisson's ratio* $\nu = 0.3$, while in Fig. 5.3 it is neglected by setting $\nu = 0$. All simulated load-deflection diagrams do not show any non-linearity, which is plausible as deformation and strain are fairly small. The relation between the scaling and the changing rigidity however, is non-linear as it is in the experiment too. The simulated results vary for different length scale parameters as expected, but also the influence of the transversal contraction can not be neglected. Furthermore, there is a difference between linear and non-linear modelling. That is, a preliminary linear simulation actually indicates that the parameter setting $l = 25\,\mu m$ and $\nu = 0.3$ should provide a fairly accurate match with experimental data for the beam with $L = 1150\,\mu m$ and also for $L = 200\,\mu m$. In contrast, the non-linear simulation depicted in Fig. 5.4 shows that this is not the case. Neglecting the transversal contraction illustrated in Fig. 5.3 significantly improves the agreement of simulation with the experiment for the beams with $L = 1150\,\mu m$, $750\,\mu m$ and $200\,\mu m$. But then again, this result is not predicted by the preliminary linear run with $\nu = 0$, which indicates less accuracy than with $\nu = 0.3$. It can be generally stated that the transversal contraction affects the least the beam with $L = 1150\,\mu m$ and most significantly the beam with $L = 200\,\mu m$.

The simulation deviates the most from the experiment for the beam with length $L = 380\,\mu m$. Overall, no parameter setting for ν and l can be found which provides an accurate

match between modelled and experimentally obtained tip-deflection for all scaling levels. This might indicate that the micro-structural behaviour is not fully characterized by rotations only.

Finally, the modelling of the micro-cantilever beams is undertaken without the stabilization term of Eq. (5.47). This is beneficial, because its incorporation heavily affects the result of the simulation. That is, the solution for the cantilever's tip deflection varies up to 100% depending on the magnitude of the penalty parameters. Without the penalty term the boundary enforcement is somewhat limited, but not substantially.

Micro-films

The second example is a thin square sheet which is clamped at all its four edges depicted in Fig. 5.5. Due to the symmetry only one quarter of the sheet is modelled with $11 \times 11 \times 3$ particles in longitudinal and thickness direction, respectively, applying the appropriate symmetry conditions for displacement and rotation. The material is chosen to be the same as for the micro-cantilever beam, except that the *Poisson ratio* is kept constant at $\nu = 0.3$. Four different scaling levels are simulated with $L = 6.0\,mm$, $3.0\,mm$, $1.2\,mm$ and $0.6\,mm$ using the modified variational formulation (Eq. 5.47). The ratio $L/h = 300$ is fixed for all four plates so that all results are directly comparable. The classical solution denoted by the red line in all graphs Fig. 5.6 - 5.9 is obtained using the Green strain tensor based model (Eq. 4.11) presented in Sec. 4.2. The results depicted in Fig. 5.6 and Fig. Fig. 5.7

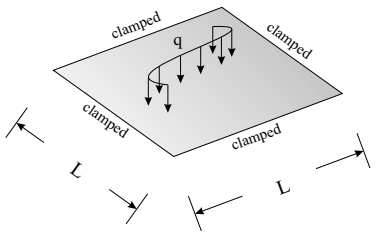

Figure 5.5: *problem configuration*

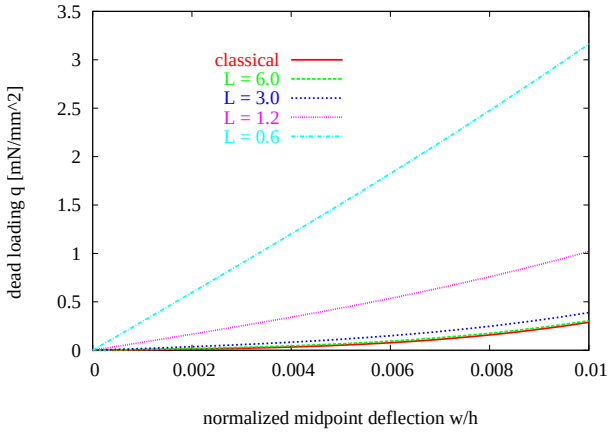

Figure 5.6: *displacement diagram with displacement boundary conditions*

are achieved by fixing only all displacement but not the rotational degrees of freedom at the outer edges of the plate. The load-deflection graph in Fig. 5.6 illustrates that in the first stage of the simulation the rigidity of the clamped plate is increasing for smaller scaling levels. In the subsequent modelling process displayed in Fig. 5.7 the increased rigidity relative to the classical solution is again decreasing and eventually turning into a rigidity regime which is of lower magnitude than the classical reference solution. The crossing point however, where

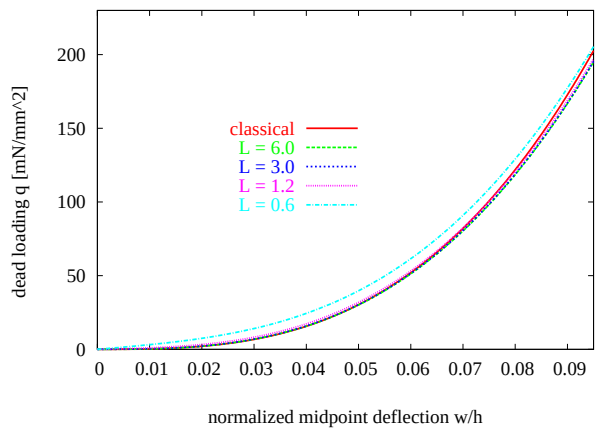

Figure 5.7: *displacement diagram with displacement boundary conditions*

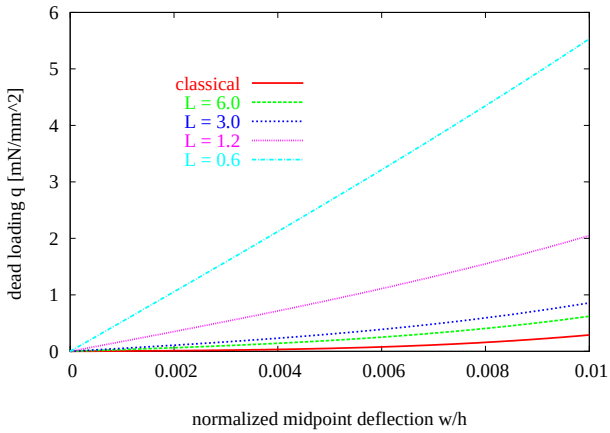

Figure 5.8: *displacement diagram with displacement and rotation boundary conditions*

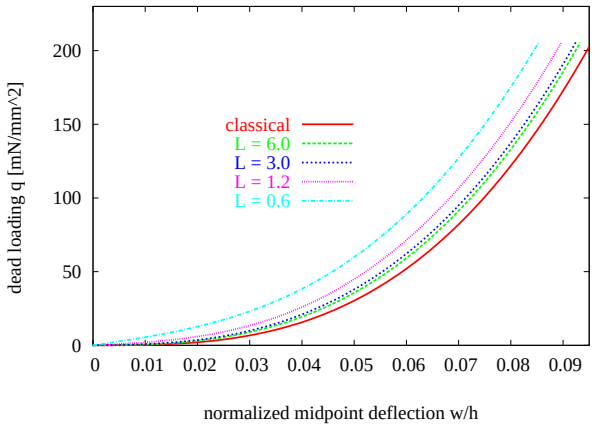

Figure 5.9: *displacement diagram with displacement and rotation boundary conditions*

the curves of the non-classical and classical solution meet, is increasingly delayed for the smaller scaling levels.

Holding also all three rotational degrees of freedom at the outer edges of the plate leads somewhat different results depicted in Fig. 5.8 and Fig. 5.9. The additional rotational boundary conditions have the effect that the stiffness increase for smaller scaling levels is much higher than without these rotational boundary conditions. Furthermore, the load-deflection curves illustrated in Fig. 5.9 do not indicate a declining rigidity relative to the classical solution.

The enforcement of the essential boundary conditions in this example is somewhat critical, because the incorporation of the stabilization term into the augmented modified varia-

tional principle Eq. (5.26) has the effect that the solution for the displacement field noticeably varies depending on the magnitude of the stabilization parameters. Note, that the magnitude of the augmentation is controlled by a numerical boundary enforcement error tolerance δ. This kind of sensitivity is similar to the previous example, however, in case of the clamped plate the augmentation is necessary to provide a stable non-linear modelling. It is also found that the magnitude of the stabilization parameter influences the achieved results of the four scaling levels of the plate differently. In order to have comparable results this set of examples is therefore exclusively modelled using the penalty method with a penalty parameter $\beta = 1.0 \times 10^{15}$. That is all boundary terms except for the stabilization term in Eq. (5.26) are discarded.

Torsion experiments on human bone specimens

Materials such as foam and bones show a porous micro-structure which consists of osteons of $0.15\,mm - 0.25\,mm$ in diameter. Torsion experiments on human bone specimens exhibited a size-dependent elastic response (Yang and Lakes 1981). The authors employed the linear elastic isotropic couple stress theory to model experimental results which involved two additional material parameters. These material parameters were related to a so-called internal length scale parameter l which had about the same magnitude as the bone pores. Later on, Aifantis (1999) demonstrated that also his strain gradient approach was able to predict these experimental results. His approach incorporated, besides the normal shear strain the second order gradient of the same, the latter of which was associated with another material parameter.

In the following, the experiment is idealized as a set of thin beams with a square cross-section with side length $a = 5.0\,mm$, $2.0\,mm$, $1.0\,mm$ and $0.5\,mm$ depicted in Fig. 5.10. It is not the aim of this study to predict the experimental data, but to show qualitatively that size-scale effects in torsion of thin beams can be modelled applying the proposed modified variational principle (Eq. 5.47) to a MLS-based meshfree method. The ratio of beam length

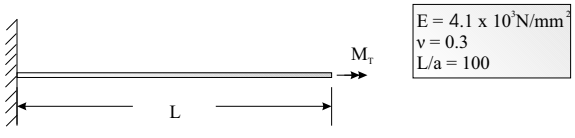

Figure 5.10: *problem configuration*

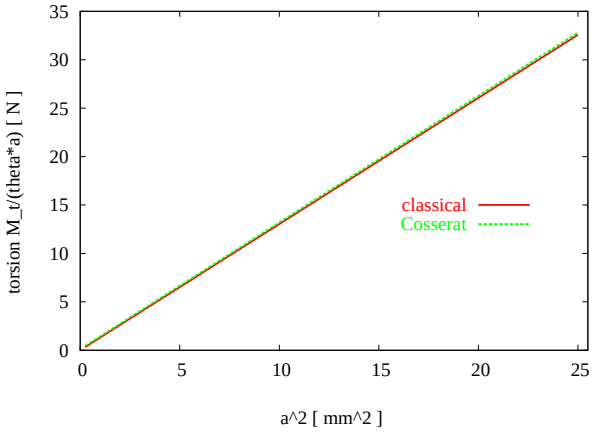

Figure 5.11: *diagram: normalized torsion vs. cross-section size*

to side length $L/a = 100$ is kept constant all four beams so that the results for the twist θ and the corresponding torsion moment M_T are comparable. The torsion moment is applied to the tip of the beam. The opposite end of the beam is clamped, that is all degree displacement degrees of freedom are held over the entire cross-section. The problem is simulated with $21 \times 4 \times 4$ particles in longitudinal and thickness direction, respectively. The internal length scale parameter is assumed as $l = 0.25\,mm$. Note that the enforcement of the essential boundary conditions does not require the incorporation of the stabilization term in Eq. (5.47).

If the twist is considered to be small, then the analytical relation of the applied torsion moment to the resulting twist θ is given by

$$M_T = C\,G\,a^4\,\frac{\theta}{L}\,, \tag{5.49}$$

where C is a constant and $L = 100\,a$. Aifantis as well Yang and Lakis very closely fitted the experimental data with their linear non-classical theories. Plotting the results in graphs with $\frac{M_T}{\theta\,a}$ versus cross-section size a^2 for various bone specimens a slight but distinct difference between classical and non-classical theory was recognizable. Qualitatively equivalent results achieved with the modified variational principle based on the *Cosserat theory* (Eq. 5.47) are depicted in Fig. 5.11, where for all sizes of the beam cross-section, also for the largest, the predictions of classical and *Cosserat* theory indicate a clear difference. Nonlinear modelling

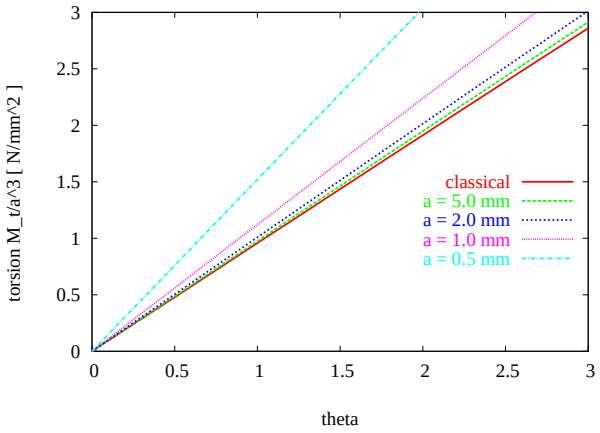

Figure 5.12: *diagram: normalized torsion vs. twist*

however, makes the size-scale effects much more visible as displayed in Fig. 5.12. Here, the classical theory predicts that curves should fall for all side lengths a into one line which is the red curve. In fact, the beams behave stiffer with decreasing cross-section size.

Chapter 6

Generalized Continua

This chapter is dedicated to the development of generalized continuum models for deformation based on the theoretical framework proposed by Sansour (1998b). Its basic principles are in outlined Sec. 6.1. In the following it is demonstrated that by specific definition of the topology of the micro-space this generalized deformation formulation allows for the derivation of strain measures, corresponding equilibrium equations and variational principles for three different cases presented in Sec. 6.2, Sec. 6.3 and Sec. 6.4, respectively. Various computations show that these models are able to address fundamental physical phenomena which are related to the underlying microstructure of the material, in particular scale-effects. The computed results are also compared with the classical *Green strain tensor*-based formulation presented in Sec. 4.2 and clear differences are revealed between classical and non-classical formulations. The modelling is undertaken with the MLS-based meshfree method described in Sec. 3. It is shown that this meshfree method provides the flexibility in terms of the continuity and consistency requirements needed by generalized formulations.

6.1 Generalized deformation

The basic idea is that a generalized continuum $\mathcal{G}$ can be assumed to inherit the mathematical structure of a fibre bundle (see e.g. Choquet-Bruhat et al. 1982). This is in the simplest case the Cartesian product of a macro space $\mathcal{B} \subset \mathbb{E}(3)$ and a micro space $\mathcal{S}$ (Sansour 1998b) which we write as

$$\mathcal{G} := \mathcal{B} \times \mathcal{S} \,. \tag{6.1}$$

This defines the additive structure of the generalized continuum which implies that the integration over the macro- and the micro-continuum can be performed separately. The macro-space $\mathcal{B}$ is parameterized by the curvilinear coordinates θ^i and the micro-space $\mathcal{S}$ by the curvilinear coordinates ζ^α. Here, and in what follows, Greek indices take the values 1, ... or n. The dimension of $\mathcal{S}$ denoted by n is arbitrary, but finite. Furthermore, we want to exclude that the dimension and topology of the micro-space is dependent on θ^i.

Each material point $\tilde{\mathbf{X}} \in \mathcal{G}$ is related to its spatial placement $\tilde{\mathbf{x}} \in \mathcal{G}_t$ at time $t \in \mathbb{R}$ by the mapping

$$\tilde{\boldsymbol{\varphi}}(t) : \mathcal{G} \longrightarrow \mathcal{G}_t \,. \tag{6.2}$$

For convenience but without loss of generality we identify $\mathcal{G}$ with the undeformed reference configuration at a fixed time t_0 in what follows.

The generalized space can be projected to the macro-space in its reference and its current configuration by

$$\pi_0(\tilde{\mathbf{X}}) = \mathbf{X} \qquad \text{and} \qquad \pi_t(\tilde{\mathbf{x}}) = \mathbf{x} \tag{6.3}$$

respectively. The tangent space $\mathcal{TG}$ in the reference configuration is defined by the pair $(\tilde{\mathbf{G}}_i \times \mathbf{I}_\alpha)$ given by

$$\tilde{\mathbf{G}}_i = \frac{\partial \tilde{\mathbf{X}}}{\partial \theta^i} \qquad \text{and} \qquad \mathbf{I}_\alpha = \frac{\partial \tilde{\mathbf{X}}}{\partial \zeta^\alpha} \,, \tag{6.4}$$

where the corresponding dual contra-variant vectors are denoted by $\tilde{\mathbf{G}}^i$ and $\mathbf{I}^\alpha$, respectively. A corresponding tangent space in the current configuration $\mathcal{TG}_t$ is spanned by the pair $(\tilde{\mathbf{g}}_i \times \mathbf{i}_\alpha)$ given by

$$\tilde{\mathbf{g}}_i = \frac{\partial \tilde{\mathbf{x}}}{\partial \theta^i} \qquad \text{and} \qquad \mathbf{i}_\alpha = \frac{\partial \tilde{\mathbf{x}}}{\partial \zeta^\alpha} \,. \tag{6.5}$$

The generalized tangent space can also be projected to its corresponding macro-space by

$$\pi_0^*(\tilde{\mathbf{G}}_i) = \mathbf{G}_i \qquad \text{and} \qquad \pi_t^*(\tilde{\mathbf{g}}_i) = \mathbf{g}_i \tag{6.6}$$

respectively.

The Riemannian metric of the macro tangent space is denoted by $\tilde{\mathbf{G}}$, $\tilde{\mathbf{g}}$ for the reference and the current configuration, respectively. Their co-variant components are given by

$$\tilde{G}_{ij} = \tilde{\mathbf{G}}_i \cdot \tilde{\mathbf{G}}_j \qquad \text{and} \qquad \tilde{g}_{ij} = \tilde{\mathbf{g}}_i \cdot \tilde{\mathbf{g}}_j \tag{6.7}$$

and correspondingly the contra-variant components by

$$\tilde{G}^{ij} = \tilde{\mathbf{G}}^i \cdot \tilde{\mathbf{G}}^j \qquad \text{and} \qquad \tilde{g}^{ij} = \tilde{\mathbf{g}}^i \cdot \tilde{\mathbf{g}}^j \,. \tag{6.8}$$

In the same way we define the Riemannian metric of the micro tangent space denoted by $\mathbf{I}$, $\mathbf{i}$ for the reference and the current configuration respectively. Their co-variant components are given by

$$I_{\alpha\beta} = \mathbf{I}_\alpha \cdot \mathbf{I}_\beta \qquad \text{and} \qquad i_{\alpha\beta} = \mathbf{i}_\alpha \cdot \mathbf{i}_\beta \tag{6.9}$$

and correspondingly the contra-variant components by

$$I^{\alpha\beta} = \mathbf{I}^{\alpha} \cdot \mathbf{I}^{\beta} \qquad \text{and} \qquad i^{\alpha\beta} = \mathbf{i}^{\alpha} \cdot \mathbf{i}^{\beta} \,. \tag{6.10}$$

The determinants of the component matrices of $\mathbf{G}$, $\mathbf{g}$ and $\mathbf{I}$, $\mathbf{i}$ provide the metric coefficients

$$\tilde{G} = \det(\tilde{G}_{ij}) \,, \quad \tilde{g} = \det(\tilde{g}_{ij}) \qquad \text{and} \qquad I = \det(I_{\alpha\beta}) \,, \quad i = \det(i_{\alpha\beta}) \,. \tag{6.11}$$

Now, we choose the placement vector $\tilde{\mathbf{x}}$ of a material point P ($\tilde{\mathbf{X}} \in \mathcal{G}$) to be the sum of its position in the macro-continuum $\mathbf{x} \in \mathcal{B}_t$ and in the micro-continuum $\boldsymbol{\xi} \in \mathcal{S}_t$ as follows

$$\tilde{\mathbf{x}} = \mathbf{x}\left(\theta^k, t\right) + \boldsymbol{\xi}\left(\theta^k, \zeta^\beta, t\right) \,. \tag{6.12}$$

Thereby, the macro-placement vector $\mathbf{x}$ defines the centerpoint of the micro-coordinate system so that the micro-placement $\boldsymbol{\xi}$ is assumed to be relative to the macro-placement. Accordingly, for $t = t_0$ the placement of a material point (Eq. 6.12) takes

$$\tilde{\mathbf{X}} = \mathbf{X}\left(\theta^k\right) + \boldsymbol{\Xi}\left(\theta^k, \zeta^\beta\right) \,, \qquad \text{with } \boldsymbol{\Xi} \in \mathcal{S} \,. \tag{6.13}$$

The micro-motion can be taken to be linear in ζ^α considering it to be very small compared to the macro-motion, a simplification also suggested by Eringen (1999), and we arrive at

$$\tilde{\mathbf{x}} = \mathbf{x}\left(\theta^k, t\right) + \zeta^\alpha \, \mathbf{a}_\alpha\left(\theta^k, t\right) \,. \tag{6.14}$$

The vector functions $\mathbf{a}_\alpha\left(\theta^k, t\right)$ can be viewed as the directors of the micro-continuum with their corresponding micro-coordinates ζ^α, the number of which must be chosen according to a specific topology of the micro-space and the physical properties of a material due to its intrinsic structure. Generally, the vector functions $\mathbf{a}_\alpha\left(\theta^k, t\right)$ can be described with the help of a tensor $\mathbf{A}$ as follows

$$\mathbf{a}_\alpha\left(\theta^k, t\right) = \mathbf{A}\mathbf{I}_\alpha \,. \tag{6.15}$$

Note, if the dimension of $\mathcal{S}$ is three, then we have $\mathbf{A} \in GL^+(3)$ which can be restricted to subgroups as well.

6.2 Generalized continuum based on a triade of normal vectors $\mathbf{n}_\alpha$

In the previous section Sec. 6.1 the basic principles to formulate a generalized deformation field was outlined. In this section this generalized formulation is specified to consist of the macroscopic deformation field and relative to it, a microscopic deformation field which is described by a triad of normal vectors $\mathbf{n}_\alpha$ attached to each material particle and defined by the following expression

$$\tilde{\mathbf{n}}_\alpha\left(\theta^i,t\right) = \frac{1}{2}\,\epsilon_{\alpha\beta\gamma}\,\frac{(\mathbf{g}_\beta\times\mathbf{g}_\gamma)}{|\mathbf{g}_\beta\times\mathbf{g}_\gamma|} = \frac{1}{2}\,\epsilon_{\alpha\beta\gamma}\,\frac{(\mathbf{Fe}_\beta\times\mathbf{Fe}_\gamma)}{\sqrt{(\mathbf{Fe}_\beta\times\mathbf{Fe}_\gamma)\cdot(\mathbf{Fe}_\beta\times\mathbf{Fe}_\gamma)}}\,, \tag{6.16}$$

where $\epsilon_{\alpha\beta\gamma}$ are the components of the *Levi-Civita tensor* (Eq. 2.16) and $|\tilde{\mathbf{n}}_\alpha| = 1$. The basis vectors $\mathbf{g}_\alpha\left(\theta^i,t\right)$ are with regard to the macro-space $\mathcal{B}\subset\mathbb{E}(3)$ defined by Eq. (2.4) and $\mathbf{F}\left(\theta^i,t\right)$ is the corresponding deformation gradient tensor (Eq. 2.5).

The deformation within the micro-continuum which has its origin defined by the macroscopic position vector is therefore characterized by rigid body rotation and shear. This is true, because, firstly, the triad of the normal vectors $\tilde{\mathbf{n}}_\alpha$ rotates corresponding to the changing orientation of the planes $\mathbf{g}_\beta\times\mathbf{g}_\gamma$ to which these vectors are perpetual, and, secondly, because the orientation of those planes to each other is altered according to the deformation of the basis vectors $\mathbf{g}_\beta$.

In this approach the micro-directors $\mathbf{a}_\alpha\left(\theta^i,t\right)$ Eq. (6.14) are replaced by expression Eq. (6.16) and we arrive at

$$\tilde{\mathbf{x}}\left(\theta^i,\zeta^\beta,t\right) = \mathbf{x}\left(\theta^i,t\right) + \zeta^\alpha\,\tilde{\mathbf{n}}_\alpha\left(\theta^i,t\right)\,. \tag{6.17}$$

Note, an advantage of this procedure is that it introduces rotation and shear of a lattice or a particle without involving additional degrees of freedom.

A set of basis vectors for the reference configuration is defined by

$$\tilde{\mathbf{G}}_i\left(\theta^i,\zeta^\beta\right) = \frac{\partial\tilde{\mathbf{X}}}{\partial\theta^i}\,,\qquad \mathbf{I}_\alpha\left(\theta^i\right) = \frac{\partial\tilde{\mathbf{X}}}{\partial\zeta^\alpha} = \tilde{\mathbf{N}}_\alpha\left(\theta^i\right) \tag{6.18}$$

and for the current configuration by

$$\tilde{\mathbf{g}}_i\left(\theta^i,\zeta^\beta,t\right) = \frac{\partial\tilde{\mathbf{x}}}{\partial\theta^i}\,,\qquad \mathbf{i}_\alpha\left(\theta^i,t\right) = \frac{\partial\tilde{\mathbf{x}}}{\partial\zeta^\alpha} = \tilde{\mathbf{n}}_\alpha\left(\theta^i,t\right)\,. \tag{6.19}$$

Furthermore, the spatial derivatives of the position vector in the current configuration with respect to the curvilinear coordinates θ^i of the macro-space are given by

$$\tilde{\mathbf{x}}_{,i}\left(\theta^i,\zeta^\beta,t\right) = \frac{\partial\tilde{\mathbf{x}}}{\partial\theta^i} = \mathbf{x}_{,i}\left(\theta^i,t\right) + \zeta^\alpha\tilde{\mathbf{n}}_{\alpha,i}\left(\theta^i,t\right)\,, \tag{6.20}$$

and with respect to the coordinates of the micro-space by

$$\tilde{\mathbf{x}}_{,\alpha}\left(\theta^i,\zeta^\beta,t\right)=\frac{\partial\tilde{\mathbf{x}}}{\partial\zeta^\alpha}=\tilde{\mathbf{n}}_\alpha\left(\theta^i,t\right)\ . \tag{6.21}$$

Hereby it is important to recognize that $\tilde{\mathbf{n}}_{\alpha,i}$ is constant over $\mathcal{S}$.

With Eq. (6.20) and Eq. (6.21) a generalized deformation gradient is formulated as follows

$$\tilde{\mathbf{F}}\left(\theta^k,\zeta^\beta,t\right)=\left(\mathbf{x}_{,i}\left(\theta^i,t\right)+\zeta^\alpha\tilde{\mathbf{n}}_{\alpha,i}\left(\theta^i,t\right)\right)\otimes\tilde{\mathbf{G}}^i+\tilde{\mathbf{n}}_\alpha\left(\theta^i,t\right)\otimes\tilde{\mathbf{N}}^\alpha\,. \tag{6.22}$$

In the following section we want to restrict ourselves to the static case.

6.2.1 Generalized Cauchy-Green deformation tensor

In order to formulate generalized strain measures based on Eq. (6.17) we compute at first correspondingly to the definition of the classical *Cauchy-Green deformation tensor* the square of the deformed arc length consisting of the macro-components dx^k and the micro-components $d\,\xi^\alpha$

$$d\,\tilde{\mathbf{x}}\left(\theta^i,\zeta^\beta\right)\ =\ \mathbf{x}_{,k}\,d\theta^k+\zeta^\alpha\,\tilde{\mathbf{n}}_{\alpha,k}\,d\theta^k+\tilde{\mathbf{n}}_\alpha\,d\,\xi^\alpha\,. \tag{6.23}$$

Then we calculate the square of the deformed arc as follows

$$\begin{aligned}(d\tilde{s})^2\ &=\ d\,\tilde{\mathbf{x}}\cdot d\,\tilde{\mathbf{x}}=\\ &=\ \left(\mathbf{x}_{,k}\cdot\mathbf{x}_{,l}+\zeta^\alpha\ (\mathbf{x}_{,k}\cdot\tilde{\mathbf{n}}_{\alpha,l}+\tilde{\mathbf{n}}_{\alpha,k}\cdot\mathbf{x}_{,l})+\zeta^\alpha\,\zeta^\beta\,\tilde{\mathbf{n}}_{\alpha,k}\cdot\tilde{\mathbf{n}}_{\beta,l}\right)\ d\theta^k\,d\theta^l+\\ &\quad+\left(\mathbf{x}_{,k}\cdot\tilde{\mathbf{n}}_\beta+\zeta^\alpha\,\tilde{\mathbf{n}}_{\alpha,k}\cdot\tilde{\mathbf{n}}_\beta\right)\ d\theta^k\,d\,\xi^\beta+\left(\tilde{\mathbf{n}}_\alpha\cdot\mathbf{x}_{,l}+\zeta^\beta\,\tilde{\mathbf{n}}_\alpha\cdot\tilde{\mathbf{n}}_{\beta,l}\right)\ d\,\xi^\alpha\ d\theta^l+\\ &\quad+\tilde{\mathbf{n}}_\alpha\cdot\tilde{\mathbf{n}}_\beta\ \ d\,\xi^\alpha\,d\,\xi^\beta\,.\end{aligned} \tag{6.24}$$

Now we can identify three strain measures

$$\tilde{\mathbf{C}}^I\left(\theta^k,\zeta^\beta\right)=\mathbf{x}_{,k}\cdot\mathbf{x}_{,l}+\zeta^\alpha\ (\mathbf{x}_{,k}\cdot\tilde{\mathbf{n}}_{\alpha,l}+\tilde{\mathbf{n}}_{\alpha,k}\cdot\mathbf{x}_{,l})\ \tilde{\mathbf{G}}^k\otimes\tilde{\mathbf{G}}^l \tag{6.25}$$

$$\tilde{\mathbf{C}}^{II}\left(\theta^k,\zeta^\beta\right)=\left(\mathbf{x}_{,k}\cdot\tilde{\mathbf{n}}_\beta+\zeta^\alpha\,\tilde{\mathbf{n}}_{\alpha,k}\cdot\tilde{\mathbf{n}}_\beta\right)\ \left(\tilde{\mathbf{G}}^k\otimes\tilde{\mathbf{N}}^\beta+\tilde{\mathbf{N}}^\beta\otimes\tilde{\mathbf{G}}^k\right) \tag{6.26}$$

$$\tilde{\mathbf{C}}^{III}\left(\theta^k,\zeta^\beta\right)=\left(\tilde{\mathbf{n}}_\alpha\cdot\tilde{\mathbf{n}}_\beta\right)\ \tilde{\mathbf{N}}^\alpha\otimes\tilde{\mathbf{N}}^\beta\,, \tag{6.27}$$

where higher order terms in ζ^α within the first strain measure are regarded as negligible. These three measures can be combined to an unified generalized strain measure

$$\tilde{\mathbf{C}} = \tilde{\mathbf{C}}^I + \tilde{\mathbf{C}}^{II} + \tilde{\mathbf{C}}^{III} \,. \tag{6.28}$$

Leaning on a classical variational formulation based on the *Cauchy-Green deformation tensor* an adjacent approach is to establish a generalized variational principle based on $\tilde{\mathbf{C}}$ and we have

$$\int_{\mathcal{B}} \int_{\mathcal{S}} \tilde{\rho}_0 \, \frac{\partial \psi \left(\tilde{\mathbf{C}} \left(\theta^k, \zeta^\beta \right) \right)}{\partial \tilde{\mathbf{C}}} : \delta \tilde{\mathbf{C}} \, dS \, dV + \mathcal{W}_{ext} = 0 \,, \tag{6.29}$$

where $\tilde{\rho}_0 \, \psi$ is the stored strain energy per unit undeformed volume and $\tilde{\rho}_0$ is the density of the micro-space in the reference configuration.

However, this approach is mathematically very involved due to use of the vector cross product which is utilized to formulate the micro-directors Eq. (6.16). Especially this fact makes it from the computational perspective impractical to pursue.

6.3 Generalized continuum involving the macroscopic basis vectors $\mathbf{g}_\alpha$

In the previous section (Sec. 6.2) it was demonstrated how to formulate a generalized deformation description, which incorporates an oriented micro-continuum, without adding extra degrees of freedom to each material point. However, due to its involved character it is rather impractical to make computational use of this approach.

Another possibility to avoid the incorporation of additional degrees of freedom, other than the displacement degrees of freedom, is to define the directors of the micro-continuum $\mathbf{a}_\alpha$ (6.15) as follows

$$\mathbf{a}_\alpha\left(\theta^k, t\right) = \frac{\partial \mathbf{x}}{\partial \theta^\alpha} = \mathbf{g}_\alpha\left(\theta^k, t\right) , \tag{6.30}$$

where $\mathbf{x} \in \mathcal{B}_t$. Then the generalized deformation field (6.14) takes the following form

$$\tilde{\mathbf{x}}\left(\theta^k, \zeta^\beta, t\right) = \mathbf{x}\left(\theta^k, t\right) + \zeta^\alpha\, \mathbf{g}_\alpha\left(\theta^k, t\right) . \tag{6.31}$$

In the reference configuration we have:

$$\tilde{\mathbf{X}}\left(\theta^k, \zeta^\beta, t\right) = \mathbf{X}\left(\theta^k\right) + \zeta^\alpha\, \mathbf{G}_\alpha\left(\theta^k, t\right) , \qquad \text{with } \mathbf{G}_\alpha\left(\theta^k, t\right) = \frac{\partial \mathbf{X}}{\partial \theta^\alpha} . \tag{6.32}$$

Note, even if the micro-continuum $\mathcal{S}$ is defined by the macroscopic basis vectors $\mathbf{g}_\alpha$, it is important to realize that the dimension of the micro-space does not have to coincide with dimension of the macro-space. The spatial derivatives of the position vector in the current configuration with respect to the macro-coordinates θ^i are given by

$$\tilde{\mathbf{x}}_{,i}\left(\theta^k, \zeta^\beta, t\right) = \frac{\partial \tilde{\mathbf{x}}}{\partial \theta^i} = \mathbf{x}_{,i}\left(\theta^k, t\right) + \zeta^\alpha\, \mathbf{g}_{\alpha,i}\left(\theta^k, t\right) , \tag{6.33}$$

and with respect to the micro-coordinates ζ^α by

$$\tilde{\mathbf{x}}_{,\alpha}\left(\theta^k, t\right) = \frac{\partial \tilde{\mathbf{x}}}{\partial \zeta^\alpha} = \mathbf{g}_\alpha\left(\theta^k, t\right) . \tag{6.34}$$

The generalized deformation gradient tensor is now expressed as follows

$$\tilde{\mathbf{F}}\left(\theta^k, \zeta^\beta, t\right) = \left(\mathbf{x}_{,i}\left(\theta^k, t\right) + \zeta^\alpha\, \mathbf{g}_{\alpha,i}\left(\theta^k, t\right)\right) \otimes \tilde{\mathbf{G}}^i + \mathbf{g}_\alpha\left(\theta^k, t\right) \otimes \mathbf{I}^\alpha . \tag{6.35}$$

6.3.1 Generalized Cauchy-Green deformation tensor

In order to formulate generalized strain measures based on Eq. (6.31) we proceed correspondingly to the definition of the classical *Cauchy-Green deformation tensor*. For this, we first consider a deformed arc length $d\,\tilde{\mathbf{x}}$ consisting of the macro-components dx^k and the micro-components $d\,\xi^\alpha$ and we arrive at

$$d\,\tilde{\mathbf{x}} \;=\; \mathbf{x}_{,k}\,d\theta^k + \zeta^\alpha\,\mathbf{g}_{\alpha,k}\,d\theta^k + \mathbf{g}_\alpha\,d\,\xi^\alpha\,. \tag{6.36}$$

Subsequently, by calculating the square of the deformed arc as

$$\begin{aligned}(d\tilde{s})^2 \;&=\; d\,\tilde{\mathbf{x}}\cdot d\,\tilde{\mathbf{x}} = \\ &= \Big(\mathbf{x}_{,k}\cdot\mathbf{x}_{,l} + \zeta^\alpha\,(\mathbf{x}_{,k}\cdot\mathbf{g}_{\alpha,l} + \mathbf{g}_{\alpha,k}\cdot\mathbf{x}_{,l}) + \zeta^\alpha\,\zeta^\beta\,\mathbf{g}_{\alpha,k}\cdot\mathbf{g}_{\beta,l}\Big)\;\; d\theta^k\,d\theta^l + \\ &\quad + (\mathbf{x}_{,k}\cdot\mathbf{g}_\beta + \zeta^\alpha\,\mathbf{g}_{\alpha,k}\cdot\mathbf{g}_\beta)\;\; d\theta^k\,d\,\xi^\beta + \big(\mathbf{g}_\alpha\cdot\mathbf{x}_{,l} + \zeta^\beta\,\mathbf{g}_\alpha\cdot\mathbf{g}_{\beta,l}\big)\;\; d\,\xi^\alpha\,d\theta^l + \\ &\quad + \mathbf{g}_\alpha\cdot\mathbf{g}_\beta\;\; d\,\xi^\alpha\,d\,\xi^\beta\end{aligned} \tag{6.37}$$

and neglecting higher order terms in ζ^α we can identify three strain measures

$$\tilde{\mathbf{C}}^I = (\mathbf{x}_{,k}\cdot\mathbf{x}_{,l} + \zeta^\alpha\,(\mathbf{x}_{,k}\cdot\mathbf{g}_{\alpha,l} + \mathbf{g}_{\alpha,k}\cdot\mathbf{x}_{,l}))\;\; \tilde{\mathbf{G}}^k\otimes\tilde{\mathbf{G}}^l \tag{6.38}$$

$$\tilde{\mathbf{C}}^{II} = (\mathbf{x}_{,k}\cdot\mathbf{g}_\beta + \zeta^\alpha\,\mathbf{g}_{\alpha,k}\cdot\mathbf{g}_\beta)\;\; \Big(\tilde{\mathbf{G}}^k\otimes\mathbf{I}^\beta + \mathbf{I}^\beta\otimes\tilde{\mathbf{G}}^k\Big) \tag{6.39}$$

$$\tilde{\mathbf{C}}^{III} = (\mathbf{g}_\alpha\cdot\mathbf{g}_\beta)\;\; \mathbf{I}^\alpha\otimes\mathbf{I}^\beta\,. \tag{6.40}$$

These three measures can be combined to an unified generalized strain measure

$$\tilde{\mathbf{C}} = \tilde{\mathbf{C}}^I + \tilde{\mathbf{C}}^{II} + \tilde{\mathbf{C}}^{III} \tag{6.41}$$

which alternatively, could be directly obtained via the formula

$$\tilde{\mathbf{C}} = \tilde{\mathbf{F}}^T\tilde{\mathbf{F}}\,. \tag{6.42}$$

Furthermore, the following relation holds

$$\mathbf{g}_{\alpha,k} = \frac{\partial\mathbf{g}_\alpha}{\partial\theta^k} = \frac{1}{2}\,g^{sl}\,(g_{kl,\alpha} + g_{\alpha l,k} - g_{\alpha k,l})\;\mathbf{g}_s\,. \tag{6.43}$$

where $g_{rs,t}$ are the spatial derivatives of the *Riemannian* metric coefficients g_{ij} (Eq. 2.13). $\tilde{\mathbf{C}}^I$ and $\tilde{\mathbf{C}}^{II}$ consist of strain caused by the deformation of a macro-line element and also

strain which results from a relative deformation between macro- and micro-continuum. $\tilde{\mathbf{C}}^{III}$ however, is a sole micro-strain.

In the reference configuration these strain measures are reduced to

$$\tilde{\mathbf{C}}_0^I = (\mathbf{G}_k \cdot \mathbf{G}_l + \zeta^\alpha \ (\mathbf{G}_k \cdot \mathbf{G}_{\alpha,l} + \mathbf{G}_{\alpha,k} \cdot \mathbf{G}_l)) \ \ \tilde{\mathbf{G}}^k \otimes \tilde{\mathbf{G}}^l \tag{6.44}$$

$$\tilde{\mathbf{C}}_0^{II} = (\mathbf{G}_k \cdot \mathbf{G}_\beta + \zeta^\alpha \, \mathbf{G}_{\alpha,k} \cdot \mathbf{G}_\beta) \ \ \left(\tilde{\mathbf{G}}^k \otimes \mathbf{I}^\beta + \mathbf{I}^\beta \otimes \tilde{\mathbf{G}}^k\right) \tag{6.45}$$

$$\tilde{\mathbf{C}}_0^{III} = (\mathbf{G}_\alpha \cdot \mathbf{G}_\beta) \ \ \mathbf{I}^\alpha \otimes \mathbf{I}^\beta \tag{6.46}$$

which have to be subtracted from their counterparts in the deformed configuration Eq. (6.38)-(6.40) in order to have strain measures which vanish in the reference configuration.

In summary, due to deformation of the micro-directors (Eq. 6.30) the micro-continuum undergoes rotation, stretch and shear and we find an analogy to the so-called *micromorph continuum* (Eringen 1999). However, the micro-directors are hidden in this approach within the generalized deformation formulation (Eq. 6.31) and therefore, no additional degrees of freedom are involved. Any generalized strain measure derived from Eq. (6.31) can only be linear with respect to the micro-coordinate ζ^α, as the generalized deformation is linear in ζ^α. The micro-deformation $\boldsymbol{\xi}$ is obviously dependent on the macro deformation gradient $\operatorname{Grad}\mathbf{x}$, that is, the generalized deformation $\tilde{\mathbf{x}}$ is completely described by the unknown macro-displacement field $\mathbf{u}$ and its first derivatives.

In the following we want to confine ourselves to the quasi-static case and consider no time dependency.

6.3.2 A generalized variational formulation and its corresponding equilibrium equations

In a similar fashion as in Sec. 6.2 a generalized variational principle is established which is based on the generalized strain tensor $\tilde{\mathbf{C}}$. Let us now consider a non-linear boundary value problem in the domain $\mathcal{B} \times \mathcal{S}$ with the boundary $\partial\mathcal{B} \times \mathcal{S}$. The micro-space $\mathcal{S}$ is confined by a corresponding boundary $\partial\mathcal{S}$. Accordingly, we have to distinguished between Dirichlet boundary conditions prescribed on $\partial\mathcal{B}_D \times \mathcal{S} \subset \partial\mathcal{B} \times \mathcal{S}$ denoted by $\tilde{\mathbf{h}}_{\tilde{\mathbf{u}}}^{(\mathbf{n})}$ and such on $\partial\mathcal{B}_D \times \partial\mathcal{S}_D \subset \partial\mathcal{B} \times \partial\mathcal{S}$ denoted by $\tilde{\mathbf{h}}_{\tilde{\mathbf{u}}}^{(\boldsymbol{\nu})}$, where $\mathbf{n}$ defines the normal vector on $\partial\mathcal{B}$ and $\boldsymbol{\nu}$ is the normal vector on $\partial\mathcal{S}$. Correspondingly, Neumann boundary conditions are prescribed on $\partial\mathcal{B}_N \times \mathcal{S} = \partial\mathcal{B} \times \mathcal{S} \setminus \partial\mathcal{B}_D \times \mathcal{S}$ denoted by $\tilde{\mathbf{t}}^{(\mathbf{n})}$ and on $\partial\mathcal{B}_N \times \partial\mathcal{S}_N = \partial\mathcal{B} \times \partial\mathcal{S} \setminus \partial\mathcal{B}_D \times \partial\mathcal{S}_D$ denoted by $\tilde{\mathbf{t}}^{(\boldsymbol{\nu})}$.

Furthermore, let $\mathcal{W}_{ext}$ define the external virtual work in the Lagrangian form as follows

$$\mathcal{W}_{ext}(\mathbf{u}) = -\int_{\mathcal{B}} \mathbf{b}\left(\theta^k\right) \cdot \delta\mathbf{u}\left(\theta^k\right)\ dV - \int_{\mathcal{B}} \mathbf{l}^\alpha\left(\theta^k\right) \cdot \delta\frac{\partial \mathbf{u}\left(\theta^k\right)}{\partial\theta^\alpha}\ dV - \\ - \int_{\partial\mathcal{B}_N} \mathbf{t}^{(\mathbf{n})}\left(\theta^k\right) \cdot \delta\mathbf{u}\left(\theta^k\right)\ dA - \int_{\partial\mathcal{B}_N} \mathbf{q}^{(\mathbf{n})\,\alpha}\left(\theta^k\right) \cdot \delta\frac{\partial \mathbf{u}\left(\theta^k\right)}{\partial\theta^\alpha}\ dA \tag{6.47}$$

where the external body force

$$\mathbf{b}\left(\theta^k\right) = \int_{\mathcal{S}} \tilde{\rho}_0\, \tilde{\mathbf{b}}\left(\theta^k, \zeta^\beta\right)\ dS + \int_{\partial\mathcal{S}} \tilde{\mathbf{b}}^{(\boldsymbol{\nu})}\left(\theta^k, \zeta^\beta\right)\ d\sigma \tag{6.48}$$

and the external body couples

$$\mathbf{l}^\alpha\left(\theta^k\right) = \int_{\mathcal{S}} \zeta^\alpha\ \tilde{\rho}_0\, \tilde{\mathbf{b}}\left(\theta^k, \zeta^\beta\right)\ dS + \int_{\partial\mathcal{S}} \zeta^\alpha\, \tilde{\mathbf{b}}^{(\boldsymbol{\nu})}\left(\theta^k, \zeta^\beta\right)\ d\sigma \tag{6.49}$$

are acting on $\mathcal{B} \times \mathcal{S}$ and $\mathcal{B} \times \partial\mathcal{S}$, respectively. The external traction

$$\mathbf{t}^{(\mathbf{n})}\left(\theta^k\right) = \int_{\mathcal{S}} \tilde{\rho}_0\ \tilde{\mathbf{t}}^{(\mathbf{n})}\left(\theta^k, \zeta^\beta\right)\ dS + \int_{\partial\mathcal{S}_N} \tilde{\mathbf{t}}^{(\boldsymbol{\nu})}\left(\theta^k, \zeta^\beta\right)\ d\sigma \tag{6.50}$$

and the external surface couples

$$\mathbf{q}^{(\mathbf{n})\,\alpha}\left(\theta^k\right) = \int_{\mathcal{S}} \zeta^\alpha\ \tilde{\rho}_0\, \tilde{\mathbf{t}}^{(\mathbf{n})}\left(\theta^k, \zeta^\beta\right)\ dS + \int_{\partial\mathcal{S}_N} \zeta^\alpha\, \tilde{\mathbf{t}}^{(\boldsymbol{\nu})}\left(\theta^k, \zeta^\beta\right)\ d\sigma \tag{6.51}$$

are acting on $\partial\mathcal{B}_N \times \mathcal{S}$ and $\partial\mathcal{B}_N \times \partial\mathcal{S}_N$ respectively. Furthermore, dV is a volume element of the macroscopic domain $\mathcal{B}$, whereas dA is a surface element of its corresponding boundary $\partial\mathcal{B}$, and accordingly, dS is a volume element of the microscopic domain $\mathcal{S}$, whereas $d\sigma$ is a surface element of its corresponding boundary $\partial\mathcal{S}$. The density of the micro-space in the reference configuration is denoted by $\tilde{\rho}_0$ and the density of the macro-space is consequently expressed by

$$\rho_0 = \int_{\mathcal{S}} \tilde{\rho}_0\ dS\,. \tag{6.52}$$

In the following external loading applied on $\mathcal{B} \times \partial\mathcal{S}$ as well as on $\partial\mathcal{B}_N \times \partial\mathcal{S}_N$ is discarded.

Furthermore, we assume now that the body under consideration $\mathcal{B} \times \mathcal{S}$ is hyperelastic and possesses an elastic potential Ψ represented by the stored strain energy per unit undeformed volume $\tilde{\rho}_0\,\psi$. If the material is in addition homogeneous, Ψ depends upon position in $\mathcal{B} \times \mathcal{S}$ exclusively through the generalized strain measure $\tilde{\mathbf{C}}$ (Eq. 6.41). Further, it is reasonable to assume that $\tilde{\mathbf{C}}^I$ is the dominant part of the generalized strain measure $\tilde{\mathbf{C}}$, thus, we restrict the dependency of ψ to be on $\tilde{\mathbf{C}}^I$ alone.

For simplicity we define the projection map $\pi_0^*(\tilde{\mathbf{G}}_i)$ (Eq. 6.6) to be the identity, thus, we have $\tilde{\mathbf{G}}_i := \mathbf{G}_i$ and we also assume $\mathbf{G}_i$ to be independent of θ^k in the following.

The variation of the internal potential with respect to $\tilde{\mathbf{C}}^I$ in the Lagrangian form reads as follows

$$\delta\Psi = \int_{\mathcal{B}} \int_{\mathcal{S}} \tilde{\rho}_0 \, \frac{\partial \psi \left(\tilde{\mathbf{C}}^I \left(\theta^k, \zeta^\beta \right) \right)}{\partial \tilde{\mathbf{C}}^I} : \delta \tilde{\mathbf{C}}^I \; dS \, dV \tag{6.53}$$

which is further redrafted to

$$\delta\Psi = \int_{\mathcal{B}} \frac{1}{2} \left\{ \mathbf{S} \left(\theta^k \right) : \delta \mathbf{C} + \boldsymbol{m}^\alpha \left(\theta^k \right) : \delta \mathbf{K}_\alpha \right\} \, dV \tag{6.54}$$

with

$$\mathbf{S} \left(\theta^k \right) = \int_{\mathcal{S}} 2 \, \tilde{\rho}_0 \, \frac{\partial \psi \left(\tilde{\mathbf{C}}^I \left(\theta^k, \zeta^\beta \right) \right)}{\partial \tilde{\mathbf{C}}^I} \, dS \tag{6.55}$$

$$\boldsymbol{m}^\alpha \left(\theta^k \right) = \int_{\mathcal{S}} 2 \, \zeta^\alpha \, \tilde{\rho}_0 \, \frac{\partial \psi \left(\tilde{\mathbf{C}}^I \left(\theta^k, \zeta^\beta \right) \right)}{\partial \tilde{\mathbf{C}}^I} \, dS \tag{6.56}$$

and $\tilde{\mathbf{C}}^I \left(\theta^k, \zeta^\beta \right) = \mathbf{C} \left(\theta^k \right) + \zeta^\alpha \, \mathbf{K}_\alpha \left(\theta^k \right)$. Note that $\mathbf{C}$ and $\mathbf{K}_\alpha$ are constant over $\mathcal{S}$. Consequently, the integration over the micro-continuum $\mathcal{S}$ leads to two different stress measures. These are tensor $\mathbf{S}$ which is energy conjugate to the classical *Cauchy-Green deformation tensor* $\mathbf{C}$ and tensors $\boldsymbol{m}^\alpha$ which are energy conjugate to the first order strain gradients $\mathbf{K}_\alpha$.

For the static case and considering only mechanical processes the *first law of thermodynamics* provides the following variational statement

$$\delta\Psi + \mathcal{W}_{ext} = 0 \, , \tag{6.57}$$

which can be written with Eq. (6.54) and Eq. (6.47) as

$$\int_{\mathcal{B}} \frac{1}{2} \left\{ \mathbf{S} \left(\theta^k \right) : \delta \mathbf{C} + \boldsymbol{m}^\alpha \left(\theta^k \right) : \delta \mathbf{K}_\alpha \right\} \, dV + \mathcal{W}_{ext} = 0 \, . \tag{6.58}$$

Note that the integration over the micro-continuum $\mathcal{S}$ in Eq. (6.48) - Eq. (6.51) as well as in Eq. (6.55) and Eq. (6.56) provides for the implicit incorporation of the micro-structure characterizing internal length scale parameters into Eq. (6.58). That is, the coordinates of the micro-space ζ^α are defined over the intervals $[-\frac{l_\alpha}{2}, \frac{l_\alpha}{2}]$, where l_α are the internal length scale parameters associated with the different dimensions of $\mathcal{S}$.

The governing equations of this functional with respect to macro-space $\mathcal{B}$ are found by integration by parts and applying *Gauss's divergence theorem*

$$\begin{aligned}
&\int_{\mathcal{B}} \Big\{ -\frac{1}{\sqrt{G}}\frac{\partial}{\partial\theta^i}\Big(\sqrt{G}\,\mathbf{F}\,\mathbf{S}\left(\theta^k\right)\mathbf{G}^i\Big)\cdot\delta\mathbf{u} - \frac{1}{\sqrt{G}}\frac{\partial}{\partial\theta^i}\left(\sqrt{G}\,\frac{\partial\mathbf{F}}{\partial\theta^\alpha}\,\boldsymbol{m}^\alpha\left(\theta^k\right)\mathbf{G}^i\right)\cdot\delta\mathbf{u} - \\
&\quad - \mathbf{b}\left(\theta^k\right)\cdot\delta\mathbf{u}\Big\}\,dV + \int_{\partial\mathcal{B}_N}\Big\{\mathbf{F}\,\mathbf{S}\left(\theta^k\right)\mathbf{n}\cdot\delta\mathbf{u} + \frac{\partial\mathbf{F}}{\partial\theta^\alpha}\,\boldsymbol{m}^\alpha\left(\theta^k\right)\mathbf{n}\cdot\delta\mathbf{u} - \\
&\quad - \mathbf{t}^{(\mathbf{n})}\left(\theta^k\right)\cdot\delta\mathbf{u}\Big\}\,dA + \int_{\mathcal{B}}\Big\{-\frac{1}{\sqrt{G}}\frac{\partial}{\partial\theta^i}\Big(\sqrt{G}\,\mathbf{F}\,\boldsymbol{m}^\alpha\left(\theta^k\right)\mathbf{G}^i\Big)\cdot\delta\frac{\partial\mathbf{u}}{\partial\theta^\alpha} - \\
&\quad - \mathbf{l}^\alpha\left(\theta^k\right)\cdot\delta\frac{\partial\mathbf{u}}{\partial\theta^\alpha}\Big\}\,dV + \int_{\partial\mathcal{B}_N}\Big\{\mathbf{F}\,\boldsymbol{m}^\alpha\left(\theta^k\right)\mathbf{n}\cdot\delta\frac{\partial\mathbf{u}}{\partial\theta^\alpha} - \mathbf{q}^{(\mathbf{n})\,\alpha}\left(\theta^k\right)\cdot\delta\frac{\partial\mathbf{u}}{\partial\theta^\alpha}\Big\}\,dA = \\
&= \int_{\mathcal{B}} \Big\{ -\frac{1}{\sqrt{G}}\frac{\partial}{\partial\theta^i}\Big(\sqrt{G}\,\mathbf{F}\,\mathbf{S}\left(\theta^k\right)\mathbf{G}^i\Big)\cdot\delta\mathbf{u} - \frac{1}{\sqrt{G}}\frac{\partial}{\partial\theta^i}\left(\sqrt{G}\,\frac{\partial\mathbf{F}}{\partial\theta^\alpha}\,\boldsymbol{m}^\alpha\left(\theta^k\right)\mathbf{G}^i\right)\cdot\delta\mathbf{u} - \\
&\quad - \mathbf{b}\left(\theta^k\right)\cdot\delta\mathbf{u}\Big\}\,dV + \int_{\partial\mathcal{B}_N}\Big\{\mathbf{F}\,\mathbf{S}\left(\theta^k\right)\mathbf{n}\cdot\delta\mathbf{u} + \frac{\partial\mathbf{F}}{\partial\theta^\alpha}\,\boldsymbol{m}^\alpha\left(\theta^k\right)\mathbf{n}\cdot\delta\mathbf{u} - \\
&\quad - \mathbf{t}^{(\mathbf{n})}\left(\theta^k\right)\cdot\delta\mathbf{u}\Big\}\,dA + \int_{\mathcal{B}}\Big\{\frac{1}{\sqrt{G}}\frac{\partial}{\partial\theta^\alpha}\frac{\partial}{\partial\theta^i}\Big(\sqrt{G}\,\mathbf{F}\,\boldsymbol{m}^\alpha\left(\theta^k\right)\mathbf{G}^i\Big)\cdot\delta\mathbf{u} + \\
&\quad + \frac{\partial}{\partial\theta^\alpha}\mathbf{l}^\alpha\left(\theta^k\right)\cdot\delta\mathbf{u}\Big\}\,dV + \int_{\partial\mathcal{B}_N}\Big\{-\frac{\partial}{\partial\theta^i}\Big(\mathbf{F}\,\boldsymbol{m}^\alpha\left(\theta^k\right)\mathbf{G}^i\Big)\,n_\alpha\cdot\delta\mathbf{u}\Big\}\,dA + \\
&\quad + \int_{\partial\mathcal{B}_N}\Big\{\mathbf{F}\,\boldsymbol{m}^\alpha\left(\theta^k\right)\mathbf{n}\cdot\delta\frac{\partial\mathbf{u}}{\partial\theta^\alpha} - \mathbf{q}^{(\mathbf{n})\,\alpha}\left(\theta^k\right)\cdot\delta\frac{\partial\mathbf{u}}{\partial\theta^\alpha}\Big\}\,dA = 0\,, \qquad (6.59)
\end{aligned}$$

where G is the determinate of the *Riemannian* metric coefficients (Eq. 2.13) and it is assumed $\delta\mathbf{u} = 0$ on $\partial\mathcal{B}_D$. Note the $\mathbf{l}^\alpha$ is set to zero on $\partial\mathcal{B}_N$. Taking into account that $\delta\mathbf{u}$ is a free variation we arrive at the local statement of the governing equations which are the equilibrium equations of the above functional

$$\begin{aligned}
&-\frac{1}{\sqrt{G}}\frac{\partial}{\partial\theta^i}\left(\sqrt{G}\,\mathbf{F}\,\mathbf{S}\left(\theta^k\right)\mathbf{G}^i - \sqrt{G}\,\mathbf{F}\,\frac{\partial}{\partial\theta^\alpha}\,\boldsymbol{m}^\alpha\left(\theta^k\right)\mathbf{G}^i\right) - \mathbf{b}\left(\theta^k\right) + \\
&\quad + \frac{\partial}{\partial\theta^\alpha}\,\mathbf{l}^\alpha\left(\theta^k\right) = \mathbf{0} \quad \text{on } \mathcal{B} \qquad (6.60)
\end{aligned}$$

$$\mathbf{F}\,\mathbf{S}\left(\theta^k\right)\mathbf{n} + \frac{\partial\mathbf{F}}{\partial\theta^\alpha}\,\boldsymbol{m}^\alpha\mathbf{n} - \frac{1}{\sqrt{G}}\frac{\partial}{\partial\theta^i}\left(\sqrt{G}\,\mathbf{F}\,\boldsymbol{m}^\alpha\left(\theta^k\right)\mathbf{G}^i\right)\,n_\alpha = \mathbf{t}^{(\mathbf{n})}\left(\theta^k\right) \quad \text{on } \partial\mathcal{B}_N \qquad (6.61)$$

$$\mathbf{F}\,\boldsymbol{m}^\alpha\left(\theta^k\right)\mathbf{n} = \mathbf{q}^{(\mathbf{n})\,\alpha}\left(\theta^k\right) \quad \text{on } \partial\mathcal{B}_N \qquad (6.62)$$

where $\mathbf{F}$ is the deformation gradient tensor (Eq. 2.5). These field equations are supplemented by essential boundary conditions, the so-called Dirichlet boundary conditions

$$\mathbf{u} = \mathbf{h}_u \quad \text{on } \partial\mathcal{B}_D \qquad (6.63)$$

$$\frac{\partial\mathbf{u}}{\partial\theta^\alpha} = \mathbf{h}^\alpha_\gamma \quad \text{on } \partial\mathcal{B}_D\,. \qquad (6.64)$$

6.3.3 Numerical examples

As the continuity and the consistency of the MLS-approximation functions (Eq. 3.5) have to accommodate the requirements of the used variational formulation, the basis polynomial and the weight function must be chosen according to Eq. (3.8) and Eq. (3.9), respectively. Since the variational formulation (Eq. 6.58) contains second order spatial derivatives of the deformation field, the meshfree approximants (Eq. 3.5) need at least a second order basis polynomial in order to provide the required continuity. The examples in the following are modelled using a second order Pascal-type basis polynomial (Eq. 3.37) together with the quartic spline introduced in App. A as weight function. The numerical integration over the micro-continuum $\mathcal{S}$ is carried out with the help of the *Gauss quadrature*, the order of which is chosen to be second according to the used basis polynomial.

In all examples of this section the external loading is considered to be constant within the micro-space $\mathcal{S}$ so that integration over the micro-continuum results in expressions which are multiples of the micro-continuum volume V_S given by

$$V_S = \int_{\mathcal{S}} dS \,. \tag{6.65}$$

Since the micro-continuum attached to each macroscopic point $\mathbf{X} \in \mathcal{B}$ is assumed to possess the same geometrical configuration and dimensions throughout the entire macro-space $\mathcal{B}$, it is admissible, when evaluating the external virtual work (Eq. 6.47), to perform only the integral over the macro-space $\mathcal{B}$ and to multiply the result afterwards by V_S. Note however, that the size of the micro-continuum can not be chosen arbitrarily small, but is limited by the numerical precision.

The enforcement of the essential boundary conditions is carried out using the penalty method.

The numerical applications in this section can be distinguished in four sets. The first one focuses on size-scale effects in bending of small-scale structures, the second one investigates torsion of very thin beams, the third one is an extensive study of excavation openings in intact rock and the fourth one demonstrates oriented material behaviour for the bending of a thin sheet. The first three sets make use of the hyperelastic *Saint-Venant-Kirchhoff* constitutive model which involves as material parameters *Young's modulus* E and *Poission's ratio* ν, whereas the last one utilizes a non-linear hyperelastic material law.

Polymer micro-cantilever beam

The following example is a set of micro-cantilever beams, the problem definition of which has been already introduced in Sec. 5.7. The variational principle (Eq. 6.58) presented in the previous section allows to choose between one and three dimension for the micro-continuum so that the size of the micro-continuum is controlled by one to three internal length scale parameters l_1, l_2 and l_3. Here we assume $l_1 = l_2 = l_3 = l$. Corresponding to these parameters we have the directors or the basis vectors of the micro-continuum that

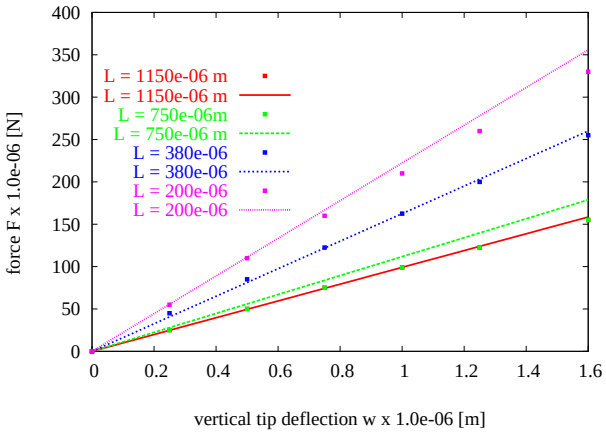

Figure 6.1: *load deflection diagram with* $l_3 = 42\,\mu\,m$ *and* $\nu = 0.3$

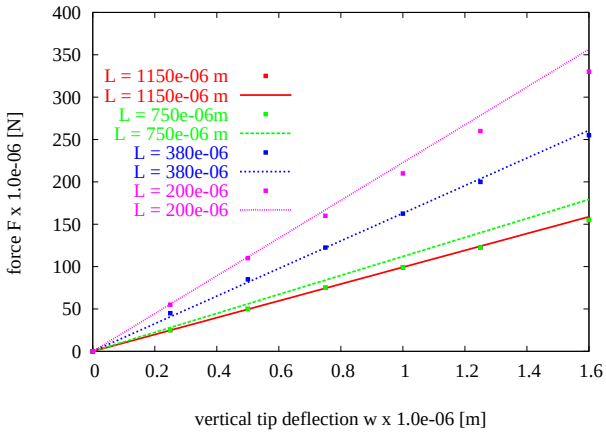

Figure 6.2: *load deflection diagram with* $l_1 = l_2 = l_3 = 42\,\mu\,m$ *and* $\nu = 0.3$

are given by Eq. (6.30). In the following two cases are distinguished. These are firstly, the one-dimensional micro-continuum having only one micro-director expressed by

$$\mathbf{a}_3 = \frac{\partial \mathbf{x}}{\partial \theta^3} \tag{6.66}$$

and secondly, the three-dimensional micro-continuum incorporating three micro-directors defined by

$$\mathbf{a}_\alpha = \frac{\partial \mathbf{x}}{\partial \theta^\alpha} \qquad \text{with}\, \alpha = 1, 2, 3\,. \tag{6.67}$$

The graphs illustrated in Fig. 6.1 - Fig.6.4 combine the load-deflection curves of the tip of four different micro-cantilever beams of lengths $L = 1150\,\mu m$, $750\,\mu m$, $380\,\mu m$ and $200\,\mu m$. The width for all four beams is $b = 235\,\mu m$ and the ratio of length to height $L/h = 10$ is kept constant so that these four beams represent four different scaling levels of one and the same beam. The internal length scale parameter is assumed as $l = 42\,\mu m$. As depicted in the load-deflection graph (Fig. 6.1) the one-dimensional micro-space provides a close match to the experimental results indicated by corresponding dotted curves. Note that the experimental data for the beams with $L = 1150\,\mu m$ and $750\,\mu m$ match each other. There is not a recognizable difference, if the microspace is chosen to be three-dimensional, shown in Fig. 6.2.

Neglecting the transversal contraction does not substantially change the results as illustrated in Fig. 6.3 and Fig. 6.4. This is in opposition to the use of the *Cosserat continuum*-based model (Eq. 5.47) in Sec. 5.7, where the choice of *Poisson's ratio* is of a great significance. This indicates that using the generalized micromorph deformation description (Eq. 6.31) the size-scale effects induced by the higher gradients outweigh those due to the transversal contraction.

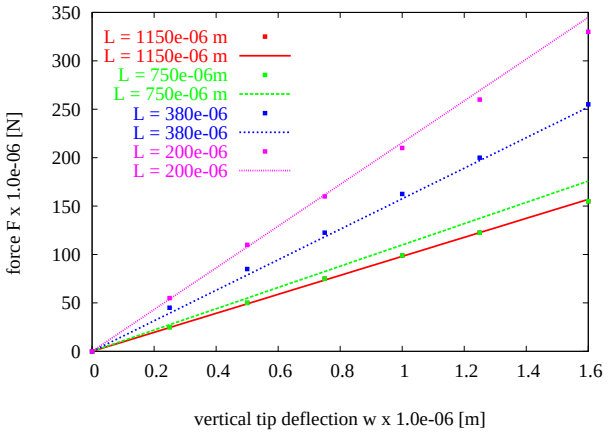

Figure 6.3: *load deflection diagram with* $l_3 = 42\,\mu\,m$ *and* $\nu = 0$

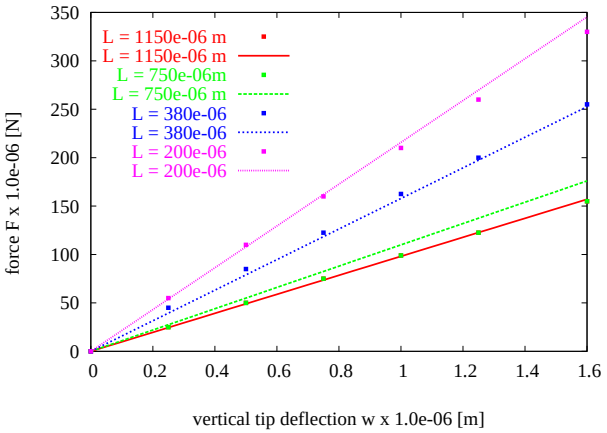

Figure 6.4: *load deflection diagram with* $l_1 = l_2 = l_3 = 42\,\mu\,m$ *and* $\nu = 0$

The modelling of small-scale structures such as the above micro-cantilever beam is discovered to be numerically critical, if the numerical integration over the micro-continuum involves very small numbers which fall below the minimum limit of double precision numbers. The solution leads then to a material behaviour which is significantly too soft. In order to achieve correct results it is necessary to change the geometrical units from meter to milli- or micrometer.

clamped micro-sheet

The second example is a square sheet which is clamped at all its four edges. The problem definition is the same already studied in Sec. 5.7 and can be found there depicted in Fig. 5.1. Due to the symmetry only one quarter of the sheet is modelled by introducing the appropriate symmetry conditions for the displacement field. The material is chosen to be the same as for the micro-cantilever beam, but with a constant *Poisson ratio* $\nu = 0.3$. Again, four different scaling levels have been simulated with $L = 6.0\,mm$, $L = 3.0\,mm$, $L = 1.2\,mm$ and $L = 0.6\,mm$. The ratio of the sheet's length to its height $L/h = 300$ is fixed for all four sheets so that the results are comparable.

Preliminary studies showed that the difference between one-dimensional micro-continuum with micro-director $\mathbf{a}_3$ (Eq. 6.66) and the three-dimensional micro-continuum involving three micro-directors (Eq. 6.67) is negligible. This is clear as the bending of the sheet results in a curvature which is almost exclusively described by vector $\mathbf{a}_3$. Therefore, only the impact of a one-dimensional micro-continuum within the generalized variational formulation (Eq. 6.58) is investigated for scaling effects. The corresponding internal length scale parameter is assumed to be $l = 42\,\mu m$.

The load-deflection curves for the vertical midpoint displacement in Fig. 6.5 and Fig. 6.6 illustrate distinct size-scale effects as the smaller sheets behave increasingly stiffer compared to the classical solution denoted by the red line. In Fig. 6.5 the relation of loading to

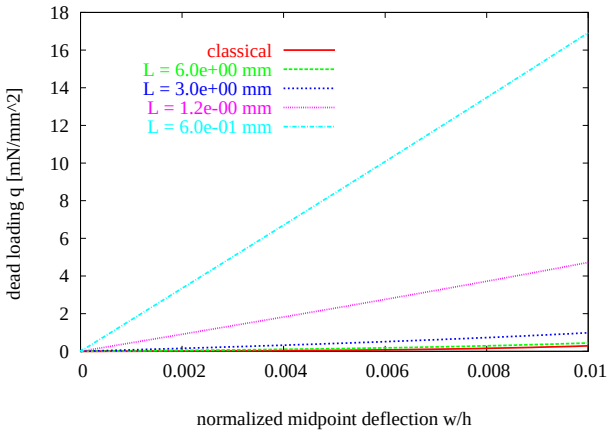

Figure 6.5: *load-deflection diagram*

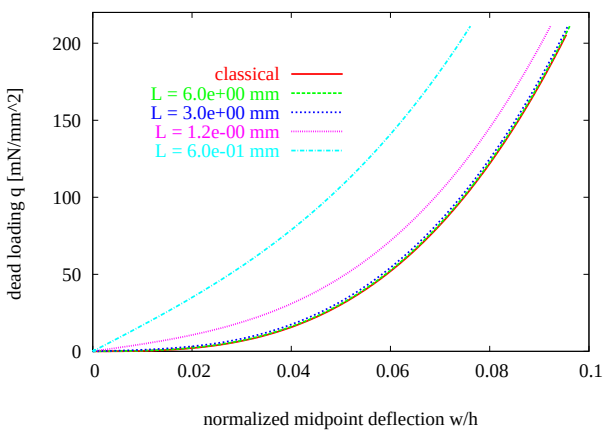

Figure 6.6: *load-deflection diagram*

deflection is for all sheets linear. Fig. 6.6 displays non-linear deformation behaviour for increasing loading. Interestingly, the curves which represent non-classical solutions do not show the same tendency to converge to the classical solution as observed for the modelling of this problem using the *Cosserat continuum* depicted in Fig. 5.7.

Torsion experiments on human bone specimens

This examples has already been presented in Sec. 5.7, where the reader can find further details. The problem is a set of thin beams with a square cross-section with side lengths $a = 5.0\,mm$, $2.0\,mm$, $1.0\,mm$ and $0.5\,mm$ depicted in Fig. 6.7. The ratio of the beam's length to side length $L/a = 100$ is kept constant for all four beams so that the results for twist θ and corresponding torsion moment M_T are comparable. The torsion moment is applied on the tip of the beams. The opposite end of the beams is clamped, that is all displacement degrees of freedom are held over the entire cross-section. The material is assumed to be hyperelastic and modelled by the *Saint-Venant-Kirchhoff* constitutive model which involves as material parameters *Young's modulus* E and *Poission's ratio* ν.

The micro-continuum $\mathcal{S}$ is chosen to be two-dimensional defined by two basis vectors or micro-directors which are given according to Eq. (6.30) by

$$\mathbf{a}_2 = \frac{\partial \mathbf{x}}{\partial \theta^2} \qquad \text{and} \qquad \mathbf{a}_3 = \frac{\partial \mathbf{x}}{\partial \theta^3}\,, \tag{6.68}$$

respectively. Associated with these two micro-directors are the so-called internal length scale parameters l_2 and l_3 which control the the size of the micro-continuum. Here, we assume $l_2 = l_3 = l = 0.5\,mm$ which is twice the value as used in the *Cosserat continuum*-based formulation (Eq. 5.47). The comparison of the simulation results of the micro-cantilever beams provided in this section with the results illustrated in Sec. 5.7 indicate that the internal length scale parameters in Eq. 5.47 and Eq. 6.58 can be related to each other by a factor 2.

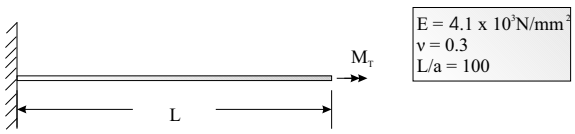

Figure 6.7: *problem configuration*

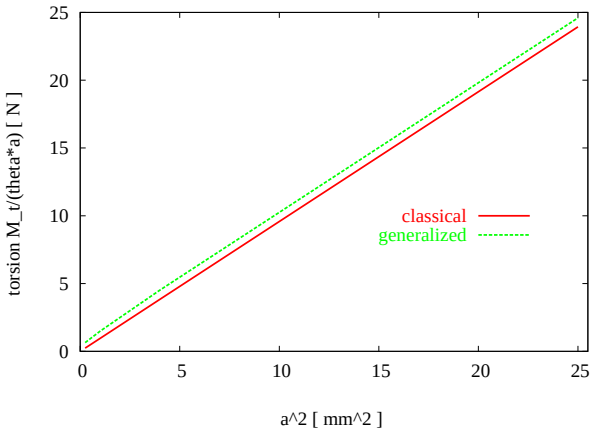

Figure 6.8: *diagram: normalized torsion vs. cross-section size*

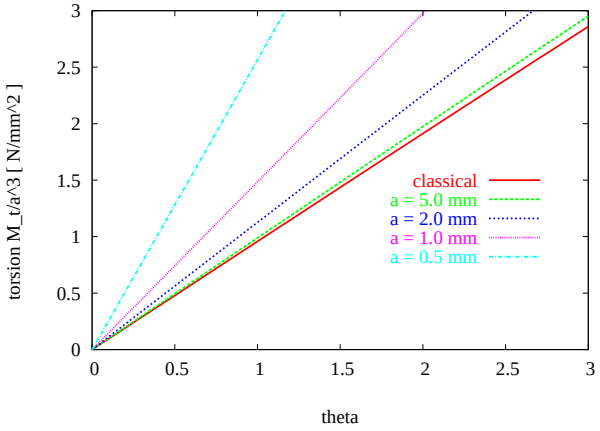

Figure 6.9: *diagram: normalized torsion vs. twist*

If the twist is considered to be small, then the analytical relation of the applied torsion moment to the resulting twist θ is given by

$$M_T = C\,G\,a^4\,\frac{\theta}{L}\,, \tag{6.69}$$

where C is a constant and $L = 100\,a$.

The difference between the classical *Green strain tensor*-based (Eq. 4.8) and the generalized formulation (Eq. 6.58) is clearly recognizable in Fig. 6.8 which illustrates a linear computation. This scaling effect is also more distinctive than shown in Fig. 5.11 which is achieved using a variational principle based on the *Cosserat theory* (Eq. 5.47). The same also applies for non-linear modelling, where the decreasing cross-section leads to increasing rigidity displayed in Fig. 6.9, the magnitude of which is, however, much higher than for the

Cosserat continuum-based model depicted in Fig. 5.12. The classical theory predicts that curves should fall for all side lengths a into one line which is the red curve.

Underground excavations

In this section underground excavations in intact rock conglomerate with two different geometrical configurations are modelled applying a classical *Green strain tensor*-based (Eq. 4.11) and the non-classical generalized formulation (6.58). The micro-continuum is chosen to be two-dimensional and the two micro-directors are given, according to Eq. (6.30), by the spatial derivatives of the macroscopic placement vector $\mathbf{x}$ with respect to the macroscopic, the problem domain defining coordinates θ^1 and θ^2 as follows

$$\mathbf{a}_1 = \frac{\partial \mathbf{x}}{\partial \theta^1}, \quad \mathbf{a}_2 = \frac{\partial \mathbf{x}}{\partial \theta^2}. \tag{6.70}$$

The dimensions of the micro-continuum are controlled by the internal length scale parameters l_1 and l_2. These two parameters could be related to physical properties of the rock mass such as a certain lattice structure which provides that the deformation and the stress can not localize as much or slip between horizontal sediment layers which leads to higher horizontal deformability compared to the vertical. The last feature can be achieved by choosing the internal length scale parameters differently which will be demonstrated at the end of the section. Note that sufficiently small values for these parameters provide the transition from the generalized continuum formulation to the classical one. The constitutive parameters of the used *Saint-Venant-Kirchhoff model* are Young's modulus $E = 20.0\,GPa$ and Poisson's ratio $\nu = 0$. As the meshfree code implemented in this work is three-dimensional the simulated results can be directly related to those achieved using the two-dimensional boundary element method (Hoek and Brown, 1982), if the transversal contraction is neglected. Both excavation configurations are simulated under plane strain conditions assuming the displacement vertical to the plane $u_3 = 0$. Since both problems are rotationally symmetric, only one quarter is modelled applying the appropriate symmetry conditions. The difference between a linear and non-linear simulation is found negligible.

The first example has a circular excavation opening with diameter $d = 4\,m$ depicted in Fig. 6.10. The diameter of the circular simulation domain $D = 10\,m$ is chosen to be large enough so that the pressure loading $p = 54.0189\,MPa$ which is applied on the boundary of the domain does not distort the stress distribution close to the opening. The problem is discretized with 26×31 particles in three horizontal layers.

The classical solutions for the absolute values of the displacement vector, maximum and minimum principal stress and shear stress are illustrated in Fig. 6.14, Fig. 6.16, Fig. 6.18 and Fig. 6.20, whereas the generalized continuum solution for internal length scale parameters $l_1 = l_2 = 4$ in Fig. 6.15, Fig. 6.17, Fig. 6.19 and Fig. 6.21. Note that grid lines in all figures are drawn with a distance of $1.0\,m$ from each other. The illustrations of maximum and minimum principal stress and shear stress are supplemented each by plots along a line between point A and point B depicted in Fig. 6.11 - Fig. 6.13, where the solutions obtained with classical and generalized theory, respectively, are compared with each

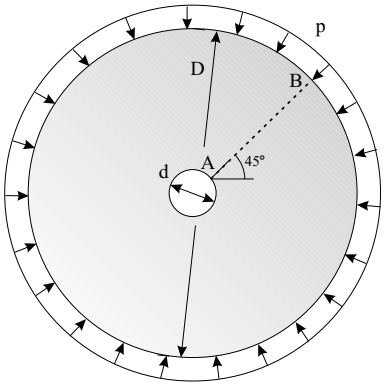

Figure 6.10: *problem definition*

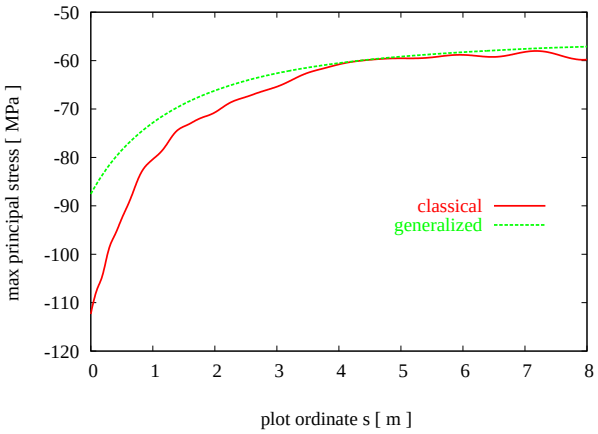

Figure 6.11: *maximum principal stress plotted along a line between point A and point B*

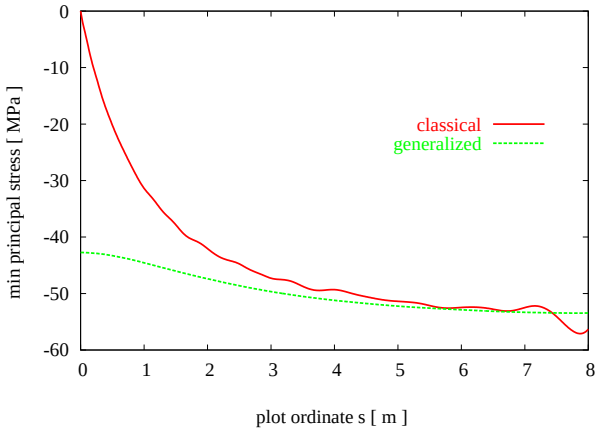

Figure 6.12: *minimum principal stress plotted along a line between point A and point B*

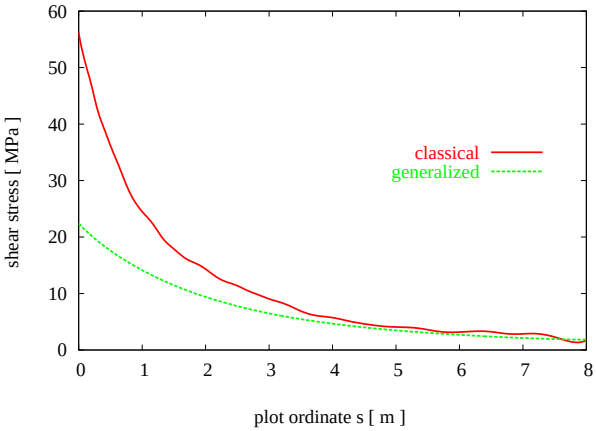

Figure 6.13: *shear stress plotted along a line between point A and point B*

other. The generalized solutions for principal and shear stress distributions are significantly smoother than the classical ones, which is due to a regularizing effect of the second order deformation gradients in the formulation. The maximum principal stress at the excavation opening $\sigma = 115.19\,MPa$ illustrated in Fig. 6.16 agrees well with the boundary element solution (Hoek and Brown, 1982) which predicts $\sigma = 120\,MPa$. The generalized model provides displacement and maximum principal stress values depicted in Fig. 6.17 and Fig. 6.19 respectively, that are significantly lower than those of the classical approach, especially close to the excavation. The magnitude of the in-plane shear stress near to the excavation for the non-classical model illustrated in Fig. 6.21 is less than one half of the Green strain based approach depicted in Fig. 6.20. This clearly indicates that the energy stored in the problem domain splits into first order and second order strain energy parts and correspondingly into

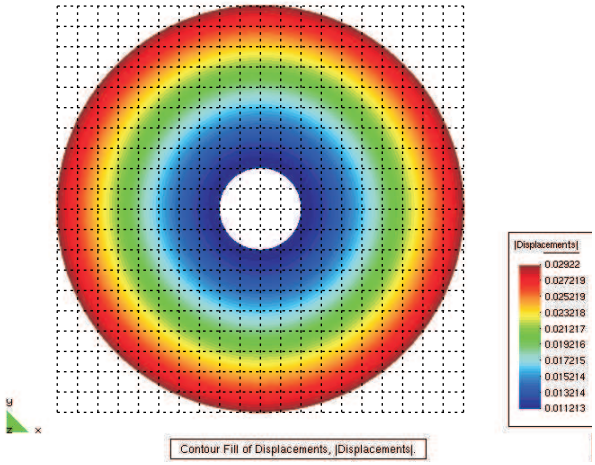

Figure 6.14: *absolute value of displacement vector - classical solution* [m]

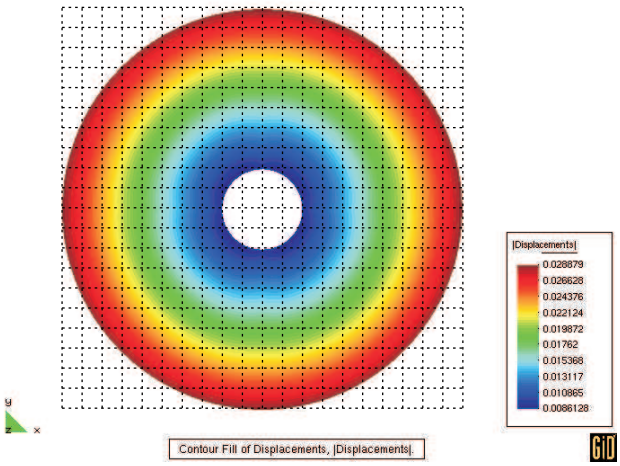

Figure 6.15: *absolute value of displacement vector - generalized solution with a two-dimensional micro-continuum* [m]

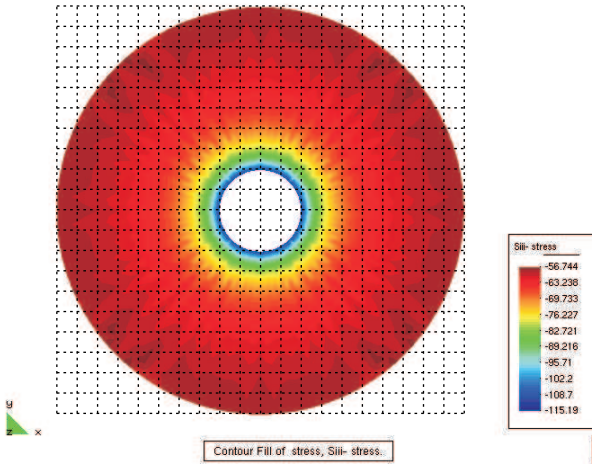

Figure 6.16: *max principal stress - classical solution* [MPa]

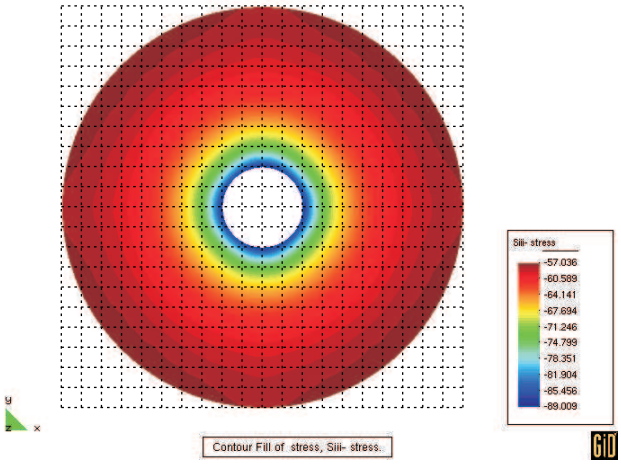

Figure 6.17: *max principal stress - generalized solution with a two-dimensional micro-continuum* [MPa]

first and second order stresses. Obviously this discrepancy depends on the choice of the micro-continuum.

Interestingly, the minimum principal stress along the excavation wall is not zero as it is for the classical approach shown in Fig. 6.12. This is as the first order internal traction equals the second order internal traction, if the external traction is zero, see Eq. (6.61). Furthermore, the classical solution for minimum principal stress depicted in Fig. 6.18 is constant on circles around the excavation opening which is not the case for the generalized solution shown in Fig. 6.19. This difference is the result of the definition of the micro-continuum. The micro-continuum can be seen as a square which is allowed to stretch and rotate relatively to macro-continuum. The current position of this square is defined by

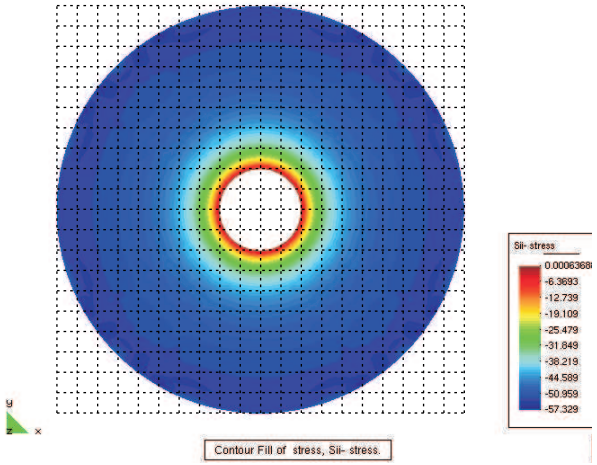

Figure 6.18: *min principal stress - classical solution* [MPa]

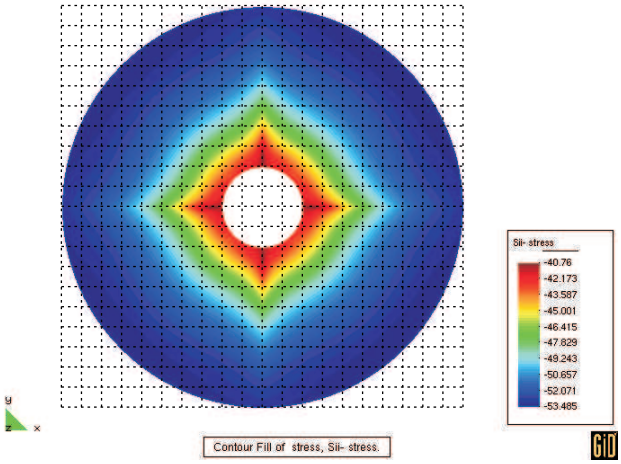

Figure 6.19: *min principal stress - generalized solutions with a two-dimensional micro-continuum* [MPa]

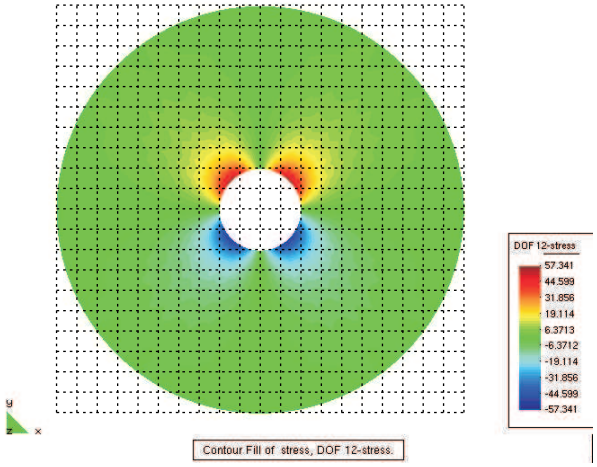

Figure 6.20: *plane shear stress - classical solution* [MPa]

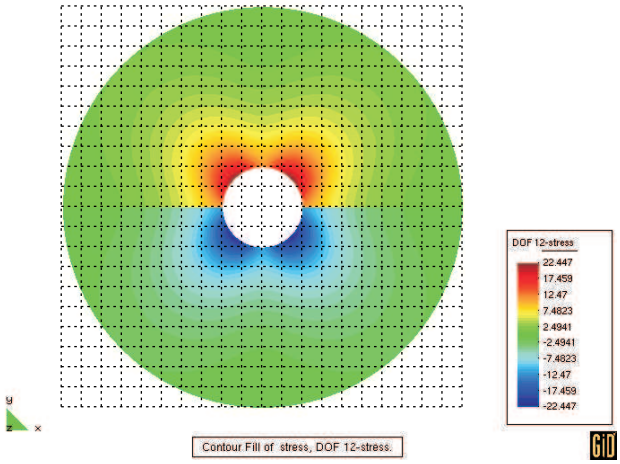

Figure 6.21: *plane shear stress - generalized solution with a two-dimensional micro-continuum* [MPa]

two base vectors which are given by the derivatives of the current macroscopic placement vector with respect to the two in-plane Cartesian coordinate directions Eq. (6.70). As those derivatives are changing on circles around the excavation opening, the micro-continuum's shape is also changing and with it, the second order stress distribution. Reciprocally, the second order stresses affect the first order stresses which are depicted in Fig. 6.17 - Fig. 6.21. However, if the micro-continuum axes would be chosen to be the derivatives of the placement vector with respect to tangential and radial direction, you could expect a non-classical solution for minimum principal stress which would qualitatively match the classical one.

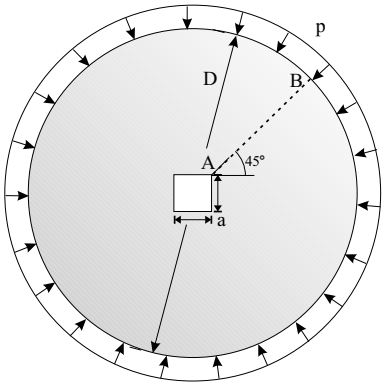

Figure 6.22: *problem definition*

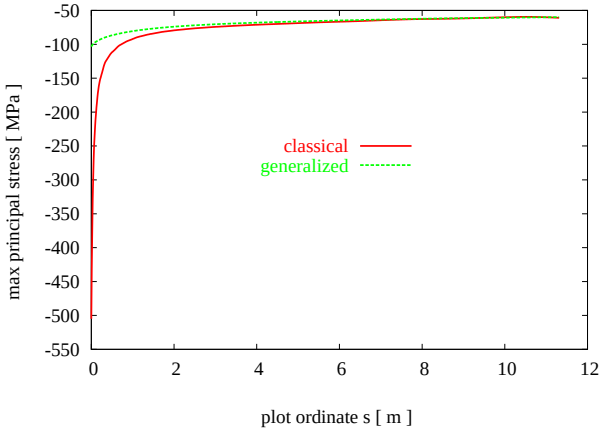

Figure 6.23: *maximum principal stress plotted along a line between point A and point B*

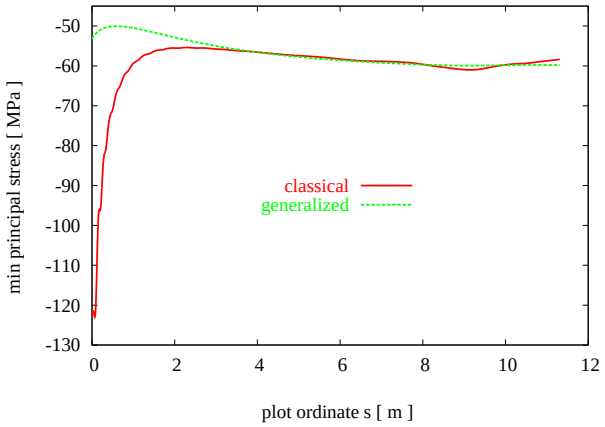

Figure 6.24: *minimum principal stress plotted along a line between point A and point B*

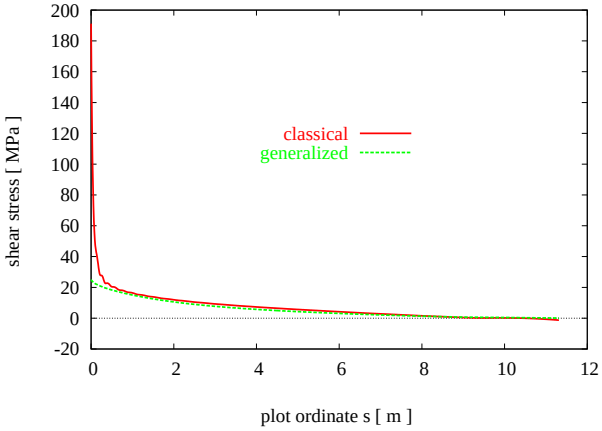

Figure 6.25: *shear stress plotted along a line between point A and point B*

The second examples has a square excavation opening of length and height $a = 4\,m$ depicted in Fig. 6.22. The problem domain is rectangular with $A = 10\,m$ and the outer edges of the domain are subjected to a pressure loading $p = 60\,MPa$. The configuration is discretized with 4473 particles distributed in three horizontal layers.

The classical solutions for the absolute values of the displacement vector, maximum and principal stress, and shear stress are depicted in Fig. 6.26, Fig. 6.28, Fig. 6.30 and Fig. 6.32. The corresponding plots for the generalized continuum solutions assuming the internal length scale parameters as $l_1 = l_2 = 4$ are shown in Fig. 6.27, Fig. 6.29, Fig. 6.31 and Fig. 6.33. Again, the grid lines in all figures are drawn with a distance of $1.0\,m$ from each other. Additionally, plots along a line between point A and point B of maximum and minimum principal stress and shear stress as depicted in Fig. 6.23 - Fig. 6.25 display the comparison of classical and non-classical results. The classical approach provides a peak value of the

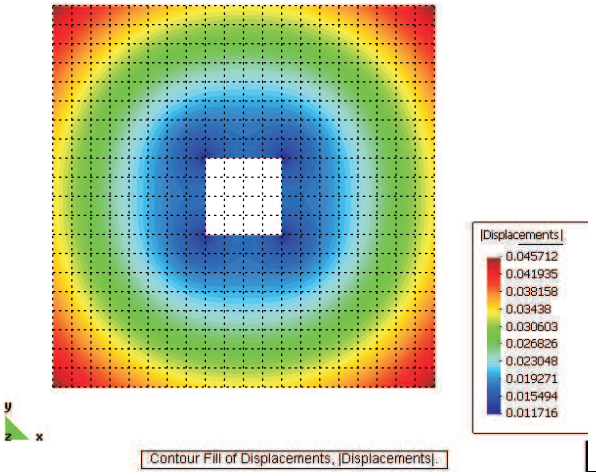

Figure 6.26: *absolute value of displacement vector - classical solution* [m]

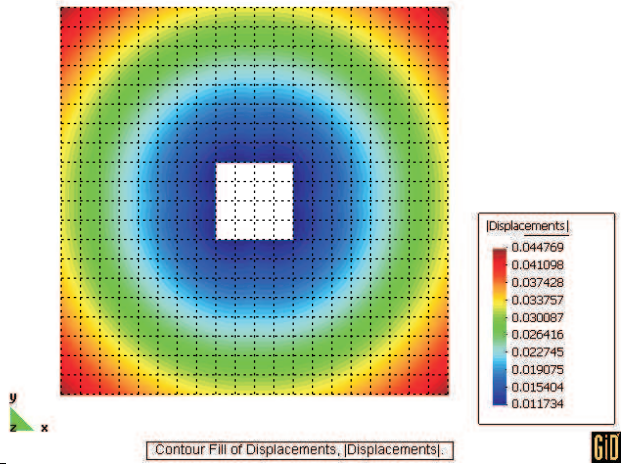

Figure 6.27: *absolute value of displacement vector - generalized solution with a two-dimensional micro-continuum* [m]

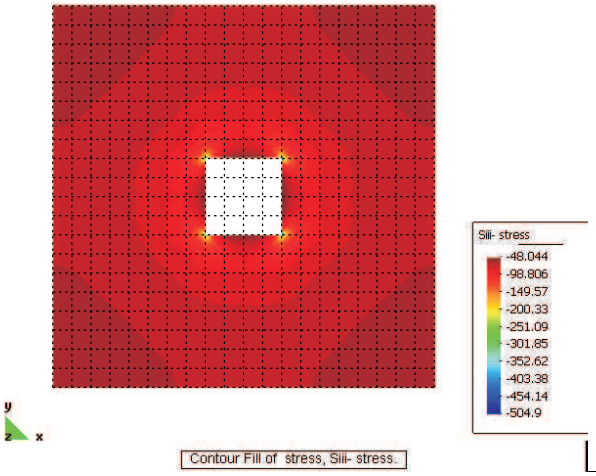

Figure 6.28: *max principal stress - classical solution* [MPa]

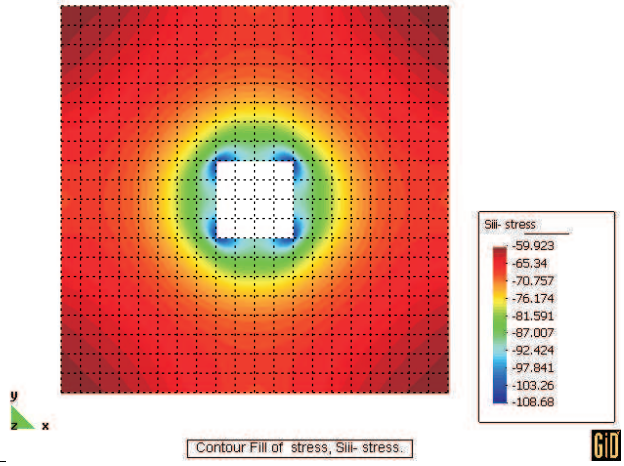

Figure 6.29: *max principal stress - generalized solution with a two-dimensional micro-continuum* [MPa]

maximum principal stress in the corners of the excavation opening $\sigma = 504.4\,MPa$ illustrated in Fig. 6.28 which is only insignificantly lower than predicted in (Hoek and Brown, 1982) to $\sigma = 510\,MPa$. Similar to the application with circular opening, the maximum principal stress distribution is smoother for the non-classical approach.

Using the classical Green strain tensor based formulation the localized stress zone is confined between the first two layers of particles in radial direction. This is also the case for higher discretization levels than 4473 particles. This means that the size of the stress singularity is dependent on the particle distribution. This kind of behavior is known in FEM as mesh dependency. Contrarily, the use of the generalized formulation provides a solution

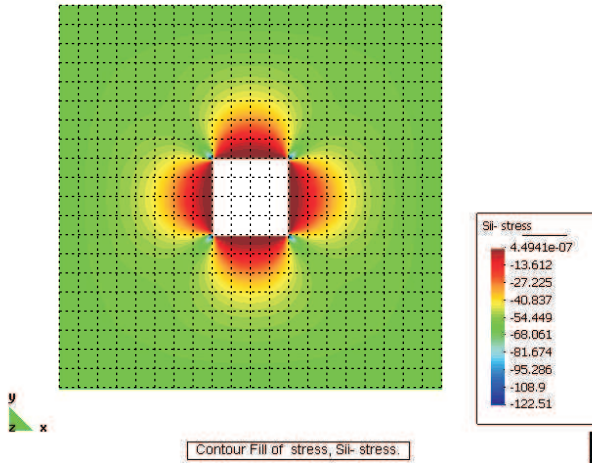

Figure 6.30: *min principal stress - classical solution* [MPa]

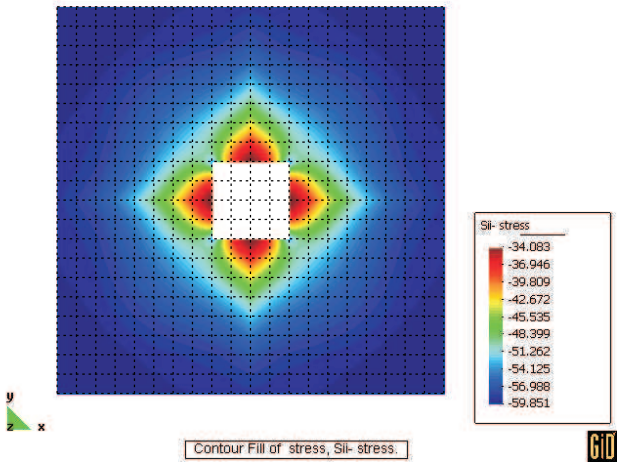

Figure 6.31: *min principal stress - generalized solutions with a two-dimensional micro-continuum* [MPa]

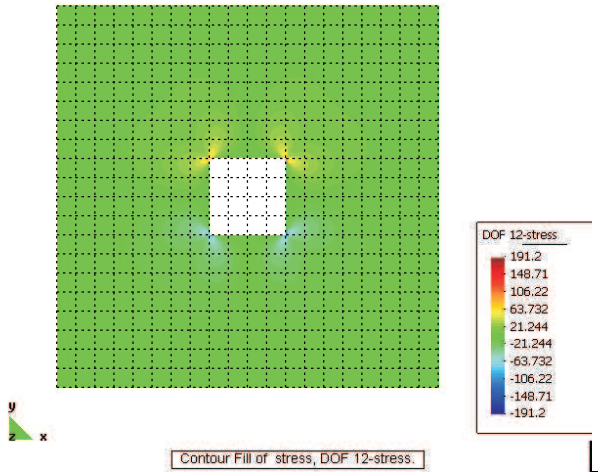

Figure 6.32: *plane shear stress - classical solution* [MPa]

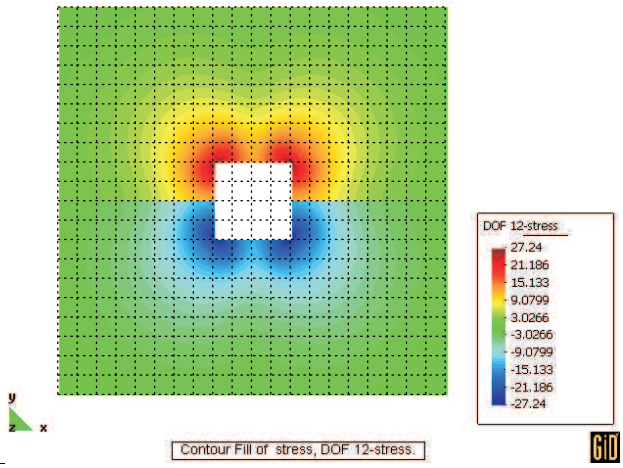

Figure 6.33: *plane shear stress - generalized solution with a two-dimensional micro-continuum* [MPa]

for the stress fields that do not show such a dependency. The non-classical formulation has obviously a regularizing effect preventing the solution for stress and displacement fields to be dependent on the density of the particle distribution.

The modelling using generalized formulation results in significantly lower principle and shear stresses in the corner of the excavation opening than predicted by the classical theory shown in Fig. 6.23 - Fig. 6.25 . The shear stress of the non-classical model is less than one seventh of the Green strain based approach. However, the stresses are kept at significant values around the entire excavation boundary. This finding matches with the displacement along the excavation wall as it maintains at almost constant values. Contrarily, the classical

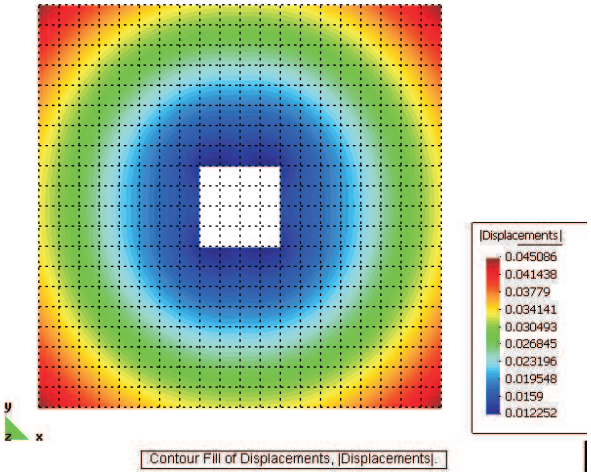

Figure 6.34: *absolute value of displacement vector - generalized solution with a one-dimensional micro-continuum* [m]

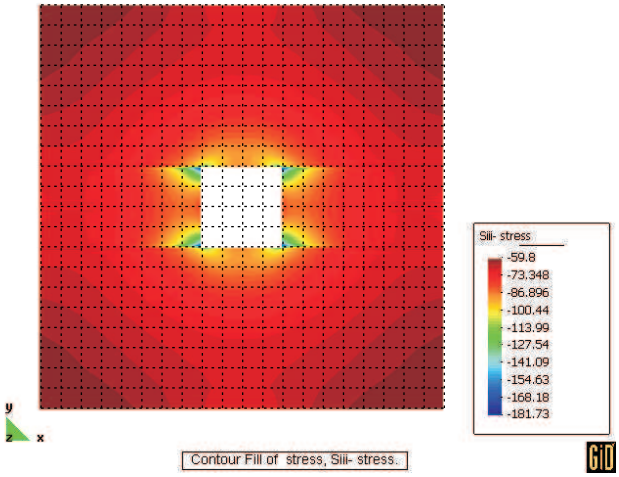

Figure 6.35: *max principal stress - generalized solution with a one-dimensional micro-continuum* [MPa]

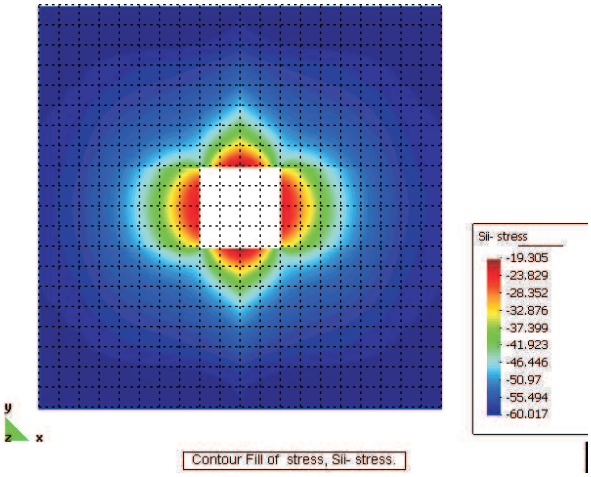

Figure 6.36: *min principal stress - generalized solutions with a one-dimensional micro-continuum* [MPa]

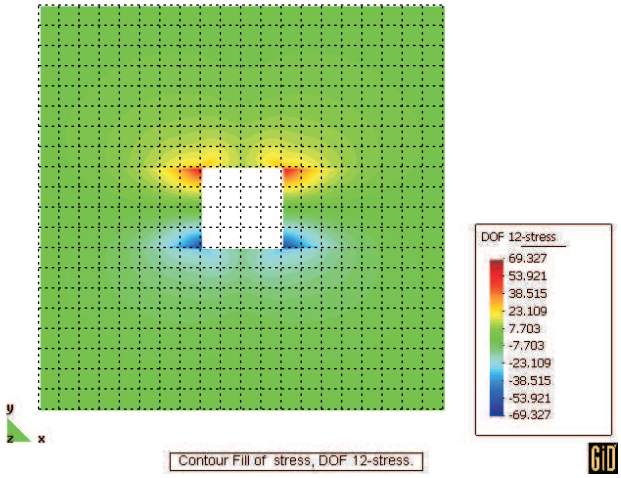

Figure 6.37: *plane shear stress - generalized solution with a one-dimensional micro-continuum* [MPa]

result indicates a clear displacement minimum in the corner and increasing away from it.

The difference in the solution between the classical model and non-classical one is negligible for $l_1 = l_2 = 0.01$ and smaller.

If the internal length scale parameters are set as $l_1 = 4$ and $l_2 < 0.01$, the micro-structural deformation only takes place in horizontal direction. The stresses and the displacement fields depicted in Fig. 6.27 - Fig. 6.33 are obviously different and distorted compared to the results illustrated in Fig. 6.34 - Fig. 6.37.

Summarizing, these examples in rock mechanics demonstrate for the case of plane elastic-

ity that the incorporation of elastic strain gradients can significantly change the distribution of stresses and displacement around excavation constructions. Furthermore, the generalized formulation Eq. (6.58) proves to be independent of the particle distribution density unlike the classical Green strain tensor based formulation.

Simply supported micro-sheet

Finally, orientated material behaviour is modelled making use of the non-linear statistically

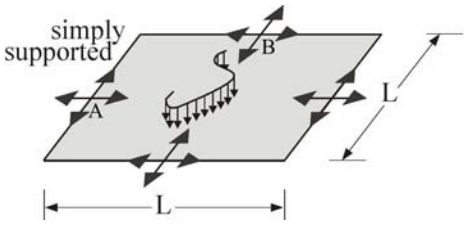

Figure 6.38: *problem definition*

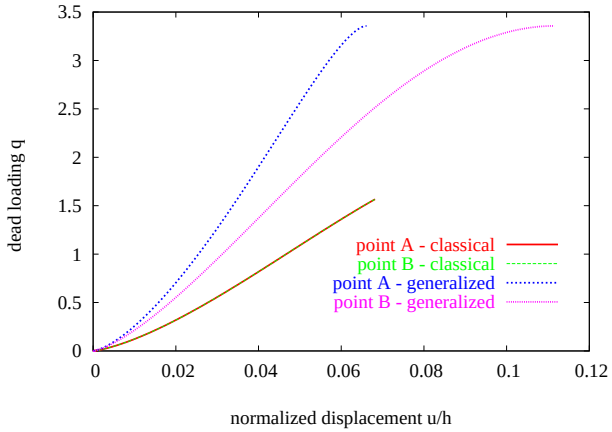

Figure 6.39: *load displacement diagram with* $l_1 = 4.2 \times 10^{-2}$

based constitutive law of hyperelasticity (Arruda and Boyce 1993; Sansour *et al.* 2003a) which which involves as constitutive parameters the shear modulus $C_R = 1.0 \times 10^4$, the bulk modulus $\kappa = 1.0 \times 10^7$ and parameter $N = 8$. This material law was already utilized in the classical *Green strain tensor*-based formulation (Eq. 4.11) in Sec. 4.3. Now however, it is applied to generalized micromorph formulation (Eq. 6.58) to give another demonstration that the incorporation of different constitutive laws is very straightforward. It shows that it is possible to directly use conventional material models in the proposed non-classical variational principle.

The problem illustrated in the following is a square sheet with $L = 0.6$ and $h = 2.0 \times 10^{-3}$ which is simply supported at its outer edges in vertical direction and subjected to a dead loading depicted in Fig. 6.38. Only one quarter of the sheet is modelled with $11 \times 11 \times 3$ particles in longitudinal and thickness direction, respectively, and appropriate symmetry conditions are applied.

The oriented material response is achieved by a specific definition of the micro-continuum $\mathcal{S}$. That is, we consider a one-dimensional micro-continuum, the director or the basis vector of which is given by Eq. (6.30).

Firstly, we define the basis vector to be $\mathbf{g}_1$ and its corresponding internal length scale parameter is determined as $l_1 = 4.2 \times 10^{-2}$. In Fig. 6.39 it is illustrated that the mag-

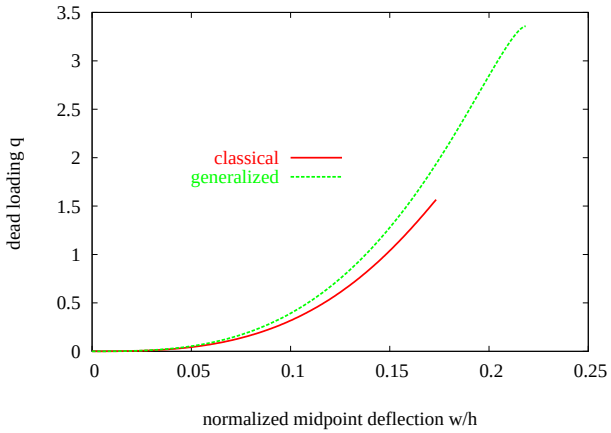

Figure 6.40: *load deflection diagram with* $l_1 = 4.2 \times 10^{-2}$

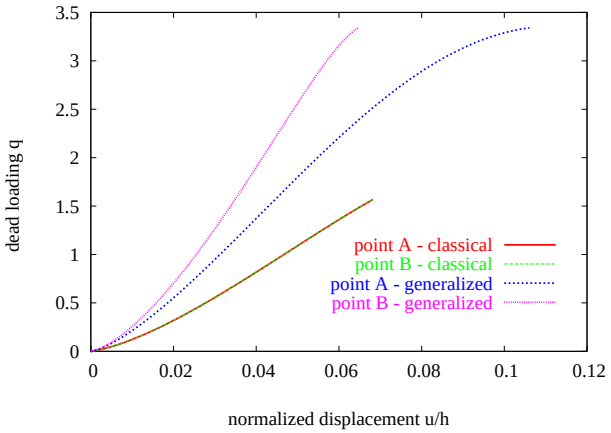

Figure 6.41: *load displacement diagram with* $l_2 = 4.2 \times 10^{-2}$

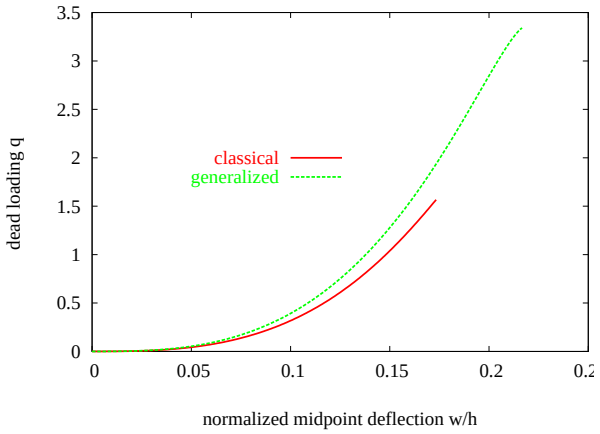

Figure 6.42: *load deflection diagram with* $l_2 = 4.2 \times 10^{-2}$

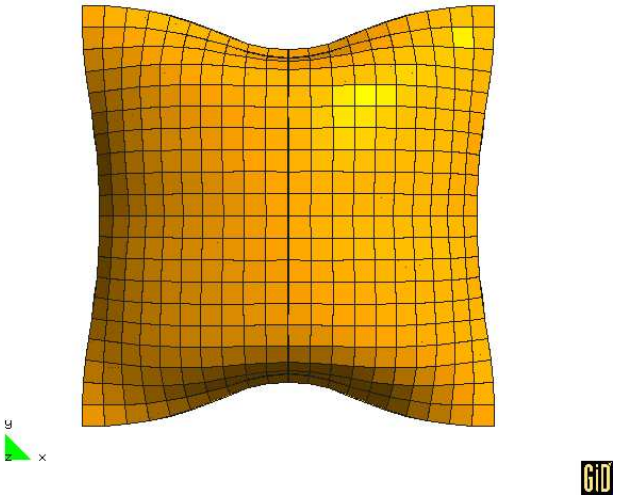

Figure 6.43: *deformed configuration at loading parameter* $q = 3.3$ *with* $l_1 = 4.2 \times 10^{-2}$

nitude of the displacement of point A in x-direction is larger than the one of point B in y-direction which the classical *Green strain tensor*-based model (Eq. 4.11) predicts to be equal as both curves fall into one line. The midpoint deflection displayed in Fig. 6.40 clearly shows that the non-classical solution provides a stiffer material response than exhibited using the *Green strain tensor*-based approach. The final deformed configuration of the sheet using the generalized formulation is illustrated in Fig. 6.43.

Secondly, the basis vector of the micro-continuum is now chosen to be $\mathbf{g}_2$ and the corresponding internal length scale-parameter is $l_2 = 4.2 \times 10^{-2}$. Again, a clear displacement difference of point A in x-direction and of point B in y-direction is recognizable displayed in Fig. 6.41. Now however, the displacement magnitude of point B is larger than the one of point A. The midpoint deflection obtained with the generalized formulation is equal to the previous configuration as illustrated in Fig. 6.42. The final deformed configuration of the

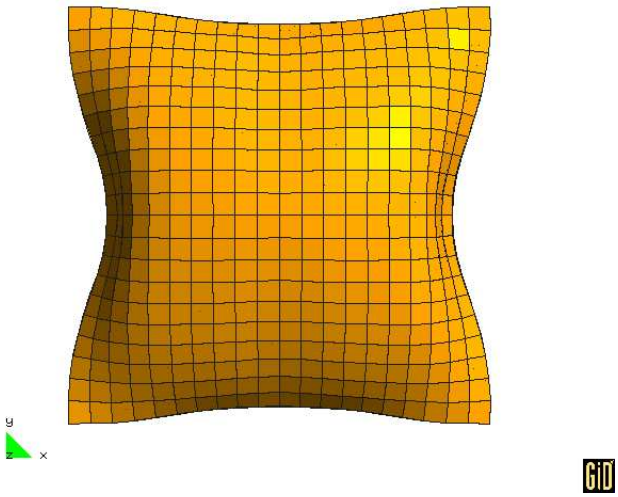

Figure 6.44: *deformed configuration at loading parameter* $q = 3.3$ *with* $l_2 = 4.2 \times 10^{-2}$

sheet modelled with the help of the generalized formulation is depicted in Fig. 6.44.

6.4 Generalized micropolar continuum involving the macro-scopic rotation tensor R

The generalized continuum presented in Sec. 6.2 features a generalized deformation, where the micro-continuum undergoes rigid body rotations as well as shear. The approach holds the benefit that only the displacement field has to be solved for. This is achieved as the deformation of microspace is dependent on the first order derivative of the macro-deformation field. Rigid body rotations of the micro-continuum however, can also be described by making use of a rotation tensor (Sansour 1998b). The directors of the micro-space $\mathbf{a}_\alpha\left(\theta^i, t\right)$ (Eq. 6.14) are in this case associated with a macroscopic rotation tensor $\mathbf{Q}$ which is considered to be independent of the map $\boldsymbol{\varphi}(\mathbf{X}, t)$ (Eq. 2.1) and element of the proper orthogonal transformation group $SO(3)$. Therefore, the micro-directors only carry out micro-rotations and the micro-continuum behaves as a rigid body. The use of the rotation tensor as kinematic field induces three extra rotational degrees of freedom, i.e. the micro-rotations are not hidden within the formulation.

If $\mathbf{Q}$ is substituted for tensor $\mathbf{A}$ into Eq. (6.15), then the generalized deformation (Eq. 6.14) takes the following form

$$\tilde{\mathbf{x}}\left(\theta^i, \zeta^\alpha, t\right) = \mathbf{x}\left(\theta^i, t\right) + \zeta^\alpha\, \mathbf{Q}\left(\theta^i, t\right) \mathbf{I}_\alpha\,, \tag{6.71}$$

which may be called generalized micropolar deformation vector leaning on the definition of Eringen (1999). This provides each material point P with extra three rotational degrees of freedom and the micro-deformation is restricted to rigid body motion. Assuming $\mathbf{I}_\alpha$ to be independent of θ^i and ζ^α the spatial derivatives of the position vector in the current configuration with respect to the macro-coordinates θ^i are given by

$$\tilde{\mathbf{x}}_{,i}\left(\theta^k, \zeta^\alpha, t\right) = \frac{\partial \tilde{\mathbf{x}}}{\partial \theta^i} = \mathbf{x}_{,i}\left(\theta^k, t\right) + \zeta^\alpha\, \mathbf{Q}_{,i}\left(\theta^k, t\right) \mathbf{I}_\alpha\,, \tag{6.72}$$

and with respect to the micro-coordinates ζ^α by

$$\tilde{\mathbf{x}}_{,\alpha}\left(\theta^k, t\right) = \frac{\partial \tilde{\mathbf{x}}}{\partial \zeta^\alpha} = \mathbf{Q}\left(\theta^i, t\right) \mathbf{I}_\alpha\,. \tag{6.73}$$

The generalized deformation gradient which describes the mapping of the tangent space $\mathcal{TG}$ in the reference configuration to a corresponding tangent space in the current configuration $\mathcal{TG}_t$ is with Eq. (6.72) and Eq. (6.73) expressed by

$$\tilde{\mathbf{F}}\left(\theta^i, \zeta^\alpha, t\right) = \left(\mathbf{x}_{,i}\left(\theta^i, t\right) + \zeta^\alpha \mathbf{Q}, i\left(\theta^i, t\right) \mathbf{I}_\alpha\right) \otimes \mathbf{G}^i + \mathbf{Q}\left(\theta^i, t\right) \mathbf{I}_\alpha \otimes \mathbf{I}^\alpha\,. \tag{6.74}$$

6.4.1 Generalized micropolar strain measures

A natural passing to a classical continuum can be achieved, if, in the following, the strain measures are required to be invariant with respect to the group $SO(3)$, very much as in the *Cosserat continuum* Sec. 5.2. This consideration will be elaborated in the next sub-section after deriving the corresponding field equations. Following the above requirement a stretch-type strain measure is chosen on the basis of a general decomposition of $\tilde{\mathbf{F}}$ (Eq. 6.74) as follows

$$\begin{aligned}\tilde{\mathbf{U}}\left(\theta^k,\zeta^\alpha,t\right) &:= \mathbf{R}^T\left(\theta^k,t\right)\tilde{\mathbf{F}}\left(\theta^k,\zeta^\alpha,t\right) = \\ &= \left(\mathbf{R}^T\left(\theta^k,t\right)\mathbf{x}_{,i}\left(\theta^k,t\right)+\zeta^\alpha\mathbf{R}^T\left(\theta^k,t\right)\mathbf{Q}_{,i}\left(\theta^k,t\right)\mathbf{I}_\alpha\right)\otimes\mathbf{G}^i+\mathbf{I}_\alpha\otimes\mathbf{I}^\alpha\,, \quad (6.75)\end{aligned}$$

where $\mathbf{R}$ is given by Eq. (5.1). The first term in Eq. (6.75) is an analogy to the classical stretch tensor and is denoted by

$$\mathbf{U}\left(\theta^k,t\right)=\mathbf{R}^T\left(\theta^k,t\right)\mathbf{x}_{,i}\left(\theta^k,t\right)\otimes\mathbf{G}^i\,, \quad (6.76)$$

whereas the second term is a set of curvature tensors

$$\mathbf{K}_\alpha\left(\theta^k,t\right)=\mathbf{R}^T\left(\theta^k,t\right)\mathbf{Q}_{,i}\left(\theta^k,t\right)\mathbf{I}_\alpha\otimes\mathbf{G}^i\,. \quad (6.77)$$

Since the the third term is simply constant, Eq. (6.75) is re-defined as

$$\tilde{\mathbf{U}}\left(\theta^k,\zeta^\alpha,t\right)=\mathbf{U}\left(\theta^k,t\right)+\zeta^\alpha\,\mathbf{K}_\alpha\left(\theta^k,t\right)\,. \quad (6.78)$$

In the following it is assumed that

$$\mathbf{Q}=\mathbf{R} \quad (6.79)$$

holds and the basis of the micro-space in the reference configuration is to be taken as

$$\mathbf{I}_\alpha:=\mathbf{G}_\alpha=\frac{\partial\mathbf{X}}{\partial\theta^\alpha}\,, \quad (6.80)$$

such that the set of curvature tensor Eq. (6.77) can be re-written as

$$\mathbf{K}_\alpha\left(\theta^k,t\right)=\mathbf{R}^T\left(\theta^k,t\right)\mathbf{R}_{,i}\left(\theta^k,t\right)\mathbf{G}_\alpha\otimes\mathbf{G}^i\,. \quad (6.81)$$

With $\mathbf{R}\in SO(3)$ relations Eq. (5.6) hold and the tensor products $\mathbf{R}^T\mathbf{R}_{,i}$ are therefore skew-symmetric with Eq. (5.7) as axial vector so that Eq. (6.81) can be alternatively expressed as

$$\mathbf{K}_\alpha\left(\theta^k,t\right)=\mathbf{k}_i\left(\theta^k,t\right)\times\mathbf{G}_\alpha\otimes\mathbf{G}^i\,, \quad (6.82)$$

or

$$\mathbf{K}_\alpha\left(\theta^k,t\right)=-\frac{1}{2}\,\boldsymbol{\epsilon}:\mathbf{R}^T\left(\theta^k,t\right)\mathbf{R}_{,i}\left(\theta^k,t\right)\mathbf{G}_\alpha\otimes\mathbf{G}^i\,. \tag{6.83}$$

Due the analogy to a micropolar continuum and the approach presented in this section may be therefore called a generalized micropolar continuum.

In the following sub-chapters we want to confine ourselves to quasi static case.

6.4.2 The generalized variational formulation and its corresponding equilibrium equations

Let us now consider a non-linear boundary value problem in the domain $\mathcal{B}\times\mathcal{S}$ with the boundary $\partial\mathcal{B}\times\mathcal{S}$. The micro-space $\mathcal{S}$ is confined by a corresponding boundary $\partial\mathcal{S}$. Accordingly, we have to distinguished between Dirichlet boundary conditions prescribed on $\partial\mathcal{B}_D\times\mathcal{S}\subset\partial\mathcal{B}\times\mathcal{S}$ denoted by $\tilde{\mathbf{h}}^{(\mathbf{n})}_{\tilde{\mathbf{u}}}$ and such on $\partial\mathcal{B}_D\times\partial\mathcal{S}_D\subset\partial\mathcal{B}\times\partial\mathcal{S}$ denoted by $\tilde{\mathbf{h}}^{(\boldsymbol{\nu})}_{\tilde{\mathbf{u}}}$ where $\mathbf{n}$ defines the normal vector on $\partial\mathcal{B}$ and $\boldsymbol{\nu}$ is the normal vector on $\partial\mathcal{S}$. Correspondingly, Neumann boundary conditions are prescribed on $\partial\mathcal{B}_N\times\mathcal{S}=\partial\mathcal{B}\times\mathcal{S}\setminus\partial\mathcal{B}_D\times\mathcal{S}$ denoted by $\tilde{\mathbf{t}}^{(\mathbf{n})}$ and on $\partial\mathcal{B}_N\times\partial\mathcal{S}_N=\partial\mathcal{B}\times\partial\mathcal{S}\setminus\partial\mathcal{B}_D\times\mathcal{S}_D$ denoted by $\tilde{\mathbf{t}}^{(\boldsymbol{\nu})}$.

The external virtual work $\mathcal{W}_{ext}$ may then be define in the Lagrangian form as follows

$$\mathcal{W}_{ext}\left(\mathbf{u},\boldsymbol{\gamma}\right)=-\int_{\mathcal{B}}\mathbf{b}\left(\theta^k\right)\cdot\delta\mathbf{u}\left(\theta^k\right)\;dV-\int_{\mathcal{B}}\mathbf{l}\left(\theta^k\right)\cdot\mathbf{w}\left(\theta^k\right)\;dV- \tag{6.84}$$

$$-\int_{\partial\mathcal{B}_N}\mathbf{t}^{(\mathbf{n})}\left(\eta^k\right)\cdot\delta\mathbf{u}\left(\theta^k\right)\;dA-\int_{\partial\mathcal{B}_N}\mathbf{q}^{(\mathbf{n})}\left(\eta^k\right)\cdot\mathbf{w}\left(\theta^k\right)\;dA \tag{6.85}$$

where the external body forces

$$\mathbf{b}\left(\theta^k\right)=\int_{\mathcal{S}}\tilde{\rho}_0\,\tilde{\mathbf{b}}\left(\theta^k,\zeta^\alpha\right)\;dS+\int_{\partial\mathcal{S}}\tilde{\mathbf{b}}^{(\boldsymbol{\nu})}\left(\theta^k,\lambda^\alpha\right)\;d\sigma \tag{6.86}$$

and the external body moments

$$\mathbf{l}\left(\theta^k\right)=\int_{\mathcal{S}}\tilde{\rho}_0\,\zeta^\alpha\,\mathbf{R}\mathbf{G}_\alpha\times\tilde{\mathbf{b}}\left(\theta^k,\zeta^\alpha\right)\;dS+\int_{\partial\mathcal{S}}\zeta^\alpha\mathbf{R}\mathbf{G}_\alpha\times\tilde{\mathbf{b}}^{(\boldsymbol{\nu})}\left(\theta^k,\lambda^\alpha\right)\;d\sigma \tag{6.87}$$

are acting on $\mathcal{B}\times\mathcal{S}$ and $\mathcal{B}\times\partial\mathcal{S}$, respectively, whereas the external traction

$$\mathbf{t}^{(\mathbf{n})}\left(\eta^k\right)=\int_{\mathcal{S}}\tilde{\rho}_0\,\tilde{\mathbf{t}}^{(\tilde{n})}\left(\eta^k,\zeta^\alpha\right)\;dS+\int_{\partial\mathcal{S}_N}\tilde{\mathbf{t}}^{(\tilde{\nu})}\left(\eta^k,\lambda^\alpha\right)\;d\sigma\,, \tag{6.88}$$

and the external surface moments

$$\mathbf{q}^{(\mathbf{n})}\left(\eta^k\right) = \int_{\mathcal{S}} \tilde{\rho}_0\, \zeta^\alpha\, \mathbf{R}\mathbf{G}_\alpha \times \tilde{\mathbf{t}}^{(\tilde{n})}\left(\eta^k, \zeta^\alpha\right)\; dS + \int_{\partial\mathcal{S}_N} \zeta^\alpha \mathbf{R}\mathbf{G}_\alpha \times \tilde{\mathbf{t}}^{(\tilde{\nu})}\left(\eta^k, \lambda^\alpha\right)\; d\sigma \tag{6.89}$$

are acting on $\partial\mathcal{B}_N \times \mathcal{S}$, and $\partial\mathcal{B}_N \times \partial\mathcal{S}_N$ respectively. Note that η^k, $k = 1, 2$ is the coordinate chart on $\partial\mathcal{B}$ and λ^α is the coordinate chart on $\partial\mathcal{S}$. Furthermore, dV is a volume element of the macroscopic domain $\mathcal{B}$, whereas dA is a surface element of its corresponding boundary $\partial\mathcal{B}$, and accordingly, dS is a volume element of the microscopic domain $\mathcal{S}$, whereas $d\sigma$ is a surface element of its corresponding boundary $\partial\mathcal{S}$. The density of the micro-space in the reference configuration is denoted by $\tilde{\rho}_0$. In the following, external loading applied on $\mathcal{B}\times\partial\mathcal{S}$ as well as on $\partial\mathcal{B}_N \times \partial\mathcal{S}_N$ is discarded.

Furthermore, we suppose now that the body under consideration $\mathcal{B}\times\mathcal{S}$ is hyperelastic and possesses an elastic potential Ψ represented by the stored strain energy per unit undeformed volume $\tilde{\rho}_0\,\psi$. If the material, in addition, is homogeneous, Ψ depends upon position in $\mathcal{B}\times\mathcal{S}$ exclusively through the first generalized strain measure $\tilde{\mathbf{U}}$.

For simplicity we define the projection map $\pi_0^*(\tilde{\mathbf{G}}_i)$ (Eq. 6.6) to be the identity, thus, we have $\tilde{\mathbf{G}}_i := \mathbf{G}_i$ and we also assume $\mathbf{G}_i$ to independent of θ^k in the following.

The variation of the internal potential with respect to $\tilde{\mathbf{U}}$ in the Lagrangian form reads as follows

$$\delta\Psi = \int_{\mathcal{B}}\int_{\mathcal{S}} \tilde{\rho}_0 \frac{\partial\psi\left(\tilde{\mathbf{U}}\left(\theta^k, \zeta^\alpha\right)\right)}{\partial\tilde{\mathbf{U}}} : \delta\tilde{\mathbf{U}}\; dS\, dV \tag{6.90}$$

and with Eq. 6.76 and Eq. 6.83 it is further redrafted to

$$\delta\Psi = \int_{\mathcal{B}} \left\{ \boldsymbol{n}\left(\theta^k\right) : \delta\mathbf{U} + \boldsymbol{m}\left(\theta^k\right)\mathbf{G}^i \cdot \delta\mathbf{k}_i \right\} dV \tag{6.91}$$

where

$$\boldsymbol{n}\left(\theta^k\right) = \int_{\mathcal{S}} \tilde{\rho}_0 \frac{\partial\psi\left(\tilde{\mathbf{U}}\left(\theta^k, \zeta^\alpha\right)\right)}{\partial\tilde{\mathbf{U}}}\; dS \tag{6.92}$$

$$\boldsymbol{m}\left(\theta^k\right) = \int_{\mathcal{S}} \tilde{\rho}_0\, \zeta^\alpha\, \mathbf{G}_\alpha \times \frac{\partial\psi\left(\tilde{\mathbf{U}}\left(\theta^k, \zeta^\alpha\right)\right)}{\partial\tilde{\mathbf{U}}}\mathbf{G}^i\; dS\,. \tag{6.93}$$

Note that $\boldsymbol{n}$ is an analogy to the so-called *Biot-Lurje* stress tensor which is energy conjugate to the classical stretch tensor $\mathbf{U}$ and with the *first Piola-Kirchhoff stress tensor* $\mathbf{P}$ Eq. (2.26) defined as

$$\boldsymbol{n}\left(\theta^k\right) = \mathbf{R}^T\mathbf{P}\,. \tag{6.94}$$

$\boldsymbol{m}$ may be interpreted as a couple stress tensor. For details on the variations $\delta\mathbf{U}$ and $\delta\mathbf{k}_i$ the reader is referred to Sec. 5.3.

In the static case and by considering only mechanical processes the *first law of thermodynamics* provides the following variational statement

$$\delta\Psi + \mathcal{W}_{ext} = 0\,, \tag{6.95}$$

which can be written with Eq. (6.91) and Eq. (6.85) as

$$\int_{\mathcal{B}} \left\{ \boldsymbol{n}\left(\theta^k\right) : \delta\mathbf{U} + \boldsymbol{m}\left(\theta^k\right)\mathbf{G}^i \cdot \delta\mathbf{k}_i \right\} dV + \mathcal{W}_{ext} = 0\,. \tag{6.96}$$

The governing equations of this functional can be derived, if we redraft Eq. (6.96) as follows

$$\begin{aligned} -\int_{\mathcal{B}} \Big\{ & \frac{1}{\sqrt{G}} \left(\sqrt{G}\,\mathbf{R}\boldsymbol{n}\left(\theta^k\right)\mathbf{G}^i\right)_{,i} \cdot \delta\mathbf{u} + \mathbf{x}_{,i} \times \mathbf{R}\boldsymbol{n}\left(\theta^k\right) \cdot \mathbf{w} + \\ & + \frac{1}{\sqrt{G}} \left(\sqrt{G}\,\mathbf{R}\boldsymbol{m}\left(\theta^k\right)\mathbf{G}^i\right)_{,i} \cdot \mathbf{w} \Big\}\, dV + \int_{\partial\mathcal{B}} \Big\{ \mathbf{R}\boldsymbol{n}\left(\eta^k\right)\mathbf{n} \cdot \delta\mathbf{u} + \mathbf{R}\boldsymbol{m}\left(\eta^k\right)\mathbf{n} \cdot \mathbf{w} - \\ & - \mathbf{t}^{(\mathbf{n})}\left(\eta^k\right) \cdot \delta\mathbf{u} - \mathbf{q}^{(\mathbf{n})}\left(\eta^k\right) \cdot \mathbf{w} \Big\}\, dA - \int_{\mathcal{B}} \Big\{ \mathbf{b}\left(\theta^k\right) \cdot \delta\mathbf{u} + \mathbf{l}\left(\theta^k\right) \cdot \mathbf{w} \Big\}\, dV = 0\,, \end{aligned} \tag{6.97}$$

where we made use of *Gauss's divergence theorem*. G is the determinate of the *Riemannian* metric coefficients (Eq. 2.13). Furthermore, the basis vectors $\mathbf{G}_i$ are considered to be independent of θ^k here and throughout this section.

Taking into account that $\delta\mathbf{u}$ and $\mathbf{w}$ are free variations, we arrive at the local statement of the governing equations which are the equilibrium equations of the above functional

$$-\left(\mathbf{R}\boldsymbol{n}\left(\theta^k\right)\mathbf{G}^i\right)_{,i} - \mathbf{b}\left(\theta^k\right) = \mathbf{0}\,, \qquad \text{in} \quad \mathcal{B} \tag{6.98}$$

$$-\mathbf{x}_{,i} \times \mathbf{R}\boldsymbol{n}\left(\theta^k\right) - \left(\mathbf{R}\boldsymbol{m}\left(\theta^k\right)\mathbf{G}^i\right)_{,i} - \mathbf{l}\left(\theta^k\right) = \mathbf{0}\,, \qquad \text{in} \quad \mathcal{B}\,. \tag{6.99}$$

The corresponding natural boundary conditions are

$$\mathbf{R}\boldsymbol{n}\left(\eta^k\right)\mathbf{n} = \mathbf{t}^{(\mathbf{n})}\left(\theta^k\right)\,, \qquad \text{on} \quad \mathcal{B}_N \tag{6.100}$$

$$\mathbf{R}\boldsymbol{m}\left(\eta^k\right)\mathbf{n} = \mathbf{q}^{(\mathbf{n})}\left(\theta^k\right)\,, \qquad \text{on} \quad \mathcal{B}_N\,. \tag{6.101}$$

These above field equations are supplemented by essential boundary conditions, the so-called Dirichlet boundary conditions

$$\mathbf{u} = \mathbf{h}_u\,, \quad \text{on } \partial\mathcal{B}_D \tag{6.102}$$

$$\boldsymbol{\gamma} = \mathbf{h}_{\boldsymbol{\gamma}}\,, \quad \text{on } \partial\mathcal{B}_D\,. \tag{6.103}$$

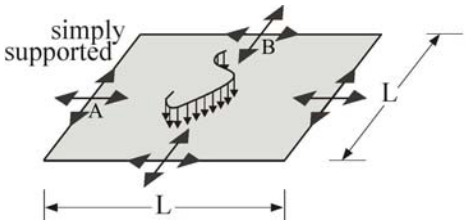

Figure 6.45: *problem definition*

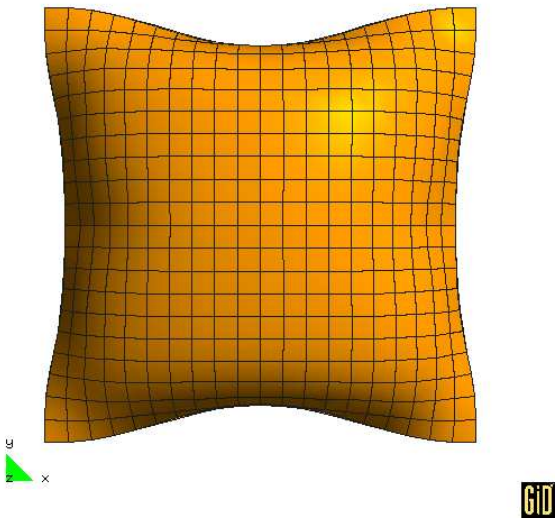

Figure 6.46: *deformed configuration at loading parameter* $83.41\,mN/mm^2$ *with* $l_1 = 21\,\mu m$

Finally, we take up the statement made in Sec. 6.4.1 that a natural passing to a classical continuum can be achieved, if the generalized strain measures are required to be invariant with respect to the group $SO(3)$. This can be readily shown, if we consider the micro-continuum to be infinitely small so that the couple stress $\boldsymbol{m}$ (Eq. 6.93) vanishes. Hence, only the well-known classical equilibrium equations (Eq. 6.98) and (Eq. 6.100) remain.

6.4.3 Numerical examples

We recall that the continuity and the consistency provided by the MLS-approximation functions (Eq. 3.5) has to meet the requirements of the used variational formulation so that the basis polynomial and weight function must be chosen according to Eq. (3.8) and Eq. (3.9), respectively. The formulation (Eq. 6.96) presented in the previous section contains first order spatial derivatives so that the meshfree approximants Eq. (3.5) only need a first order basis polynomial in order to provide the required continuity. Nonetheless, a second order Pascal-type basis polynomial (Eq. 3.37) is chosen to model the examples in the following. As weight function the quartic spline introduced in App. A is utilized. The numerical integration over the micro-continuum $\mathcal{S}$ is carried out with the help of the *Gauss quadrature*, the order of which is chosen to be second according to the used basis polynomial.

The problem studied in the following is a square sheet which is considered in four different scaling levels with lengths $L = 6.0\,mm$, $L = 3.0\,mm$, $L = 1.2\,mm$ and $L = 0.6\,mm$. The ratio of the plate's length to its height $L/h = 300$ is kept constant for all four sheets so that the results are comparable. The sheets are simply supported at their outer edges in vertical direction and subjected to a dead loading depicted in Fig. 6.45. Only one quarter of the sheet is modelled with $11 \times 11 \times 3$ particles in longitudinal and thickness direction,

Figure 6.47: *deformed configuration at loading parameter* $83.41\,mN/mm^2$ *with* $l_2 = 21\,\mu\,m$

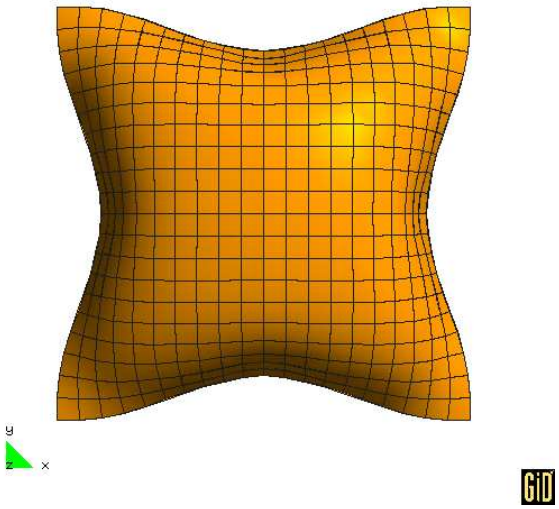

Figure 6.48: *deformed configuration at loading parameter* $231.83\,mN/mm^2$ *with* $l_1 = 21\,\mu\,m$ *and* $l_2 = 21\,\mu\,m$

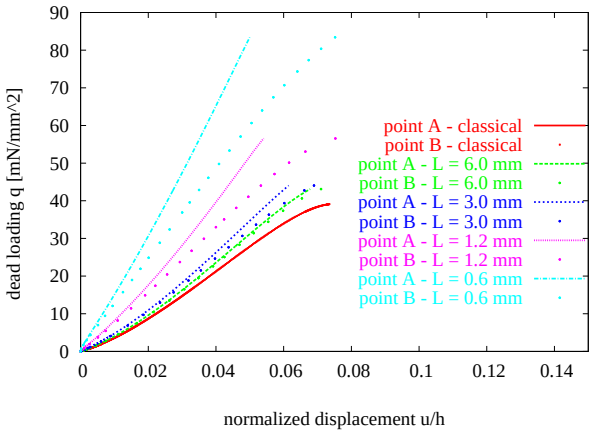

Figure 6.49: *load displacement diagram with* $l_1 = 21\,\mu\,m$

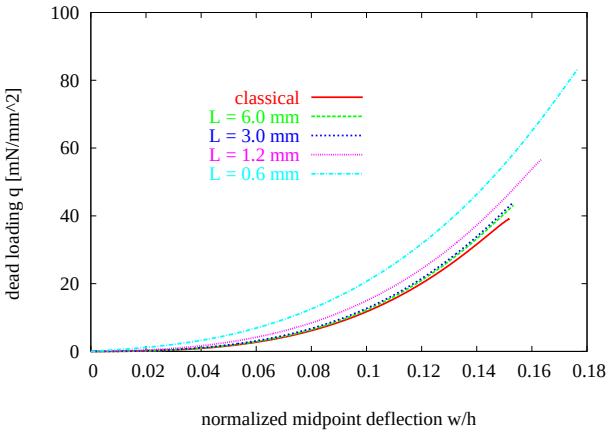

Figure 6.50: *load deflection diagram with* $l_1 = 21\,\mu\,m$

respectively, making use of the appropriate symmetry conditions.

The external loading is assumed to be constant within the micro-space $\mathcal{S}$ so that integration over the micro-continuum results in expressions which are multiples of the micro-continuum volume V_S (Eq. 6.65). Therefore, similar to Sec. 6.3.3, the evaluation of the external virtual work (Eq. 6.85) considers only the integral over the macro-space $\mathcal{B}$ and the resulting external force vector is multiplied by V_S afterwards. The enforcement of the essential boundary conditions is achieved using the penalty method.

The material behaviour is assumed to be hyperelastic and the *Saint-Venant-Kirchhoff* constitutive model is utilized which involves as material parameters *Young's modulus* $E = 1.55\,GPa$ and *Poission's ratio* $\nu = 0.3$.

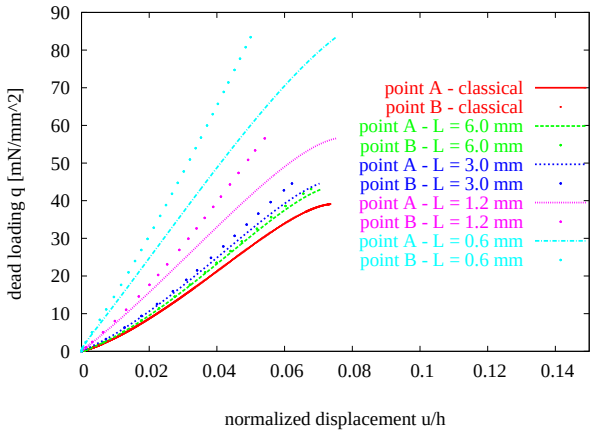

Figure 6.51: *load displacement diagram with* $l_2 = 21\,\mu m$

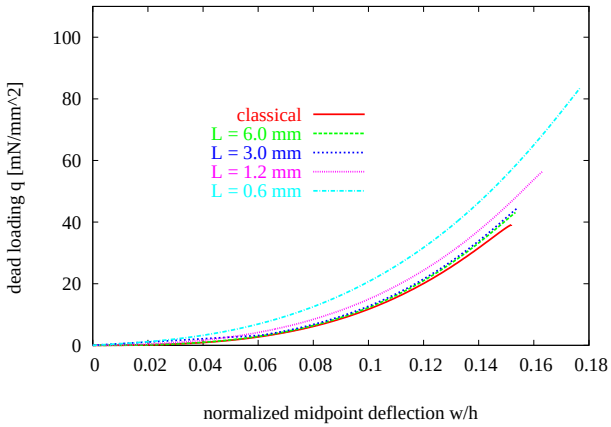

Figure 6.52: *load deflection diagram with* $l_2 = 21\,\mu m$

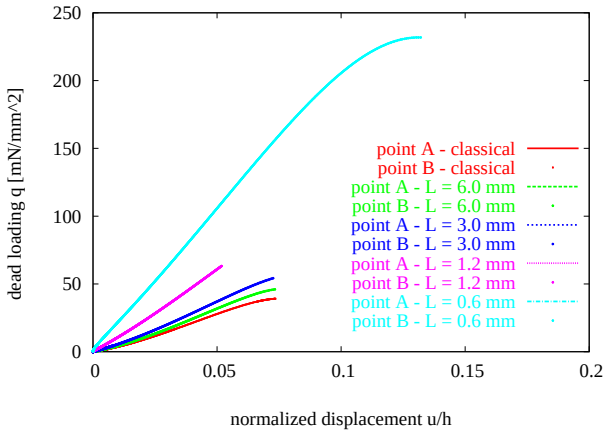

Figure 6.53: *load displacement diagram with* $l_1 = 21\,\mu m$ *and* $l_2 = 21\,\mu m$

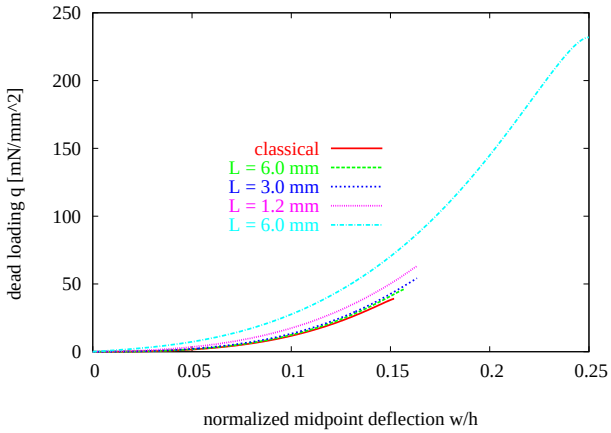

Figure 6.54: *load deflection diagram with* $l_1 = 21\,\mu m$ *and* $l_2 = 21\,\mu m$

Making use of the generalized micropolar variational formulation (Eq. 6.96) it is now the aim to illustrate oriented deformation behaviour due to a particular specification of the micro-continuum $\mathcal{S}$. That is, the micro-continuum is first assumed to be one-dimensional and its basis vector in the reference configuration is taken to be $\mathbf{G}_1$ according to Eq. (6.80). The corresponding internal length scale parameter is determined as $l_1 = 21\,\mu m$. The final deformed configuration of the smallest sheet with $L = 0.6\,mm$ displayed in Fig. 6.46 clearly shows that the magnitude of the displacement of point A in x-direction is larger than the one of point B in y-direction which the classical *Green strain tensor*-based model (Eq. 4.11) predicts for all scaling levels to be equal, illustrated in Fig. 6.49. It can also be recognized that the difference in displacement of point A in x-direction denoted by the continuous graphs and of point B in y-direction denoted by the dotted line is increasing for the smaller sheets. The curves of each scaling level are differentiated by separate colors, where the red graphs represent the classical solutions. In the same way as the displacement discrepancy

of points A and B is increasing, the midpoint deflection is decreasing for the smaller scaling levels depicted in Fig. 6.50.

Subsequently, the basis vector of $\mathcal{S}$ in the reference configuration is now alternated to $\mathbf{G}_2$ and the corresponding internal length scale-parameter is chosen to be $l_2 = 21\,\mu m$. Again, the final deformed configuration of the smallest sheet with $L = 0.6\,mm$ illustrated in Fig. 6.47 indicates a distinct difference in the displacement of point A in x-direction and of point B in y-direction. Now however, the displacement magnitude of point B is larger than the one of point A shown also in Fig. 6.51. As expected the decreasing midpoint deflection depicted in Fig. 6.52 indicates an increasing rigidity for the smaller sheets in vertical direction, but the non-classical results are equal to the previous configuration.

Finally, we consider a two-dimensional micro-continuum with the basis vectors $\mathbf{G}_1$ and $\mathbf{G}_2$, and the corresponding internal length scale parameters are given by $l_1 = 21\,\mu m$ and $l_2 = 21\,\mu m$. Now, we find that there is no displacement difference of point A and point B as illustrated in Fig. 6.48 and Fig. 6.53, as the curves for both points fall into one line. The stiffness increase with respect to the vertical midpoint deflection exhibited by the problem for smaller scaling levels though, is clearly larger than for the two previous configurations of the micro-continuum, shown in Fig. 6.54.

Chapter 7

Experiments in mixed and modified formulations with higher order derivatives

7.1 Overview

Following the success of the generalized variational principle (Eq. 6.58) presented in the previous chapter it remains to investigate, whether the continuity and consistency provided by the MLS-based meshfree approximation functions can also be utilized to deal with classical variational principles which involve higher order derivatives. In this sense one could consider to model not only the weak form of the problem which usually involves first order derivatives in solid mechanics, but also its strong form. Furthermore, the order of the used numerical integration scheme which, in this work, is the Gauss quadrature could be lowered corresponding to the derivation order incorporated in the formulation.

Alternatively, a particle integration scheme could be considered which normally leads, in case of the weak form, to under-integration and numerical instability caused by vanishing first order shape function derivatives at the particles. Since the second order derivatives of the MLS-based meshfree shape functions do not vanish at the particles, we might expect this to compensate for the first order derivatives and thus, stabilize the formulation. The use of a particle integration would be very advantageous, as no background grid for the integration would be needed anymore and, consequently, the meshfree method could be truly called *meshfree*. Moreover, the computational costs for the integration would be less, because fewer integration points have to be evaluated in comparison to the Gauss quadrature.

The modified variational principles to be developed in Sec. 7.2, Sec. 7.3, Sec. 7.4 and Sec. 7.5 aim to enrich classical formulations by means of incorporating higher order derivatives of the solution function and to study the suitability of MLS-based meshfree methods with respect to the higher order derivatives.

7.2 Mixed modified variational principle based on the *Hellinger-Reissner* functional with independent displacement and stress field

7.2.1 First version

Let us consider a non-linear boundary value problem on domain $\mathcal{B}$ with boundary $\partial\mathcal{B}$. Displacement boundary conditions are prescribed on $\partial\mathcal{B}_D \subset \partial\mathcal{B}$ and traction boundary conditions are prescribed on $\partial\mathcal{B}_N = \partial\mathcal{B} \backslash \partial\mathcal{B}_D$. Let us assume hyperelastic material behaviour and $\rho_0\psi(\mathbf{E})$ define the stored energy per unit volume which is a functional of the *Green strain tensor* $\mathbf{E}$. Furthermore, let $\tilde{\psi}(\mathbf{S})$ define the complementary function of $\psi(\mathbf{E})$, where $\mathbf{S}$ denotes the *second Piola-Kirchhoff stress tensor*. Due to the convexity of $\psi(\mathbf{E})$ the following expression holds

$$\rho_0\psi(\mathbf{E}) + \rho_0\tilde{\psi}(\mathbf{S}) = \mathbf{S} : \mathbf{E}\,, \tag{7.1}$$

which is the so-called *Legendre transformation*. Reformulating (Eq. 7.1) as follows

$$\mathcal{F} = \mathbf{S} : \mathbf{E} - \rho_0\tilde{\psi}(\mathbf{S})\,, \tag{7.2}$$

we arrive at an expression which is a functional of the *Green strain tensor* $\mathbf{E}$ and the *second Piola-Kirchhoff stress tensor* $\mathbf{S}$. Assuming that the body under consideration $\mathcal{B}$ possesses an elastic potential we cast $\mathcal{F}$ in integral form and write first the internal potential in the Lagrangian form as follows

$$\Psi = \int_{\mathcal{B}} \left\{ \mathbf{S} : \mathbf{E} - \rho_0\tilde{\psi}(\mathbf{S}) \right\} dV\,, \tag{7.3}$$

and finally the so-called *Hellinger-Reissner functional* is given by

$$\Pi = \int_{\mathcal{B}} \left\{ \mathbf{S} : \mathbf{E} - \rho_0\tilde{\psi}(\mathbf{S}) \right\} dV + \mathcal{W}_{ext}(\mathbf{u}) = \text{stationary}\,. \tag{7.4}$$

$\mathcal{W}_{ext}$ denotes the external potential which is expressed by

$$\mathcal{W}_{ext}(\mathbf{u}) = -\int_{\mathcal{B}} \mathbf{b} \cdot \mathbf{u}\; dV - \int_{\partial\mathcal{B}_N} \hat{\mathbf{t}}^{(\mathbf{n})} \cdot \mathbf{u}\; dA \tag{7.5}$$

with the body force vector $\mathbf{b}$, the external traction vector $\hat{\mathbf{t}}^{(\mathbf{n})}$ prescribed on $\mathcal{B}_N$ and vector $\mathbf{n}$ defining the normal vector at the boundary $\partial\mathcal{B}$. Substituting for the *Green strain tensor* $\mathbf{E}$ its definition (Eq. 2.23) we further write

$$\Pi = \int_{\mathcal{B}} \left\{ \frac{1}{2}\mathbf{F}\mathbf{S} : \mathbf{F} - \frac{1}{2}\,\mathrm{tr}(\mathbf{S}) \right\} dV - \int_{\mathcal{B}} \rho_0\tilde{\psi}(\mathbf{S})\; dV + \mathcal{W}_{ext}(\mathbf{u}) = \text{stationary}\,. \tag{7.6}$$

Making use of *Gauss's divergence theorem* we consider the following modification of Eq. (7.6)

$$\Pi = -\int_{\mathcal{B}} \left\{ \frac{1}{2\sqrt{G}} \left(\sqrt{G}\, \mathbf{F}\mathbf{S}\mathbf{G}^i \right)_{,i} \cdot \mathbf{x} - \frac{1}{2} \operatorname{tr}(\mathbf{S}) \right\} dV + \int_{\partial\mathcal{B}} \frac{1}{2} \mathbf{F}\mathbf{S}\mathbf{n} \cdot \mathbf{x}\; dA - \\ - \int_{\mathcal{B}} \rho_0 \tilde{\psi}(\mathbf{S})\; dV + \mathcal{W}_{ext}(\mathbf{u}) = \text{stationary}\,, \tag{7.7}$$

For simplicity, we consider the basis vectors $\mathbf{G}_i$ to be independent of the coordinate charts θ^i in what follows. The above functional is assumed to hold for any arbitrary displacement field $\delta\mathbf{u}$ and stress $\delta\mathbf{S}$ which leads to the variation of Eq. (7.7) given by

$$\frac{\partial \Pi}{\partial \mathbf{u}} \cdot \delta\mathbf{u} = -\int_{\mathcal{B}} \left\{ \frac{1}{2} \left(\mathbf{F}_{,i}\mathbf{S}\mathbf{G}^i + \mathbf{F}\mathbf{S}_{,i}\mathbf{G}^i \right) \cdot \delta\mathbf{u} + \frac{1}{2} \left(\mathbf{x} \otimes \mathbf{G}^i \right) \mathbf{S}^T : \delta\mathbf{F}_{,i} + \right. \\ \left. + \frac{1}{2} \left(\mathbf{x} \otimes \mathbf{G}^i \right) \mathbf{S}^T_{,i} : \delta\mathbf{F} \right\} dV + \int_{\partial\mathcal{B}} \left\{ \frac{1}{2} (\mathbf{x} \otimes \mathbf{n})\, \mathbf{S}^T : \delta\mathbf{F} + \frac{1}{2} \mathbf{F}\mathbf{S}\mathbf{n} \cdot \delta\mathbf{u} \right\} dA + \\ + \mathcal{W}_{ext}(\delta\mathbf{u}) = 0$$

$$\frac{\partial \Pi}{\partial \mathbf{S}} \cdot \delta\mathbf{S} = -\int_{\mathcal{B}} \left\{ \frac{1}{2} \mathbf{F}^T_{,i} \left(\mathbf{x} \otimes \mathbf{G}^i \right) : \delta\mathbf{S} + \frac{1}{2} \mathbf{F}^T \left(\mathbf{x} \otimes \mathbf{G}^i \right) : \delta\mathbf{S}_{,i} + \frac{1}{2} \mathbf{1} : \delta\mathbf{S} \right\} dV + \\ + \int_{\partial\mathcal{B}} \frac{1}{2} \mathbf{F}^T (\mathbf{x} \otimes \mathbf{n}) : \delta\mathbf{S}\; dA - \int_{\mathcal{B}} \rho_0 \frac{\tilde{\psi}(\mathbf{S})}{\partial \mathbf{S}} : \delta\mathbf{S}\; dV = 0\,. \tag{7.8}$$

The implementation of the above formulation (Eq. 7.8) and first numerical tests indicate that the functional is numerically instable. It is believed that this behaviour is related to one particular term in Eq. (7.8) which is the following

$$-\int_{\mathcal{B}} \frac{1}{2} \mathbf{1} : \delta\mathbf{S}\; dV\,. \tag{7.9}$$

This leads to the consideration that the removal of this term, which has to be achieved by modifying Eq. (7.6) in suitable manner, might lead to a numerically stable variational formulation. In the following section this will be outlined in more detail.

7.2.2 Second version

Starting from Eq. (7.6) we replace the deformation gradient tensor by the following expression

$$\mathbf{F} = \mathbf{1} + \mathbf{H} \tag{7.10}$$

where $\mathbf{H} = \mathbf{u}_{,i} \otimes \mathbf{G}^i$ is the displacement gradient tensor and we achieve

$$\Pi = \int_{\mathcal{B}} \left\{ \mathbf{S} : \mathbf{H} + \frac{1}{2} \mathbf{H}\mathbf{S} : \mathbf{H} \right\} dV - \int_{\mathcal{B}} \rho_0 \tilde{\psi}(\mathbf{S})\; dV + \mathcal{W}_{ext}(\mathbf{u}) = \text{stationary}\,. \tag{7.11}$$

After some simplification *Gauss's divergence theorem* is applied and we further have

$$\Pi = -\int_{\mathcal{B}} \left\{ \frac{1}{\sqrt{G}} \left(\sqrt{G}\,\mathbf{S}\mathbf{G}^i \right)_{,i} \cdot \mathbf{u} + \frac{1}{2\sqrt{G}} \left(\sqrt{G}\,\mathbf{H}\mathbf{S}\mathbf{G}^i \right)_{,i} \cdot \mathbf{u} \right\} dV + \\ + \int_{\partial\mathcal{B}} \left\{ \mathbf{S}\mathbf{n} \cdot \mathbf{u} + \frac{1}{2}\mathbf{H}\mathbf{S}\mathbf{n} \cdot \mathbf{u} \right\} dA - \int_{\mathcal{B}} \rho_0 \tilde{\psi}\left(\mathbf{S}\right)\, dV + \mathcal{W}_{ext}\left(\mathbf{u}\right) = \text{stationary}\,. \tag{7.12}$$

The variation of Eq. (7.12) in $\mathbf{u}$ and $\mathbf{S}$ is given by

$$\frac{\partial \Pi}{\partial \mathbf{u}} \cdot \delta\mathbf{u} = -\int_{\mathcal{B}} \left\{ \mathbf{S}_{,i}\mathbf{G}^i \cdot \delta\mathbf{u} + \frac{1}{2}\mathbf{H}_{,i}\mathbf{S}\mathbf{G}^i \cdot \delta\mathbf{u} + \frac{1}{2}\mathbf{H}\mathbf{S}_{,i}\mathbf{G}^i \cdot \delta\mathbf{u} + \right. \\ \left. + \frac{1}{2}\left(\mathbf{u}\otimes\mathbf{G}^i\right)\mathbf{S}^T\mathbf{G}^j \cdot \delta\mathbf{u}_{,ji} + \frac{1}{2}\left(\mathbf{u}\otimes\mathbf{G}^i\right)\mathbf{S}^T_{,i}\mathbf{G}^j \cdot \delta\mathbf{u}_{,j} \right\} dV + \\ + \int_{\partial\mathcal{B}} \left\{ \mathbf{S}\mathbf{n} \cdot \delta\mathbf{u} + \frac{1}{2}\mathbf{H}\mathbf{S}\,\mathbf{n} \cdot \delta\mathbf{u} + \frac{1}{2}\left(\mathbf{u}\otimes\mathbf{n}\right)\mathbf{S}^T\mathbf{G}^j \cdot \delta\mathbf{u}_{,j} \right\} dA + \mathcal{W}_{ext}\left(\delta\mathbf{u}\right) = 0$$

$$\frac{\partial \Pi}{\partial \mathbf{S}} \cdot \delta\mathbf{S} = -\int_{\mathcal{B}} \left\{ \left(\mathbf{u}\otimes\mathbf{G}^i\right) : \delta\mathbf{S}_{,i} + \frac{1}{2}\mathbf{H}^T_{,i}\left(\mathbf{u}\otimes\mathbf{G}^i\right) : \delta\mathbf{S} + \frac{1}{2}\mathbf{H}^T\left(\mathbf{u}\otimes\mathbf{G}^i\right) : \delta\mathbf{S}_{,i} \right\} dV + \\ + \int_{\partial\mathcal{B}} \left\{ \left(\mathbf{u}\otimes\mathbf{n}\right) : \delta\mathbf{S} + \frac{1}{2}\mathbf{H}^T\left(\mathbf{u}\otimes\mathbf{n}\right) : \delta\mathbf{S} \right\} dA - \\ - \int_{\mathcal{B}} \rho_0 \frac{\tilde{\psi}\left(\mathbf{S}\right)}{\partial\mathbf{S}} : \delta\mathbf{S}\; dV = 0 \tag{7.13}$$

7.2.3 Numerical applicability

The implementation of the mixed functional (Eq. 7.13) outlined in the previous section gives rise to the difficulty that the coefficient matrix of the initial discrete equation system holds zero entries on parts of its diagonal which correspond to the displacement particle parameters. Therefore, it is necessary to incorporate at the beginning of the modelling an additional formulation which acts as a kind of perturbation and makes the discrete equation system solvable. This is achieved by altering Eq. (7.2) as follows

$$\hat{\mathcal{F}} = \alpha\,\mathcal{F} + (1-\alpha)\;\mathcal{F}\,. \tag{7.14}$$

With Eq. (7.1) the following relation for $\mathcal{F}$ (Eq. 7.2) holds

$$\mathcal{F} = \rho_0 \psi\left(\mathbf{E}\right)\,. \tag{7.15}$$

Therefore, it is admissible to substitute Eq. (7.2) and Eq. (7.15) into Eq. (7.14) as follows

$$\hat{\mathcal{F}} = \alpha\,\rho_0\psi\left(\mathbf{E}\right) + (1-\alpha)\,\left(\mathbf{S}:\mathbf{E} - \rho_0\tilde{\psi}\left(\mathbf{S}\right)\right)\,, \tag{7.16}$$

where α is so-called perturbation parameter which controls degree of the perturbation of the formulation. Replacing Eq. (7.2) in this functional with its modified counterpart (Eq. 7.7) and we arrive at

$$\begin{aligned}\Pi = \alpha \int_{\Omega} \rho_0 \psi\left(\mathbf{E}\right)\ dV - (1-\alpha) \int_{\mathcal{B}} \left\{ \left(\mathbf{S}\mathbf{G}^i\right)_{,i} \cdot \mathbf{u} + \frac{1}{2}\left(\mathbf{H}\mathbf{S}\mathbf{G}^i\right)_{,i} \cdot \mathbf{u} \right\} dV + \\ + (1-\alpha) \int_{\partial\mathcal{B}} \left\{ \mathbf{S}\mathbf{n} \cdot \mathbf{u} + \frac{1}{2}\mathbf{H}\mathbf{S}\mathbf{n} \cdot \mathbf{u} \right\} dA - \ (1-\alpha) \int_{\mathcal{B}} \rho_0 \tilde{\psi}\left(\mathbf{S}\right)\ dV + \\ + \mathcal{W}_{ext}\left(\mathbf{u}\right) = \text{stationary}\,. \end{aligned} \tag{7.17}$$

Finally, the variation of Eq. (7.17) in $\mathbf{u}$ and $\mathbf{S}$ is expressed as follows

$$\begin{aligned}\frac{\partial \Pi}{\partial \mathbf{u}} \cdot \delta\mathbf{u} = \alpha \int_{\Omega} \rho_0 \frac{\partial \psi\left(\mathbf{E}\right)}{\partial \mathbf{E}} : \delta\mathbf{E}\ dV - (1-\alpha) \int_{\mathcal{B}} \left\{ \mathbf{S}_{,i}\mathbf{G}^i \cdot \delta\mathbf{u} + \frac{1}{2}\mathbf{H}_{,i}\mathbf{S}\mathbf{G}^i \cdot \delta\mathbf{u} + \frac{1}{2}\mathbf{H}\mathbf{S}_{,i}\mathbf{G}^i \cdot \delta\mathbf{u} + \right. \\ \left. + \frac{1}{2}\left(\mathbf{u} \otimes \mathbf{G}^i\right)\mathbf{S}^T\mathbf{G}^j \cdot \delta\mathbf{u}_{,ji} + \frac{1}{2}\left(\mathbf{u} \otimes \mathbf{G}^i\right)\mathbf{S}^T_{,i}\mathbf{G}^j \cdot \delta\mathbf{u}_{,j} \right\} dV + \\ + (1-\alpha) \int_{\partial\mathcal{B}} \left\{ \mathbf{S}\mathbf{n} \cdot \delta\mathbf{u} + \frac{1}{2}\mathbf{H}\mathbf{S}\,\mathbf{n} \cdot \delta\mathbf{u} + \frac{1}{2}\left(\mathbf{u} \otimes \mathbf{n}\right)\mathbf{S}^T\mathbf{G}^j \cdot \delta\mathbf{u}_{,j} \right\} dA + \mathcal{W}_{ext}\left(\delta\mathbf{u}\right) = 0 \end{aligned}$$

$$\begin{aligned}\frac{\partial \Pi}{\partial \mathbf{S}} \cdot \delta\mathbf{S} = -\left(1-\alpha\right) \int_{\mathcal{B}} \left\{ \left(\mathbf{u} \otimes \mathbf{G}^i\right) : \delta\mathbf{S}_{,i} + \frac{1}{2}\mathbf{H}^T_{,i}\left(\mathbf{u} \otimes \mathbf{G}^i\right) : \delta\mathbf{S} + \right. \\ \left. + \frac{1}{2}\mathbf{H}^T\left(\mathbf{u} \otimes \mathbf{G}^i\right) : \delta\mathbf{S}_{,i} \right\} dV + (1-\alpha) \int_{\partial\mathcal{B}} \left\{ \left(\mathbf{u} \otimes \mathbf{n}\right) : \delta\mathbf{S} + \frac{1}{2}\mathbf{H}^T\left(\mathbf{u} \otimes \mathbf{n}\right) : \delta\mathbf{S} \right\} dA - \\ - (1-\alpha) \int_{\mathcal{B}} \rho_0 \frac{\tilde{\psi}\left(\mathbf{S}\right)}{\partial \mathbf{S}} : \delta\mathbf{S}\ dV = 0 \end{aligned} \tag{7.18}$$

As Eq. (7.17) is a combination of Eq. (7.15) and Eq. (7.7), accordingly, it is the solution for the stress field. Therefore, the *second Piola-Kirchhoff stress tensor* must be computed as follows

$$\mathbf{S}\left(\mathbf{E},\,\mathbf{S}\right) = \alpha\,\mathbf{S}\left(\mathbf{E}\right) + (1-\alpha)\ \mathbf{S} \tag{7.19}$$

where $\mathbf{S}\left(\mathbf{E}\right)$ is the material stress defined by

$$\mathbf{S}\left(\mathbf{E}\right) = \rho_0 \frac{\partial \psi\left(\mathbf{E}\right)}{\partial \mathbf{E}} \tag{7.20}$$

and $\mathbf{S}$ is the interpolated stress tensor. Note that in case of a non-linear calculation the perturbation of the original variational formulation (Eq. 7.13) is needed only for the first loading step. The initial value for the perturbation parameter α is chosen as small as possible, usually we have $\alpha \approx 1.0 \times 10^{-6}$. Within the first calculation step during the iteration process α is continuously decreased until it vanishes.

In order to test the numerical applicability of Eq. (7.18) the hyperelastic *Saint-Venant-Kirchhoff* model for the stored energy function is utilized:

$$\rho_0 \psi(\mathbf{E}) = \frac{1}{2} \mathbf{D}\mathbf{E} : \mathbf{E}, \tag{7.21}$$

where $\mathbf{D}$ defines the fourth-order elasticity tensor. Assuming for $\psi(\mathbf{E})$ convexity its inverse is given by

$$\rho_0 \tilde{\psi}(\mathbf{S}) = \frac{1}{2} \mathbf{D}^{-1}\mathbf{S} : \mathbf{S}. \tag{7.22}$$

The modelling of beams under tension provides accurate solutions for stress and displacement field. However, very poor results are obtained for bending problems. Two reasons for this behaviour might play a role. Firstly, it seems that the approximation of the stress derivatives is not sufficiently accurate which is crucial as the derivations of the *second Piola-Kirchhoff stress tensor* are a core part of this modified variational principle. This conjecture is further confirmed in Sec. 7.5 and Sec. 6.3.3. Secondly, the use of *Gauss's divergence theorem* requires the equivalence of volume and surface integrals which, apparently, can not be ensured numerically as the MLS-approximation of the solution function is substantially more accurate within the domain than at the boundary. For details on the latter the reader is referred to Sec. 3.2. Interestingly, the modelling becomes stable, if the boundary and the interior of domain $\mathcal{B}$ is linked together at least at one integration point. That is, the particle support zones of the MLS-approximation functions (Eq. 3.5) are chosen to be very large so that the MLS-approximation scheme at this particular integration point incorporates all particle parameters of the domain $\mathcal{B}$. In that way the mathematical equivalence of volume and surface integrals seems to be already integrated in the discrete equation system as kind of additional condition.

The application of higher order polynomial should theoretically improve the approximation accuracy of the MLS-approximants (Eq. 3.5), but in fact, it leads to oscillating solutions. The second order basis polynomial is found to be the highest applicable one. As the weight function used in Eq. (3.5) signs responsible for the global smoothness of the approximation, one could expect that the higher order continuity of the weight function might have a positive effect on the solution. However, the C^∞ Gaussian spline spline (Eq. 3.33) does not significantly improve the result compared with that obtained using the C^2 cubic spline (Eq. 3.30).

Another issue is the enforcement of the essential boundary conditions which are in case of the mixed functional (Eq. 7.18) the displacement as well as the traction boundary conditions. It basically means that at the entire boundary $\partial\mathcal{B}$ essential boundary conditions are applied which need to be enforced. For this model two different boundary enforcement methods are implemented. These are, firstly, the modified boundary collocation method (see Sec. 3.3.2.1) which is very costly due to its involved algorithm and secondly, the penalty method which becomes critical to use, if the ratio of the problem's surface to its volume is large. In this case a large part of the coefficient matrix of the discrete equation system is numerically penalized and the problem becomes unsolvable.

7.3 Mixed modified variational principle based on the *Hellinger-Reissner* functional with independent displacement, rotation and stress field

In the previous section it was outlined, how a mixed variational formulation based on the *Hellinger-Reissner* can be modified to incorporate second order derivatives of the displacement field as well as first order derivatives of the stress field. The general idea of this approach can also be used to develop a formulation which involves additional to the independent displacement and stress field an independent rotation field.

Let us assume hyperelastic material behaviour and $\rho_0\psi(\mathbf{U})$ define the stored energy per unit volume which is a functional of a stretch-type strain measure $\mathbf{U}$:

$$\mathbf{U} = \mathbf{R}^T\mathbf{F} \tag{7.23}$$

where $\mathbf{F}$ is the deformation gradient tensor (Eq. 2.5) and $\mathbf{R} \in SO(3)$ is the rotation tensor (Eq. 5.4) which is considered to be independent of the map $\boldsymbol{\varphi}(\mathbf{X}, t)$ (Eq. 2.1) and consequently of the displacement field. Furthermore, let $\tilde{\psi}(\boldsymbol{n})$ define the complementary function of $\psi(\mathbf{U})$, where $\boldsymbol{n}$ denotes a stress tensor defined by

$$\boldsymbol{n} = \rho_0 \frac{\partial \psi(\mathbf{U})}{\partial \mathbf{U}} \tag{7.24}$$

which is conjugate to the strain tensor $\mathbf{U}$. Then assuming for $\psi(\mathbf{U})$ convexity and making use of the *Legendre transformation* the following expression holds

$$\rho_0\psi(\mathbf{U}) + \rho_0\tilde{\psi}(\boldsymbol{n}) = \boldsymbol{n} : (\mathbf{U} - \mathbf{1}) \ . \tag{7.25}$$

Reformulating (Eq. 7.25) as follows

$$\mathcal{F} = \boldsymbol{n} : (\mathbf{U} - \mathbf{1}) - \rho_0\tilde{\psi}(\boldsymbol{n}) \ , \tag{7.26}$$

an expression is obtained which is a function of the strain tensor $\mathbf{U}$ and the stress tensor $\boldsymbol{n}$. Since the computation of $\mathbf{U}$ involves the deformation gradient $\mathbf{F}$, which is a function of the displacement field $\mathbf{u}$, but also the rotation tensor $\mathbf{R}$ which is a function of an independent rotation field $\boldsymbol{\gamma}$, Eq. (7.26) is therefore a three-field functional.

Now, the subsequent procedure is according to Sec. 7.2 that is we assume that the body under consideration $\mathcal{B}$ possesses an elastic potential Π which can be expressed with Eq. (7.26) as follows

$$\Pi = \int_{\mathcal{B}} \left\{ \boldsymbol{n} : (\mathbf{U} - \mathbf{1}) - \rho_0\tilde{\psi}(\boldsymbol{n}) \right\} \, dV + \mathcal{W}_{ext}(\mathbf{u}) = \text{stationary} \, , \tag{7.27}$$

where the external potential $\mathcal{W}_{ext}$ is given by Eq. (7.5). Note that Eq. (7.27) is the so-called *Hellinger-Reissner functional*. Redrafting Eq. (7.27) to

$$\Pi = \int_{\mathcal{B}} \left\{ \mathbf{R}\boldsymbol{n}\mathbf{G}^i \cdot \mathbf{x}_{,i} - tr\,(\boldsymbol{n}) - \rho_0 \tilde{\psi}(\boldsymbol{n}) \right\} dV + \mathcal{W}_{ext}\,(\mathbf{u}) = \text{stationary} \tag{7.28}$$

and applying *Gauss's divergence theorem* leads us to the final expression

$$\Pi = \int_{\mathcal{B}} \left\{ -\frac{1}{\sqrt{G}} \left(\sqrt{G}\,\mathbf{R}\boldsymbol{n}\mathbf{G}^i \right)_{,i} \cdot \mathbf{x} - \text{tr}\,(\boldsymbol{n}) - \rho_0 \tilde{\psi}(\boldsymbol{n}) \right\} dV + \tag{7.29}$$

$$+ \int_{\partial\mathcal{B}} \mathbf{R}\boldsymbol{n}\,\mathbf{n} \cdot \mathbf{x}\; dA + \mathcal{W}_{ext}\,(\mathbf{u}) = \text{stationary}\,, \tag{7.30}$$

where for simplicity the basis vectors $\mathbf{G}_i$ are assumed to be independent of the coordinate charts θ^i. In comparison with Eq. (7.12) this formulation also involves first order derivatives of the stress field, but no derivatives of the displacement field and additional to Eq. (7.12), first order derivatives of the rotation field. Note that corresponding to Eq. (7.30) we find as underlying field equations the following relations

$$\frac{1}{\sqrt{G}} \left(\sqrt{G}\,\mathbf{R}\boldsymbol{n}\mathbf{G}^i \right)_{,i} + \mathbf{b} = \mathbf{0}\,, \qquad \text{in } \mathcal{B}\,, \tag{7.31}$$

$$\boldsymbol{n}\mathbf{U}^T = \text{symmetric} \qquad \text{in } \mathcal{B}\,, \tag{7.32}$$

$$\mathbf{R}\boldsymbol{n}\,\mathbf{n} = \mathbf{t}^{(\mathbf{n})}\,, \quad \text{on } \partial\mathcal{B}_N\,. \tag{7.33}$$

This approach is surely an interesting one from the theoretical point of view, however, it is conjectured that its use for modelling would exhibit similar difficulties as the formulation Eq. (7.12) outlined in Sec. 7.2. Therefore, no further efforts with the approach presented in this section are undertaken.

7.4 Modified variational principle inspired by the *Hu-Washizu* functional

7.4.1 Variational formulation

In this section a variational principle is introduced which is inspired by the so-called *Hu-Washizu functional* (Washizu 1975). The *Hu-Washizu* functional originally incorporates three independent fields which are the displacement field $\mathbf{u}$, the *Green strain tensor* $\mathbf{E}$ and the *second Piola-Kirchhoff stress tensor* $\mathbf{S}$. It reads in the Lagrangian form as follows

$$\Pi_{HW} = \int_{\mathcal{B}} \left\{ \rho_0 \psi\left(\mathbf{E}\right) - \mathbf{S} : \mathbf{E} + \mathbf{S} : \frac{1}{2}\left(\mathbf{F}^T\mathbf{F} - \mathbf{1}\right) \right\} dV + \mathcal{W}_{ext}\left(\mathbf{u}\right) = \text{stationary} \tag{7.34}$$

where $\mathbf{F}$ is the deformation gradient tensor (Eq. 2.5) and the external potential $\mathcal{W}_{ext}$ is given by Eq. (7.5). The variation of Eq. (7.34) leads to the following relations

$$\int_{\mathcal{B}} \left(-\frac{1}{\sqrt{G}} \left(\sqrt{G}\, \mathbf{F}\mathbf{S}\mathbf{G}^i \right)_{,i} - \mathbf{b} \right) \cdot \delta\mathbf{u}\; dV = 0\,, \qquad \int_{\partial\mathcal{B}_N} \left(\mathbf{F}\mathbf{S}\mathbf{n} - \hat{\mathbf{t}}^{(\mathbf{n})} \right) \cdot \delta\mathbf{u}\; dA = 0\,, \tag{7.35}$$

$$\int_{\mathcal{B}} \left(\frac{1}{2}\left(\mathbf{F}^T\mathbf{F} - \mathbf{1}\right) - \mathbf{E} \right) : \delta\mathbf{S}\; dV = 0\,, \tag{7.36}$$

$$\int_{\mathcal{B}} \left(\rho_0 \frac{\partial \psi\left(\mathbf{E}\right)}{\partial \mathbf{E}} - \mathbf{S} \right) : \delta\mathbf{E}\; dV = 0\,, \tag{7.37}$$

where for simplicity the basis vectors $\mathbf{G}_i$ are considered to be independent of the coordinate charts θ^i. Considering that $\delta\mathbf{u}$, $\delta\mathbf{E}$ and $\delta\mathbf{S}$ are free variations, thus, the integrands must vanish so that we can identify Eq. (7.35) as the *equilibrium equations*, Eq. (7.36) as the kinematics, i.e. the definition of the *Green strain tensor* (Eq. 2.23), and Eq. (7.37) as the material law.

With $\mathbf{F} = \mathbf{1} + \mathbf{H}$ and $\mathbf{H}$ denoting the displacement gradient we write the *Hu-Washizu functional* (Eq. 7.34) as follows

$$\begin{aligned} \Pi = \int_{\mathcal{B}} \left\{ \rho_0 \psi\left(\mathbf{E}\right) - \mathbf{S} : \mathbf{E} + \frac{1}{2}\left(\mathbf{1} + \mathbf{H}\right)\mathbf{S} : \left(\mathbf{1} + \mathbf{H}\right) - \frac{1}{2}\mathbf{S} : \mathbf{1} \right\} dV + \\ + \mathcal{W}_{ext}\left(\mathbf{u}\right) = \text{stationary}\,. \end{aligned} \tag{7.38}$$

Further simplified we arrive at

$$\Pi = \int_{\mathcal{B}} \left\{ \rho_0 \psi\left(\mathbf{E}\right) - \mathbf{S} : \mathbf{E} + \left(\mathbf{1} + \frac{1}{2}\mathbf{H} \right) \mathbf{S} : \mathbf{H} \right\} dV + \mathcal{W}_{ext}\left(\mathbf{u}\right) = \text{stationary}\,. \tag{7.39}$$

After integration by parts and making use of *Gauss's divergence theorem* we obtain

$$\Pi = \int_{\mathcal{B}} \left\{ \rho_0 \psi\left(\mathbf{E}\right) - \mathbf{S} : \mathbf{E} - \frac{1}{\sqrt{G}} \left(\sqrt{G} \left(\mathbf{1} + \frac{1}{2}\mathbf{H} \right) \mathbf{S}\mathbf{G}^i \right)_{,i} \cdot \mathbf{u} \right\} dV + \\ + \int_{\partial\mathcal{B}} \left(\mathbf{1} + \frac{1}{2}\mathbf{H} \right) \mathbf{S}\mathbf{n} \cdot \mathbf{u} \; dA + \mathcal{W}_{ext}\left(\mathbf{u}\right) = \text{stationary}\,. \tag{7.40}$$

In order to reduce this formulation to a pure displacement based one we have to replace the independent field functions $\mathbf{E}$ and $\mathbf{S}$ by functions of the displacement field $\mathbf{u}$. These are Eq. (2.23) and

$$\mathbf{S}\left(\mathbf{u}\right) = \rho_0 \frac{\partial \psi\left(\mathbf{E}\left(\mathbf{u}\right)\right)}{\partial \mathbf{E}\left(\mathbf{u}\right)}\,, \tag{7.41}$$

respectively. Thus, we arrive at

$$\Pi = \int_{\mathcal{B}} \left\{ \rho_0 \psi\left(\mathbf{E}\left(\mathbf{u}\right)\right) - \mathbf{S}\left(\mathbf{u}\right) : \mathbf{E}\left(\mathbf{u}\right) \right\} dV - \int_{\mathcal{B}} \frac{1}{\sqrt{G}} \left(\sqrt{G} \left(\mathbf{1} + \frac{1}{2}\mathbf{H} \right) \mathbf{S}\left(\mathbf{u}\right) \mathbf{G}^i \right)_{,i} \cdot \mathbf{u} \; dV + \\ + \int_{\partial\mathcal{B}} \left(\mathbf{1} + \frac{1}{2}\mathbf{H} \right) \mathbf{S}\left(\mathbf{u}\right) \mathbf{n} \cdot \mathbf{u} \; dA + \mathcal{W}_{ext}\left(\mathbf{u}\right) = \text{stationary} \tag{7.42}$$

Of all admissible deformations the solution corresponds to that one which makes the functional stationary. For this reason we vary all terms with respect to the unknown displacement field $\mathbf{u}$. The variation of Π (Eq. (7.42) is given by the following functional

$$\delta\Pi = \int_{\mathcal{B}} \left\{ \rho_0 \frac{\partial \psi}{\partial \mathbf{E}} : \delta\mathbf{E} - \rho_0 \frac{\partial^2 \psi}{\partial \mathbf{E} \partial \mathbf{E}} \delta\mathbf{E} : \mathbf{E} - \rho_0 \frac{\partial \psi}{\partial \mathbf{E}} : \delta\mathbf{E} \right\} dV - \\ - \int_{\mathcal{B}} \left\{ \frac{1}{2} \delta\mathbf{H}_{,i} \, \rho_0 \frac{\partial \psi}{\partial \mathbf{E}} \mathbf{G}^i \cdot \mathbf{u} + \frac{1}{2} \mathbf{H}_{,i} \, \rho_0 \frac{\partial^2 \psi}{\partial \mathbf{E} \partial \mathbf{E}} \delta\mathbf{E}\mathbf{G}^i \cdot \mathbf{u} + \frac{1}{2} \mathbf{H}_{,i} \, \rho_0 \frac{\partial \psi}{\partial \mathbf{E}} \mathbf{G}^i \cdot \delta\mathbf{u} \right\} dV - \\ - \int_{\mathcal{B}} \left\{ \frac{1}{2} \delta\mathbf{H} \left(\rho_0 \frac{\partial \psi}{\partial \mathbf{E}} \right)_{,i} \mathbf{G}^i \cdot \mathbf{u} + \left(\mathbf{1} + \frac{1}{2}\mathbf{H} \right) \left(\rho_0 \frac{\partial^2 \psi}{\partial \mathbf{E} \partial \mathbf{E}} \delta\mathbf{E} \right)_{,i} \mathbf{G}^i \cdot \mathbf{u} + \right. \\ \left. + \left(\mathbf{1} + \frac{1}{2}\mathbf{H} \right) \left(\rho_0 \frac{\partial \psi}{\partial \mathbf{E}} \right)_{,i} \mathbf{G}^i \cdot \delta\mathbf{u} \right\} dV + \\ + \int_{\partial\mathcal{B}} \left\{ \frac{1}{2} \delta\mathbf{H} \, \rho_0 \frac{\partial \psi}{\partial \mathbf{E}} \mathbf{n} \cdot \mathbf{u} + \left(\mathbf{1} + \frac{1}{2}\mathbf{H} \right) \rho_0 \frac{\partial^2 \psi}{\partial \mathbf{E} \partial \mathbf{E}} \delta\mathbf{E}\mathbf{n} \cdot \mathbf{u} \right\} dA + \\ + \int_{\partial\mathcal{B}} \left(\mathbf{1} + \frac{1}{2}\mathbf{H} \right) \rho_0 \frac{\partial \psi}{\partial \mathbf{E}} \mathbf{n} \cdot \delta\mathbf{u} \; dA + \\ + \mathcal{W}_{ext}\left(\delta\mathbf{u}\right) = 0\,. \tag{7.43}$$

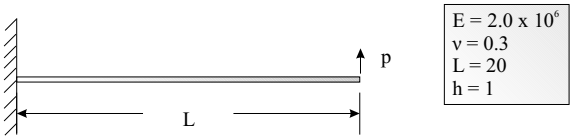

Figure 7.1: *problem configuration*

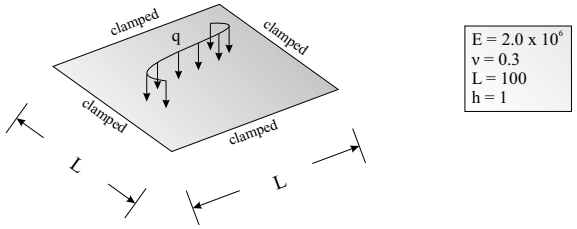

Figure 7.2: *problem configuration*

Further redrafting leads to the final variational expression given by

$$
\begin{aligned}
\delta\Pi = \int_{\mathcal{B}} \Big\{ & -\frac{1}{2}\,\rho_0 \frac{\partial^2\psi}{\partial\mathbf{E}\partial\mathbf{E}}\,\delta\mathbf{F}^T\mathbf{F} : \mathbf{E} - \frac{1}{2}\,\rho_0 \frac{\partial^2\psi}{\partial\mathbf{E}\partial\mathbf{E}}\,\mathbf{F}^T\delta\mathbf{F} : \mathbf{E} \Big\}\, dV + \\
& - \int_{\mathcal{B}} \Big\{ \frac{1}{2}\,\delta\mathbf{H}_{,i}\,\rho_0 \frac{\partial\psi}{\partial\mathbf{E}}\mathbf{G}^i\cdot\mathbf{u} + \frac{1}{4}\,\mathbf{H}_{,i}\,\rho_0 \frac{\partial^2\psi}{\partial\mathbf{E}\partial\mathbf{E}}\,\delta\mathbf{F}^T\mathbf{F}\mathbf{G}^i\cdot\mathbf{u} + \frac{1}{4}\,\mathbf{H}_{,i}\,\rho_0 \frac{\partial^2\psi}{\partial\mathbf{E}\partial\mathbf{E}}\,\mathbf{F}^T\delta\mathbf{F}\mathbf{G}^i\cdot\mathbf{u} + \Big\} \\
& \quad + \frac{1}{2}\,\mathbf{H}_{,i}\,\rho_0 \frac{\partial\psi}{\partial\mathbf{E}}\mathbf{G}^i\cdot\delta\mathbf{u} \Big\}\, dV - \\
& - \int_{\mathcal{B}} \Big\{ \frac{1}{2}\,\delta\mathbf{H}\left(\rho_0 \frac{\partial\psi}{\partial\mathbf{E}}\right)_{,i}\mathbf{G}^i\cdot\mathbf{u} + \frac{1}{2}\left(\mathbf{1}+\frac{1}{2}\,\mathbf{H}\right)\left(\rho_0 \frac{\partial^2\psi}{\partial\mathbf{E}\partial\mathbf{E}}\right)_{,i}\delta\mathbf{F}^T\mathbf{F}\mathbf{G}^i\cdot\mathbf{u} + \\
& \quad + \frac{1}{2}\left(\mathbf{1}+\frac{1}{2}\,\mathbf{H}\right)\left(\rho_0 \frac{\partial^2\psi}{\partial\mathbf{E}\partial\mathbf{E}}\right)_{,\mathrm{i}}\mathbf{F}^T\delta\mathbf{F}\mathbf{G}^i\cdot\mathbf{u} + \frac{1}{2}\left(\mathbf{1}+\frac{1}{2}\,\mathbf{H}\right)\rho_0 \frac{\partial^2\psi}{\partial\mathbf{E}\partial\mathbf{E}}\,\delta\mathbf{F}_{,i}^T\mathbf{F}\mathbf{G}^i\cdot\mathbf{u} + \\
& \quad + \frac{1}{2}\left(\mathbf{1}+\frac{1}{2}\,\mathbf{H}\right)\rho_0 \frac{\partial^2\psi}{\partial\mathbf{E}\partial\mathbf{E}}\,\mathbf{F}_{,i}^T\delta\mathbf{F}\mathbf{G}^i\cdot\mathbf{u} + +\frac{1}{2}\left(\mathbf{1}+\frac{1}{2}\,\mathbf{H}\right)\rho_0 \frac{\partial^2\psi}{\partial\mathbf{E}\partial\mathbf{E}}\,\delta\mathbf{F}^T\mathbf{F}_{,i}\mathbf{G}^i\cdot\mathbf{u} + \\
& \quad + \frac{1}{2}\left(\mathbf{1}+\frac{1}{2}\,\mathbf{H}\right)\rho_0 \frac{\partial^2\psi}{\partial\mathbf{E}\partial\mathbf{E}}\,\mathbf{F}^T\delta\mathbf{F}_{,i}\mathbf{G}^i\cdot\mathbf{u} + \left(\mathbf{1}+\frac{1}{2}\,\mathbf{H}\right)\left(\rho_0 \frac{\partial\psi}{\partial\mathbf{E}}\right)_{,i}\mathbf{G}^i\cdot\delta\mathbf{u} \Big\}\, dV + \\
& + \int_{\partial\mathcal{B}} \Big\{ \frac{1}{2}\,\delta\mathbf{H}\,\rho_0 \frac{\partial\psi}{\partial\mathbf{E}}\mathbf{n}\cdot\mathbf{u} + \frac{1}{2}\left(\mathbf{1}+\frac{1}{2}\,\mathbf{H}\right)\rho_0 \frac{\partial^2\psi}{\partial\mathbf{E}\partial\mathbf{E}}\,\delta\mathbf{F}^T\mathbf{F}\mathbf{n}\cdot\mathbf{u} + \\
& \quad + \frac{1}{2}\left(\mathbf{1}+\frac{1}{2}\,\mathbf{H}\right)\rho_0 \frac{\partial^2\psi}{\partial\mathbf{E}\partial\mathbf{E}}\,\mathbf{F}^T\delta\mathbf{F}\mathbf{n}\cdot\mathbf{u} + \left(\mathbf{1}+\frac{1}{2}\,\mathbf{H}\right)\rho_0 \frac{\partial\psi}{\partial\mathbf{E}}\,\mathbf{n}\cdot\delta\mathbf{u} \Big\}\, dA + \\
& + \mathcal{W}_{ext}\,(\delta\mathbf{u}) = 0\,.
\end{aligned}
\tag{7.44}
$$

7.4.2 Numerical experiments

The modified variational principle (Eq. 7.44) developed in the previous section is obviously very involved. Its practicability for numerical computations is now investigated with two different problems. For both examples the *Saint-Venant-Kirchhoff* constitutive model for the stored energy function $\rho_0\psi$ is chosen which involves as material parameters *Young's modulus* E and *Poisson ratio* ν.

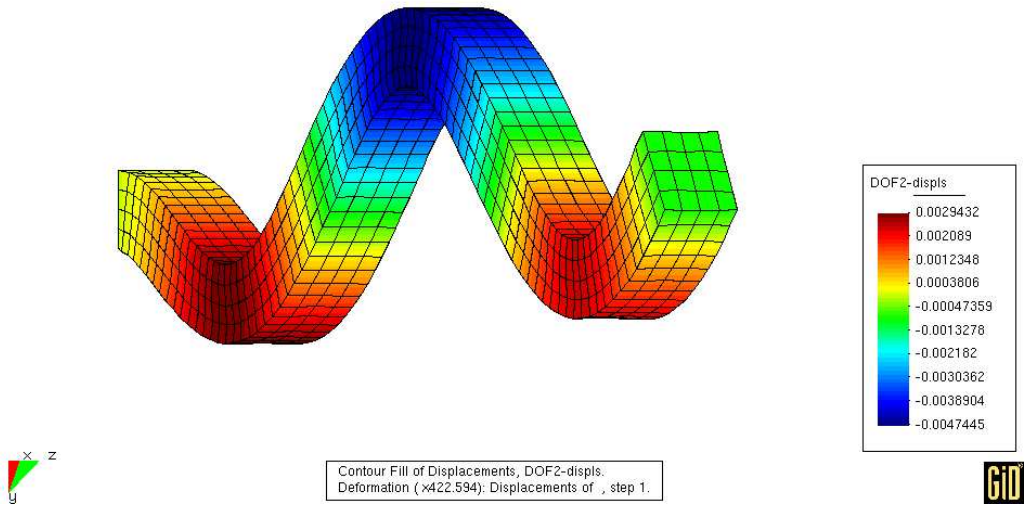

Figure 7.3: *deformed configuration*

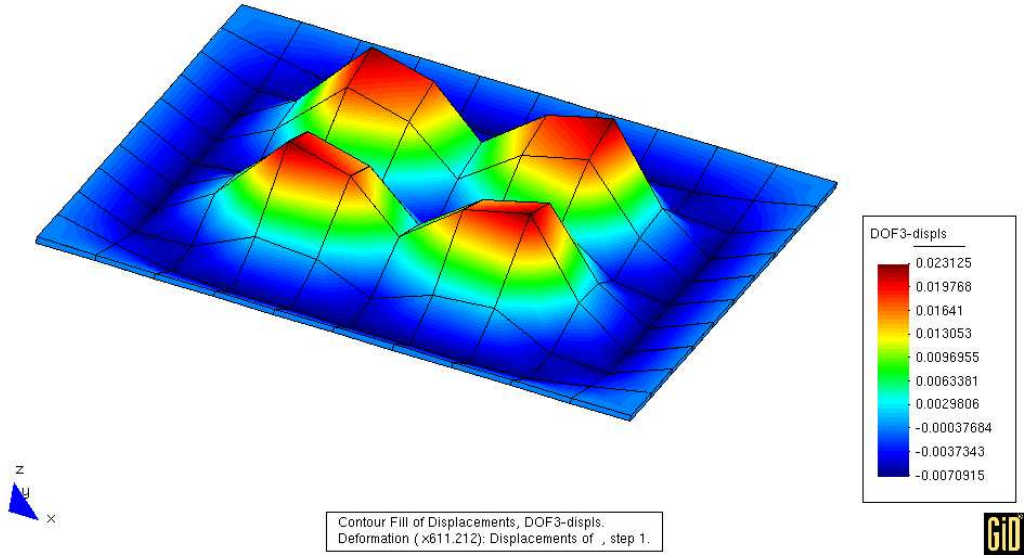

Figure 7.4: *deformed configuration*

The first example is a cantilever beam subjected to a body force $b = 1.0$ acting in y-direction depicted in Fig. 7.1. The solution of the deformed configuration illustrated in Fig. 7.2 is oscillating and called a spurious mode.

The second example a square plate depicted in Fig. 7.2 subjected to a dead loading $q = 1.0$ and clamped at all four edges. The solution of the square plate turns out to be a rather spurious mode as well.

It is discovered that the oscillations disappear for both examples, if at least one Dirichlet boundary particle lies within the influence radius of all other particles. This however results in huge particle influence zones and is therefore not practical.

Interestingly, the simulation of a beam under tension which is not shown here, provides good results for linear as well as for non-linear modelling. This observation might be explained by the fact that the analytical solution is a linear function of the beams's longitudinal coordinate. Hence, the consistency requirements on the meshfree approximation functions are lower and the approximation accuracy of the second order derivatives of the solution function is apparently sufficient.

7.5 Integral form of the equilibrium equations

The mixed formulation (Eq. 7.13) as well as displacement based formulation (Eq. 7.44) presented in the previous sections failed to be numerical stable. It is believed that the elaborate mathematical modifications of the *Hellinger Reissner functional* and the *Hu-Washizu functional*, respectively, which result in various to each other corresponding volume and surface integral expressions, are not suitable to be modelled.

Therefore, the objective to incorporate second order derivatives of the solution function into a modified variational principle is pursuit by another very straightforward approach which is the integral form of the equilibrium equations (Eq. 4.4) which can be directly implemented in MLS-based meshfree methods as the MLS shape functions are capable to provide the necessary continuity. For this, the equilibrium equations are at first multiplied by a weight function $\delta\mathbf{u}$ and integrate over the domain $\mathcal{B}$ and its boundary $\partial\mathcal{B}_N$, respectively, and we have:

$$-\int_{\mathcal{B}} \frac{1}{\sqrt{G}} \left(\sqrt{G}\,\mathbf{F}\mathbf{S}\mathbf{G}^i\right)_{,i} \cdot \delta\mathbf{u}\; dV + \int_{\partial\mathcal{B}_N} \mathbf{F}\mathbf{S}\mathbf{n} \cdot \delta\mathbf{u}\; dA + \mathcal{W}_{ext} = 0\,, \tag{7.45}$$

where the external potential $\mathcal{W}_{ext}$ is given by Eq. (7.5) and the basis vectors $\mathbf{G}_i$ are assumed to be independent of the coordinate charts θ^i. Note however, that this formulation is not symmetrical.

In contrast to the variational formulations (Eq. 7.13) and (Eq. 7.44) the approach in the previous section (Eq. (7.45) does not make use of *Gauss's divergence theorem*. Accordingly, the boundary integral expression in Eq. (7.45) is not directly related to the volume integral expression as result of mathematical manipulations, but is explicitly incorporated as natural boundary condition. Therefore, the boundary term does not enter the formulation, if no external traction loading is applied.

This formulation is therefore ideal to study the applicability of second order derivatives in comparison to the variational principles presented in Sec. 7.2 and Sec. 7.4. For this, we consider the cantilever beam introduced in Sec. 7.4.2 and depicted in Fig. 7.1, but we replace the traction loading by a body force. The approximation functions (Eq. 3.5) are computed using second order polynomial and a cubic spline (Eq. 3.30) to provide the necessary continuity. Geometrically linear modelling provides a good solution already for low particle discretization levels. However, non-linear computation fails, even if a very fine particle distributions is utilized. Exactly the same behaviour is observed for traction loading, where the natural boundary conditions are part of the formulation. The use of weight functions with higher continuity such as the Gaussian spline (Eq. 3.33) does not improve the results and higher order polynomials have a rather negative effect. The latter is conceivable as it is well-known that function approximation based on higher order polynomials exhibit a tendency to oscillate.

Considering that the variational formulation (Eq. 7.45) is very straightforward and nothing else than the integral form of the *equilibrium equations*, the suspect is further confirmed that the MLS approximation accuracy is not adequate for derivatives higher than first order.

7.6 Summary

In Sec. 7.2 - 7.5 various modified variational principles have been studied which involve higher order derivatives of the solution function. The numerical stability of all these formulations was not satisfying, this was especially the case for non-linear computations. It is well-known that in particular non-linear modelling has higher requirements on the approximation accuracy. The meshfree approximation functions are computed by a weighted least square fit (Eq. 3.2) which is minimized with respect to sample points of the solution function, but not for its derivatives. It is therefore clear that the approximation accuracy for the solution function derivatives is less than for the solution function itself. This fact is also shown in Sec. 3.2. Furthermore, the modifications which involved *Gauss's divergence theorem* and led to the mixed formulations (Eq. 7.13) and (Eq. 7.30) as well as to the variational principle based on the *Hu-Washizu* functional (Eq. 7.44) put additional constraints on the approximation accuracy. That is, the equivalence of the volume and the corresponding surface integral expressions.

Since the variational formulation (Eq. 7.45) which represents the integral form of the weighted equilibrium equations also fails to perform satisfactorily, and taken into account that it is not modified by the use of *Gauss's divergence theorem*, it is obvious that the lacking approximation accuracy for the second order derivatives of the solution function is a main issue. Now, it is not clear, whether or not the use of *Gauss's divergence theorem* has part on the numerical instabilities. This is due to the fact that it leads to the incorporation of additional boundary integral terms and it was shown in Sec. 3.2 that the boundary approximation accuracy is substantially worse than for the interior domain. Testing the mixed formulation with an independent rotation field (Eq. 7.30) could perhaps provide more clarity, because it does not involve higher than first order function derivatives, but it is modified utilizing *Gauss's divergence theorem*.

Considering that all formulations outlined in the previous sub-sections are not stable using the Gauss quadrature, the original aim to study the applicability of a particle integration scheme is not pursuit any further.

Chapter 8

Conclusion

The presented generalized deformation formulation in Sec. 6.1 is an elegant way to describe physical behaviour originated from the microstructural level. Three different approaches for a generalized deformation description illustrate its adaptivity to certain properties of the material's underlying micro-structure. Moreover, these models allow the incorporation of any conventional constitutive law in a very straightforward manner. This fact is demonstrated using two different hyperelastic materials, firstly, the linear *Saint-Venant-Kirchhoff* model and secondly, a non-linear statistically based one.

The simulated results of size-scale effects of elastic bending experiments on epoxy polymer micro-beams show a very good agreement with the experimental data. Obviously, the epoxy material is well characterized by the generalized micromorph deformation description (Eq. 6.31). The discrepancy between classical and non-classical continuum theory is clearly demonstrated in case of torsion of human bone specimens. This difference in the predicted solution is shown to be more distinct than exhibited for the *Cosserat continuum*-based formulation (Eq. 5.26). This is especially true for non-linear modelling.

The study on the excavation openings in rock specifically reveals that the incorporation of elastic strain gradients can significantly change the distribution of stresses and displacement around excavation constructions. Moreover, it is shown that the generalized micromorph deformation formulation can be defined in such a way that orthotropic material behaviour is described. In particular, the use of meshfree methods enables to directly approximate the higher gradient parts of the formulation which is so not possible using FEM. Furthermore, meshfree approximations of generalized continuum-based approaches as applied in this thesis prove to be independent of the particle distribution density. Moreover, it is demonstrated that this feature is lost, when the formulation is based on the classical *Green strain tensor* which exhibits clear dependency on the particle distribution.

The generalized *Cosserat* continuum formulation (Eq. 6.96) provides the possibility to model micropolar material behaviour by linking the spatial change of the rotation tensor with the basis vectors of the micro-space. This allows to control the influence of the corresponding parts of the curvature tensor (Eq. 6.82) by the specific definition of the micro-continuum's dimension and the corresponding internal length scale parameters. The computation of

micro-films demonstrates that the macroscopic response is significantly influenced by the incorporation of deformation related to the material's microstructure. In particular, the deformation process exhibits oriented behaviour which is directly connected to the choice of the microspace. The magnitude of this property is manipulated by the value of the internal length scale parameters which is shown to allow to model size-scale effects.

The investigation of the *moving least square method*-based approximation functions gives valuable details which facilitate its application in the engineering area in general. It is shown that the minimum applicable influence radius depends on the utilized basis polynomial as the invertibility requirement of the moment matrix (Eq. 3.4) necessitates a specific minimum particle support for each point in the domain. However, in order to achieve smooth shape functions, a certain minimal overlapping of the particle influence zones is required. Otherwise, the involved weight function ordinates are numerically too small. Furthermore, the lack of particle support at the boundary has the effect that the influence radius of particles at the boundaries of the domain and adjacent to it must be chosen larger than that actually required for the interior domain. It is also demonstrated that for the lower polynomial orders the MLS shape functions possess under certain conditions the *Kronecker Delta property* which, however, is applicable in practise and can therefore not be exploited. The approximation accuracy is shown to increase according to the order of the used basis polynomial and the continuity of the weight function. However, the use of higher order polynomials is limited as the needed particle support rapidly rises so that the gain on accuracy is not justifiable in relation to the high demand on computing time. Furthermore, it is found that the optimal influence radius which provides the best accuracy is not necessarily the minimum applicable one. Moreover, the influence radius which minimizes the error of the approximation is different for the function and its derivatives, respectively. This is clear as the approximation accuracy of the function is only dependent on the locality of the approximation, so that the minimal applicable influence radius provides the least error. The approximation of the function derivatives additionally requires smoothness of the approximation of the function in the first place. This however, is not given for the minimal applicable influence radius, but only for this radius which ensures sufficient overlapping of the particle influence zones. This fact has to be considered when modelling problems which also involve the derivatives of the solution function. Another important finding is that the approximation accuracy at the boundary is considerably less than within the interior domain.

The modified variational principle (Eq. 4.11) presented in Sec. 4 primarily serves as a reference model representing the classical continuum approach. Nevertheless, a novel method is proposed which accounts for the imposition of the Dirichlet boundary conditions. That is to incorporate the essential boundary conditions in the functional and to enforce these conditions as a Euler-Lagrange equation. Numerical instabilities are addressed by including an additional penalty term, where the magnitude of the stabilization parameters $\beta(\theta^1, \theta^2, \hat{u}_i)$ are kept at relatively low levels, but sufficiently high to enforce the essential boundary conditions at all integration points within a given error tolerance. This is achieved by making use of an iterative algorithm to determine suitable values for $\beta(\theta^1, \theta^2, \hat{u}_i)$ individually for each integration point. Furthermore, Sec. 4.3.1 provides insight in the boundary approximation accuracy of MLS, as it is crucial for this modified variational principle. The lacking approximation accuracy at the boundary, which is compensated by the stabilization term,

already gives some indications to the difficulties which arise in Sec. 7 as those models also rely on an adequate boundary approximation accuracy.

In Sec. 5 a variational principle based on the conventional *Cosserat continuum* is introduced. A multiplicative updating scheme of the rotation field is investigated for its application in a MLS-based meshfree method. The result is somewhat in-conclusive, because the updating algorithm can be used in principle. However, if the rotation reaches 2π, the updated rotation tends to become ambiguous. The usage of the rotation updating method is therefore limited to a rotation smaller than 2π.

Finally, the applications of size-scale effects in elasticity show good results for the torsion of the human bone specimens. The predictions for the epoxy micro-beams however, only partially match the experimental data. It is therefore concluded that the physical properties of the epoxy polymer material is not satisfactorily described by this micropolar continuum.

The study of variational principles presented in Sec. 7.2 - 7.5, which are derived from classical variational formulations and involve higher order derivatives, prove to be numerically unstable. This fact indicates that the approximation accuracy of meshfree methods based on *moving least squares* is lacking. Therefore, the modelling with formulations incorporating higher order derivatives is rather problematic and needs further investigation. It can however, not definitely be determined, whether the insufficient approximation accuracy alone or also the mathematical manipulations involving *Gauss's divergence theorem* sign mainly responsible for the difficulties.

Chapter 9

Future work

The variational formulation (Eq. 6.58) based on the generalized micromorph deformation description introduced in Sec. 6.3.2 does not incorporate the generalized strain tensor (Eq. 6.41) as a whole. In particular, a constitutive law could be developed which separately addresses the pure micro-strain (Eq. 6.40) and an additional material parameter could be associated with this strain tensor.

The part of the generalized deformation approach (Eq. 6.14) which describes the micro-deformation is only linearly related to the micro-coordinate. A further extension would be a non-linear dependency on the coordinates of the micro-continuum.

The application on rock excavations presented in Sec. 6.3.3 and the micro-films examples illustrated in Sec. 6.4.3 demonstrate that it is possible to simulate orthotropic material behaviour. This potential is however not fully exploited yet, because the directional macroscopic material response is strictly linked to the basis vectors of the macro-continuum. It would be therefore of interest to induce a variable dependency on those basis vectors in a sense that the directors of the micro-continuum (Eq. 6.15) are rotated around the micro-space's origin by a set of angles which can be freely chosen. Then it would be also possible to address anisotropy originated in the material's microstructure.

Furthermore, it is believed that the real potential of this non-classical approach becomes visible in modelling non-linear plastic material behaviour. In general, it would be also interesting to study other material behaviour which is related to underlying microstructure such as localization phenomena.

As the modified variational principles proposed in Sec. 4.2 and Sec. 5.6 are shown to enhance the enforcement of essential boundary conditions, it would be worthwhile to consider similar modifications of the proposed generalized variational principles.

Considering the improvement in smoothness of the stress shown in Sec. 6.3.3 it might be possible to increase the accuracy of the first order stress derivatives by the incorporation of higher order strain gradients in such a way that the modified variational formulations presented in Sec. 7 could be dealt with. Furthermore, the suspended efforts on the particle integration could be taken up again.